Doctoral Dissertation

Studies on the Electronic Structure of Passive Films Formed on Ti and Cr

(Ti および Cr に生成する不働態皮膜の電子構造に関する研究)

Seong-Cheol Kim

金　成哲

December 2023

Division of Materials and Manufacturing Science,

Graduate School of Engineering,

Osaka University

Contents

Chapter 1
General introduction

Corrosion causes huge economic losses in many countries every year [1]. The global cost of corrosion is estimated to be 2.5 trillion US dollars, which is equivalent to 3.4 % of the global GDP in 2013 [2]. Therefore, the corrosion control of metallic materials provides cost benefits. To develop corrosion control, an understanding of the corrosion-induced degradation of materials is required. Passive films are well-known as oxide-based ultra-thin films formed at the surface of metallic materials to prevent direct contact with corrosive environments. The structure of passive films is thus crucial to suppress general corrosion and has been extensively studied. In addition, since the 1980s, the semiconductive nature and electronic structure of passive films have been considered to be related to their protective ability. In this chapter, the author first describes the passivity of metals and alloys, and the surface analytical techniques that have often been utilized to examine the structure of passive films. Then, the author explains the basis of semiconductor electrochemistry, which can be helpful to understand the semiconductive nature of passive films, followed by a summary of the research history of the semiconductive nature of passive films.

1.1 Passivation and passive film

1.1.1 Passivation

Passivation is a phenomenon that leads to the formation of an ultra-thin oxide-based film on metal and alloy surfaces in aqueous environments. This is the origin of the high corrosion resistance of metals and alloys such as Ti-based and Cr-containing alloys. One of the most frequently observed examples of passivity is the active–passive transition in the potentiodynamic polarization curve. Figure 1.1 shows a typical polarization curve exhibiting

an active–passive transition period. As shown in the figure, the current density increases with increasing applied potential from the corrosion potential. Subsequently, when the potential increases above E_{pp} (the primary passive potential), the current density drastically decreases by 10^{-4} – 10^{-6} times compared to the maximum value in the active state, i_{crit} (the critical anodic current density). This rapid current drop is attributed to the formation of a passive film that prevents the direct contact between the underlying substrate and the corrosive environment. The potential range where the low current density is maintained is called the passive state. The passive film deteriorates at higher potentials owing to the transpassive dissolution, which again increases the anodic current density.

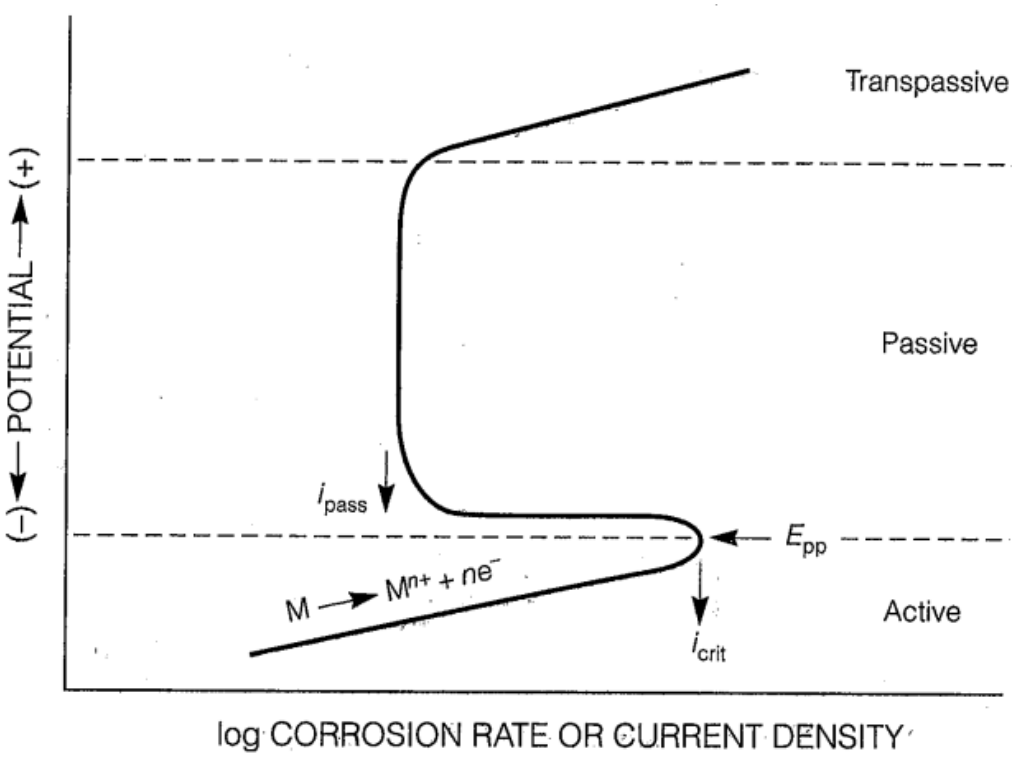

Figure 1.1 Schematic polarization behavior of a metal [3].

Fe–Cr, Ni–Cr, and Ti-based alloys are well-known to exhibit superior corrosion resistance in various corrosive environments. Therefore, the structure of passive films on these alloys has been extensively studied by X-ray photoelectron spectroscopy (XPS). Details regarding this surface analytical technique are described in Section 1.2. Common conclusions drawn from XPS studies of passive films on the alloys are as follows: (i) the passive films mainly consist of an inner oxide layer and a covering hydroxide layer, (ii) alloying elements are unevenly distributed in the passive films, and (iii) such distribution varies depending on the environment. When the semiconductive nature of passive films is examined and considered by the undermentioned photoelectrochemical response and electrochemical impedance spectroscopy, the analysis and interpretation of the results become complex. Therefore, in the present thesis, the author has focused on passive films formed on Ti and Cr to exclude the latter two of the three aforementioned factors, and on the electronic structure of passive films. In the following sections, general information regarding passive films on Ti and Cr is described.

1.1.2 Passive films formed on Ti and its alloys

The potential–pH diagram, also known as the Pourbaix diagram, demonstrates the thermodynamic stability of metals in aqueous environments. Figure 1.2 shows the Pourbaix diagram of the Ti–H_2O system [4]. The diagram indicates that it is thermodynamically favorable for Ti to dissolve at low potentials of approximately −1.7 V. However, Ti forms stable TiO_2 on the surface over a wide range of pHs, resulting in high corrosion resistance. In the case of Ti alloys such as Ti–6Al–4V and Ti–Ni alloys, passive films consisting mainly of TiO_2 also form on the surface [5-8]. It has been reported that passive films formed on Ti consist not only of stoichiometric TiO_2, but also of other titanium compounds. Pouilleau *et al.* explained that passive films on Ti were composed of the inner TiO and the outer TiO_2 [9]. Additionally, when Ti is exposed to an aqueous environment, hydroxide of Ti could be

formed by the reaction of the inner oxide layer with other OH^- or water [10]. Furthermore, the passive film on Ti and its alloys may have a porous structure in the outer layer. This porous structure is solely related to its biocompatibility [11], and the relatively high density of the inner layer has been reported to directly contribute to the corrosion resistance [12, 13]. Consequently, the passive films on Ti are composed of various oxides and hydroxides, and it is important to analyze their structures and characteristics.

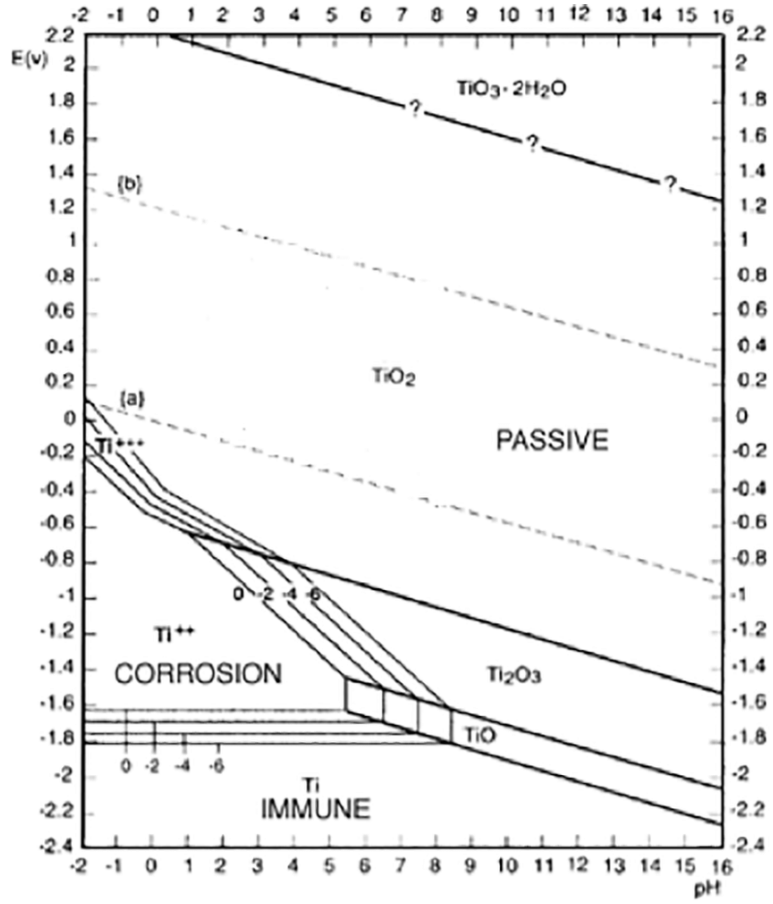

Figure 1.2 Pourbaix diagram of titanium (V_{SHE} vs. pH) [4].

1.1.3 Passive films formed on Cr and its alloys

Cr is also a representative metal that is spontaneously passivated to form a thin oxide or hydroxide layer on its surface. Passive films formed on Cr are very dense and prevent corrosive agents from penetrating to the metal surface, providing excellent corrosion resistance.

Figure 1.3 presents the Pourbaix diagram of Cr and the various types of oxides and hydroxides of Cr that are thermodynamically formed [14]. Cr belongs to the sixth group of transition metals and generally exhibits different oxidation states of +2, +3, and +6, as oxides or hydroxides. The most stable oxidation state of Cr is reported to be +3. Therefore, Cr_2O_3 and/or $Cr(OH)_3$ are essentially formed on the surface of Cr. Seo *et al.* has reported that the composition of the passive film on Cr was the same as Cr_2O_3 through depth profiling analysis, and that the upper part of the film was in the hydrated state [15]. Li *et al.* has also reported that the passive film of Cr, formed in aqueous sulfuric acid solution, was composed of Cr_2O_3 and $Cr(OH)_3$ [16]. These oxide and hydroxide forms of Cr are proposed to play an important role in the passivity of Cr. However, Cr is brittle and is therefore often used as an alloying element to provide corrosion resistance to high-strength alloys such as Fe- and Ni-based alloys. These Cr-containing alloys also form a passive film mainly composed of Cr. Marcus *et al.* described that the passive films of Fe–Cr alloys, i.e., stainless steels, possess a duplex structure with a mixed Cr^{3+} and Fe^{3+} oxide inner layer and a hydroxide outer layer of Cr [17]. Furthermore, they reported that passive films of Ni–Cr–Fe alloys formed in 0.05 M H_2SO_4 consisted of an inner oxide layer composed of Cr_2O_3 (96 %) and Fe_2O_3 (4 %) along with an outer hydroxide layer of $Cr(OH)_3$ [18].

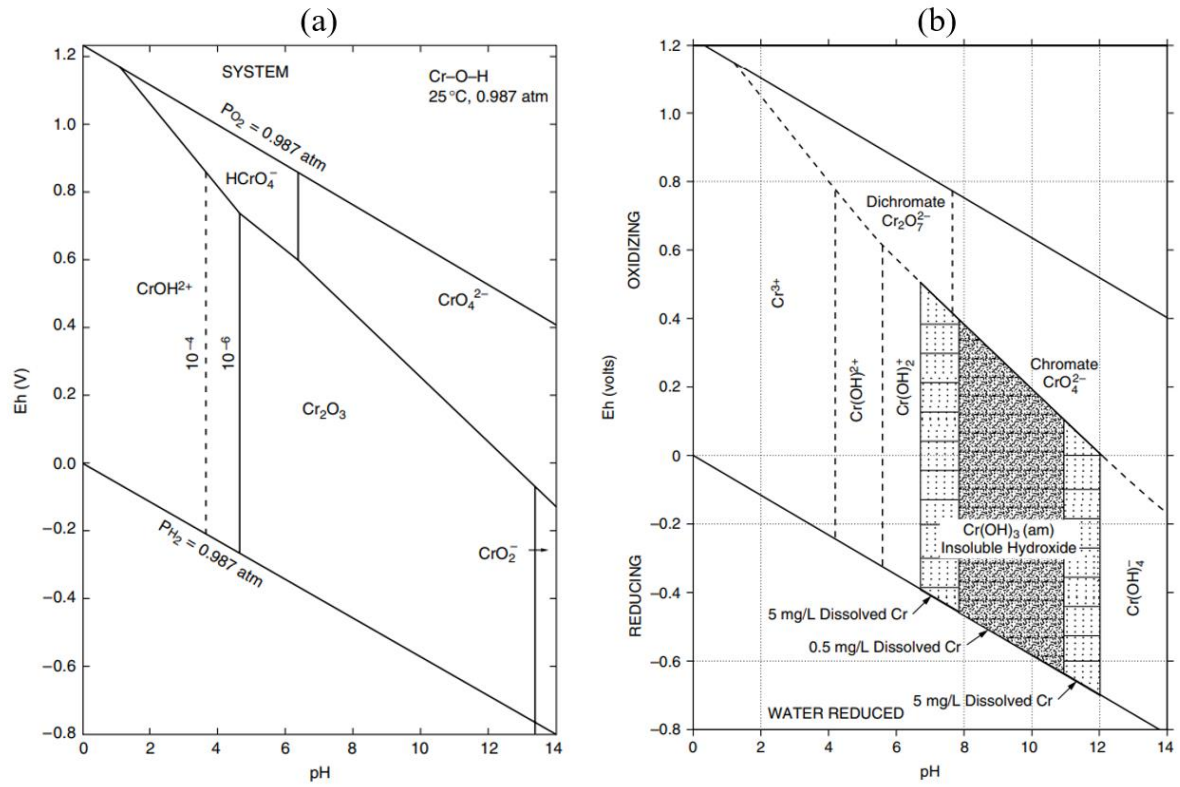

Figure 1.3 Pourbaix diagram for the (a) Cr–O–H system and (b) Cr–O–H_2O system. E_h values are in volts (V_{SHE}) [14].

1.2 Structural analysis of passive film

1.2.1 X-ray photoelectron spectroscopy

Among surface analytical techniques, X-ray photoelectron spectroscopy (XPS) is the most widely used for analyzing the chemical structure (thickness, chemical composition etc.) of passive films. This spectroscopic technique is based on the photoelectric effect first discovered by Hertz in 1887 [19], and its details were explained later by Einstein in 1905 [20]. In 1907, Innes successfully recorded an XPS spectrum for the first time using a spectrometer consisting of a magnetic field hemisphere (the kinetic energy analyzer of photoelectrons) and a photographic detector [21]. Owing to several significant improvements in the equipment, and a comprehensive study using the XPS equipment by Siegbahn, the utility of XPS has been recognized as a powerful surface analytical technique since the 1960s [22].

Because XPS is a highly sensitive surface analytical technique, it has been utilized in the passivity study to evaluate the chemical composition, thickness, and structure of passive films. XPS was first applied to the analysis of passive films on metals and alloys in the 1970s [23-29]. Since then, many researchers have applied XPS to analyze passive films on Ti-based and Cr-containing alloys, which exhibit excellent corrosion resistance. Pan *et al.* examined the effect of hydrogen peroxide on the passivity of Ti in a phosphate-buffered saline solution and confirmed the presence of peaks for Ti and O on passivated Ti in the XPS spectrum. The asymmetry of the Ti 2p spectrum was attributed to the presence of an outer hydroxide layer such as TiOOH [30]. Milošev analyzed the passive film of the Ti–Al–V alloy formed by electrochemical oxidation in a physiological solution using XPS [31] and revealed that TiO and Ti_2O_3 were formed at the film / alloy substrate interface, although the passive film mainly consisted of TiO_2.

In addition to the XPS studies related to passive films on Ti and Ti-based alloys, some XPS studies on the passivity of Cr and Cr-containing alloys are briefly described below. Stypula *et al.* reported that the XPS spectrum measured on a passive film of Cr formed in

sulfuric acid solution could be decomposed into peaks derived from Cr^{3+} oxide and hydroxide [32]. Asami *et al.* used XPS to quantitatively analyze the composition and structure of the passive films formed on Fe–Cr alloys in 1 M H_2SO_4. The structure of the passive films differed depending on the Cr content of the alloys, and it was reported that at a Cr content of 13 %, the main component of the passive films changed to hydrated chromium oxyhydroxide [26]. Lim *et al.* investigated the passive film formed on an Ni–Cr alloy in a 0.1 M NaCl solution. They reported that the passive film formed on the Ni–Cr alloy contained only Cr oxide owing to selective oxidation of Cr [33].

1.2.2 Auger electron spectroscopy

Auger electron spectroscopy (AES) has also been used for the analysis of passive films. In this analytical technique, the surface of a solid material is irradiated by an electron beam ejecting Auger electrons, and their kinetic energy is measured. Because the kinetic energy of Auger electrons is an intrinsic value depending on the element, the chemical composition of the material surface can be analyzed from the kinetic energy and intensity of Auger peaks; thus, the elements contained in the passive films can be quantified. Yaniv *et al.* used AES to investigate the effects of pH, Cl^- addition, and potential on the composition of passive films formed on ferritic stainless steel [34]. Bouyssoux *et al.* examined the passive films of Cr anodically polarized in sulfuric acid solutions and reported that the films consisted of 1.3 – 1.6 nm thick oxide layer with a composition close to Cr_2O_3 [28]. Solar *et al.* confirmed the changes in passive films on a Ti–6Al–4V alloy by polarization in a physiological chloride solution and compared the films with those obtained before polarization [35]. Boudin *et al.* investigated the passive films formed on an Ni–Cr alloy in borate buffer solutions and reported that the passive films were less than 2.5 nm in thickness and were composed of an inner layer of mainly Cr oxides and a few outer Ni oxyhydroxide layers [36].

These XPS and AES studies demonstrated that the chemical composition and structure

of passive films vary depending on the composition of metallic materials and the aqueous environments. As the chemical composition and structure of passive films can affect their electronic structures and resulting electronic properties, in particular the semiconductive properties which are relevant for the present thesis, the basis of semiconductor properties and the characteristics of the semiconductor / electrolyte interface are reviewed in the next section.

1.3 Semiconductor electrochemistry

As mentioned in the previous sections, the surfaces of most engineering metals and alloys are covered with an ultra-thin oxide-based film that possesses a protective ability against corrosion. Because many of the oxide-based films behave as semiconductors, the properties of the semiconductor / electrolyte interface are of considerable importance for the corrosion of metals and alloys.

1.3.1 Basic concepts of semiconductor

Semiconductors can be characterized by the energy levels of the valence band (VB) and the conduction band (CB), where the former is entirely occupied by electrons and the latter is vacant, and the Fermi level, E_F. A band gap separates the two energy bands, that is, the band gap energy, E_g, which is defined as the energy difference between the highest energy of the VB and the lowest energy of the CB. The Fermi level of a semiconductor is located within the band gap, as illustrated in Fig. 1.4. For intrinsic semiconductors, the concentration of electrons in the CB is equal to that of holes in the VB, and therefore the Fermi level is located at the center of the band gap. By contrast, semiconductors containing impurities are classified into the following two types: n-type and p-type. In such extrinsic semiconductors, the concentration of electrons and holes differ. In n-type semiconductors, the concentration of

electrons is significantly larger than that of holes, and the localized donor level is close to the CB. This alters the Fermi level to be closer to the CB. In the case of p-type semiconductors, the opposite situation is generated. Thus, the concentration of holes is significantly larger than that of electrons and therefore, the Fermi level is located closer to the VB as illustrated in Fig. 1.4 (c). These situations are realized by doping with an electron acceptor such as B or electron donor such as P, in silicon semiconductors. A similar situation is observed in oxide semiconductors as well. An excess or deficiency of oxygen ions provides a p-type or n-type semiconductive nature, respectively, in oxides. For example, CuO [37] and NiO [38] behave like p-type semiconductors whereas TiO_2 [39] and ZnO [40] behave like n-type semiconductors.

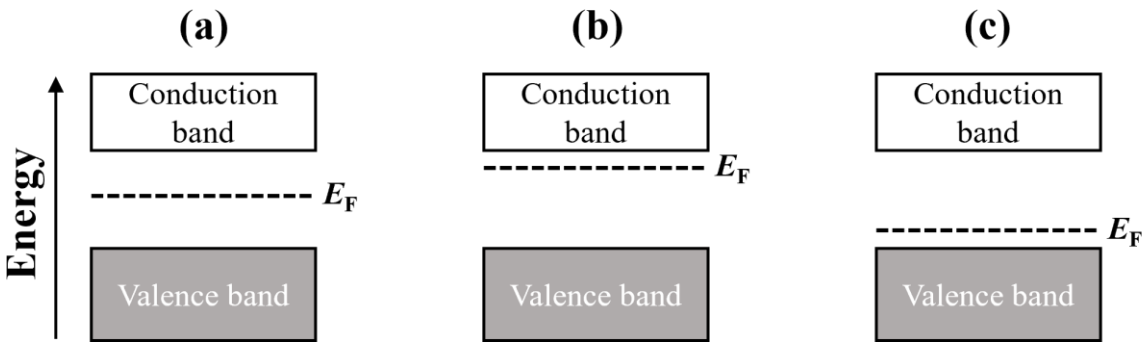

Figure 1.4 Schematic illustration of (a) an intrinsic semiconductor, (b) an n-type semiconductor, and (c) a p-type semiconductor [41].

1.3.2 Interface between semiconductor and electrolyte

Similar to the Fermi level in semiconductors, the Fermi level of redox electrons for the redox species in an electrolyte can also be defined. The electron state densities of reduced and oxidized species in a redox system are expressed as the product of the probability densities of the reduced and oxidized species, and the concentrations of the species, respectively. The

total state density is defined as the sum of the electron state densities of reduced and oxidized species as illustrated in Fig. 1.5 (a). In the figure, the level E^{o}_{redox}, where the electron density of the reduced species equals that of the oxidized species, is called the Fermi level of the redox electron. At this level, the total state density of the redox species is half occupied by electrons which provide the occupied state density of the reduced species, and the remaining half is vacant for the unoccupied state density of the oxidized species. When the semiconductor, with an E_F which is distinct from E^{o}_{redox} comes into contact with the electrolyte, a charge transfer takes place and continues until both Fermi levels are balanced, as illustrated in Figs. 1.5 (b) and (c) for n-type and p-type semiconductors, respectively. The charge transfer induces a space charge layer, where the concentration of the majority carriers is different from that in the bulk. When the concentration of the majority carriers in the space charge layer is lower than that in the bulk, the space charge layer is called a depletion layer. In the depleted state for n-type semiconductors, the space charge layer exhibits an upward band bending to the electrolyte as illustrated in Fig. 1.6 (b). By contrast, when the concentration near the surface is higher than that in the bulk for n-type semiconductors, the space charge layer is called an accumulation layer. In this case, the space charge layer exhibits a downward band bending. The space charge layer affects the separation of photo-excited charge carriers which are generated by the absorption of energy that is larger than the band gap energy. In the depletion layer for n-type semiconductors, photo-excited electrons in the CB travel to the substrate, whereas holes in the VB move to the interface with the electrolyte and are consumed by reduced species in the electrolyte. On the contrary, charge carriers in the accumulation layer move in the opposite direction to the depletion layer, that is, electrons are consumed by oxidized species in the electrolyte at the interface. This indicates that the direction of the photo-induced current strongly depends on the potential gradient within the space charge layer. Once the space charge layer is formed at the interface with the electrolyte, it can be varied with an applied potential. For instance, when the applied

potential is shifted in the less noble direction from the potential at which the depletion layer is formed, as shown in the center column of Fig. 1.6, and finally reaches the one shown in the left column, the space charge layer near the interface disappears and instead, the bottom of the CB and the top of the VB become flat, which is known as the flat-band state. In this state, no photo-induced current change is obtained. When the applied potential is shifted more in the less noble direction, the space charge layer becomes the accumulation layer, as shown in the right column of Fig. 1.6.

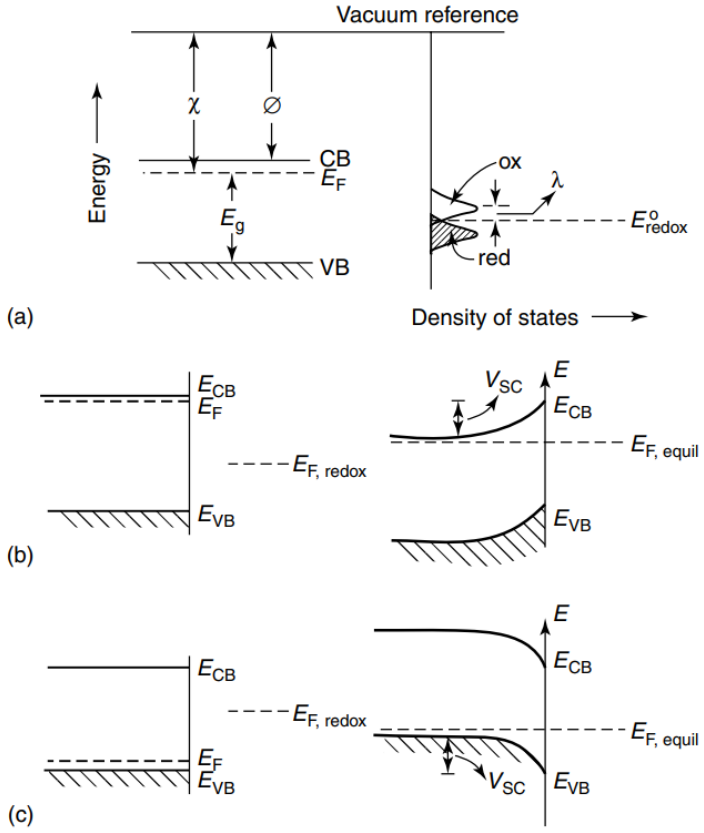

Figure 1.5 (a) Energy levels in a semiconductor (left-hand side) and a redox electrolyte (right-hand side) shown on a common vacuum reference scale. χ and φ are the semiconductor electron affinity and work function, respectively. (b) The semiconductor-electrolyte interface before (left) and after (right) equilibration (i.e., contact of the two phases) shown for an n-type semiconductor. (c) is the same as (b) but for a p-type semiconductor [41].

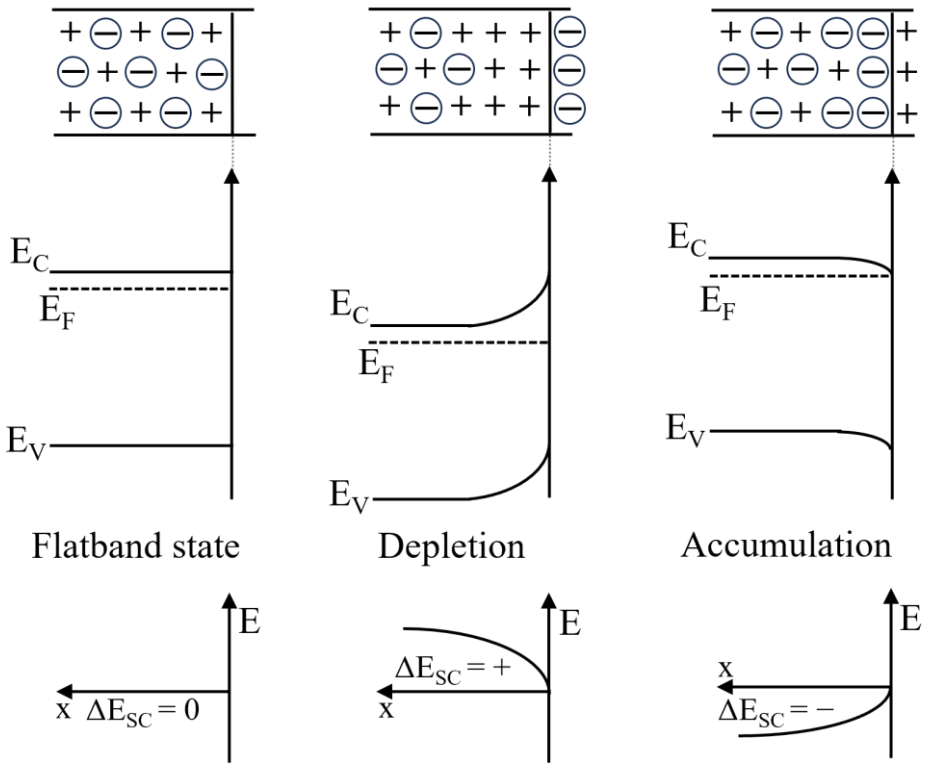

Figure 1.6 Space charge layers in an n-type semiconductor in contact with electrolytes. Above: distribution of charge carriers; middle: course of band edges; below: course of electric potential (*E*) [42].

1.4 Analytical techniques to evaluate the electronic structures of semiconductor materials and their properties

As mentioned above, most of the oxides (including hydroxides) behave as semiconductors although the specific semiconductor characteristics, such as the type of conduction, VB and CB edges, and band gap energy, differ depending on the oxides and hydroxides. This indicates that passive films can be also considered as semiconductors because they consist of oxides and hydroxides. The present section describes the analytical techniques often used to evaluate the electronic structures of semiconductor materials and their properties.

1.4.1 Valence band spectrum of XPS

XPS is based on photoionization; the surface of the specimen is excited by monochromatic X-ray photons and the emitted photoelectrons are separated according to their energy and then analyzed. The photon energy is large enough to extract electrons even from the inner atoms, thus ionizing the atoms. The penetration depth of photons is reported to be between 1 and 10 μm; however, photoelectrons can leave the surface only from several to tens of nm owing to their large inelastic scattering cross-section. Therefore, as previously described, XPS is a powerful analytical technique to investigate the chemical structure and characteristics of surfaces. Electrons in the valence level do not take a specific value, unlike the energy levels of an isolated inner shell which are well defined but exist in a wide energy range called the valence band. When valence electrons are excited by X-rays, the kinetic energy of the emitted photoelectrons increase as the energy of the X-ray is large and the distribution of the density of states can be considered as free electrons with a gentle distribution. It represents the density of state of valence electrons. In the case of metals, the bands overlap significantly, and there is no energy gap up to the highest energy level filled

with electrons (the Fermi level). Therefore, when measuring the valence band of the metal, the electron density rapidly increases at the Fermi level. As the Fermi level of transition metals is, in general, sharply observed, the energy is used for calibration. As the density of states is very sensitive to the bonding between atoms, and the passivation of metals affects the density of states of the valence band, the passivation of metal surfaces (the bonding between metal and oxygen) is evaluated from the valence band spectrum of XPS.

1.4.2 Electrochemical impedance spectroscopy

The history of electrochemical impedance spectroscopy (EIS) began with the basic knowledge established by Heaviside between 1880 and 1900 [43]. Warburg extended the concept of impedance to electrochemical systems and suggested that the interface could be expressed as a connection series of a polarization resistance and a capacitor [44]. Since the application of impedance to electrochemical systems, various electrochemical analyses have been performed on oxide films. Consequently, it was suggested that oxide films can be treated as dielectric. In the 1970s, Stimming *et al.* suggested that the space charge layer inside the passive film formed on an iron electrode is dielectric and discussed the dynamics of metal surface reactions on the metal and the electronic structure of the film [45].

The space charge layer formed in the semiconductor electrode in contact with the electrolyte changes its thickness and capacitance with an applied potential. The capacitances obtained from EIS measurements are often analyzed based on the theoretical Mott–Schottky equation which expresses the relationship between the capacitance of the space charge layer (the depletion layer) and the applied potential, that is, for depleted n-type semiconductors, the equation is described as Eq. (1.1) whereas for depleted p-type semiconductors, the equation is defined as Eq. (1.2).

$$\frac{1}{C_{SC}^2} = \frac{2}{\varepsilon\varepsilon_0 q N_D}\left(E_m - E_{fb} - \frac{kT}{q}\right), \quad (1.1)$$

$$\frac{1}{C_{SC}^2} = \frac{-2}{\varepsilon\varepsilon_0 q N_A}\left(E_m - E_{fb} + \frac{kT}{q}\right), \quad (1.2)$$

where C_{SC} represents the space charge capacitance in the semiconductor, ε and ε_0 represent the relative permittivity of the passive film and the vacuum permittivity (8.85×10^{-14} F/cm), respectively. q is the electric charge (1.602×10^{-19} C), and E_m and E_{fb} are the measuring potential and the flatband potential, respectively. In addition, N_D and N_A represent the donor and acceptor densities, respectively. The kT/q term is very small and therefore can be neglected. From the equations, it is found that the type of semiconductor and the concentration of carrier can be discussed from the slope of the Mott–Schottky plot. Figure 1.7 shows the Mott–Schottky plots of n-type and p-type semiconductors measured in an $AlCl_3$/n-butylpyridinium chloride molten-salt electrolyte [46].

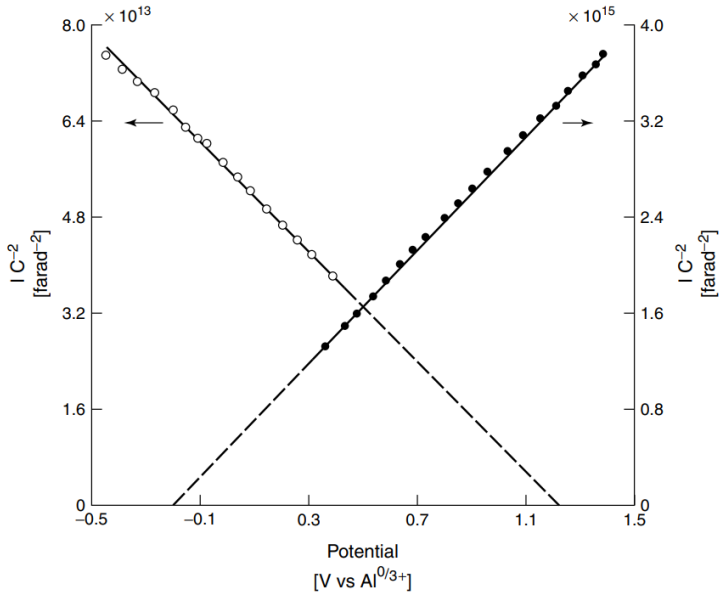

Figure 1.7 Mott–Schottky plots for n-type and p-type GaAs electrodes in an $AlCl_3$/n-butylpyridinium chloride molten-salt electrolyte [46].

1.4.3 Photoelectrochemical response

The effect of light on electrochemistry was discovered by Becquerel in 1839 [47]. In the field of corrosion science, Kruger reported the effect of light irradiation on Cu in a neutral solution [48]. In the 1950s and 1960s, photoelectrochemical responses were applied to compound semiconductors and oxide semiconductors in aqueous solutions [49-54]. Cronemeyer examined the photo transition effect of single crystal rutile at various temperatures and confirmed that the optical band energy of the crystal was about 3.05 eV [49]. Applications of the photo effects to characterize the electronic structure of passive films formed on metals and alloys have also been reported since the 1950s. Oshe *et al.* measured the photo potential of a passive film formed on Fe and reported that the film could function as a semiconductor [55]. Since the 1970s, the photoelectrochemical response has been extensively used to evaluate the semiconductive properties of various passive films [56-62]. In the 1990s, Gerischer led the relevant field of photoelectrochemistry through various pioneering works on oxide semiconductors as well as oxide films on metals [42, 63-65].

Photocurrent is generated by the transport of photo-excited charge carriers. Reactions that are induced by photo-excited carriers are illustrated in Fig. 1.8. In the case of p-type semiconductors, electrons are transported to the electrolyte and consumed by oxidants in the electrolyte while holes are transported towards the substrate, causing a negative photocurrent. In the case of n-type semiconductors, as shown in Fig. 1.8 (b), electrons travel to the substrate whereas holes move to the electrolyte and react with reductants in the electrolyte, causing a positive photocurrent. The photocurrents increase with a decreasing electrode potential for a p-type semiconductor and an increasing electrode potential for an n-type semiconductor, as shown in Fig. 1.9, because the width of the space charge layer increases according to the potential variations. Therefore, it can be concluded that the direction of the photocurrent and its potential dependence, can be used to characterize the type of semiconductor.

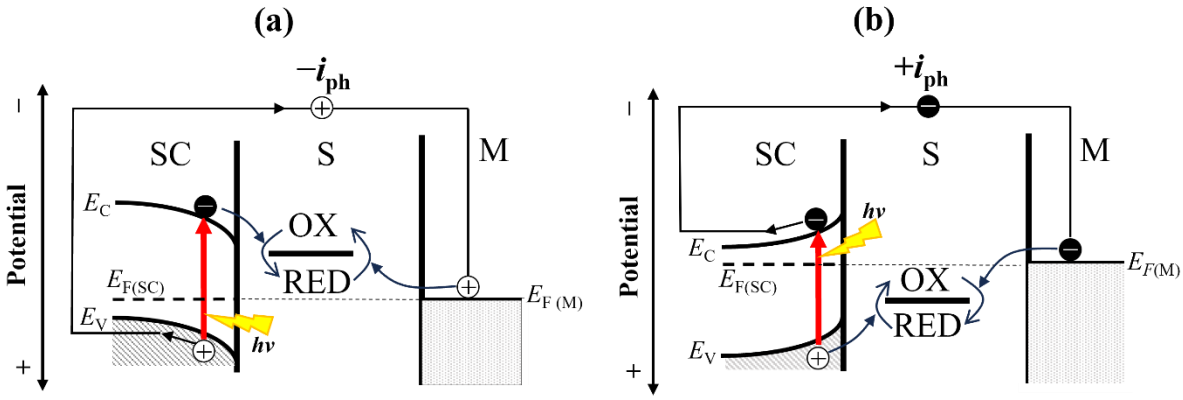

Figure 1.8 Photo-excited reaction current (photocurrent) at semiconductor electrodes: (a) photo-excited reaction of a cathodic electron transfer (OX + e → RED) at a p-type semiconductor electrode, (b) photo-excited reaction of an anodic hole transfer (RED → OX + e) at an n-type semiconductor electrode, i_{ph} : photocurrent [66].

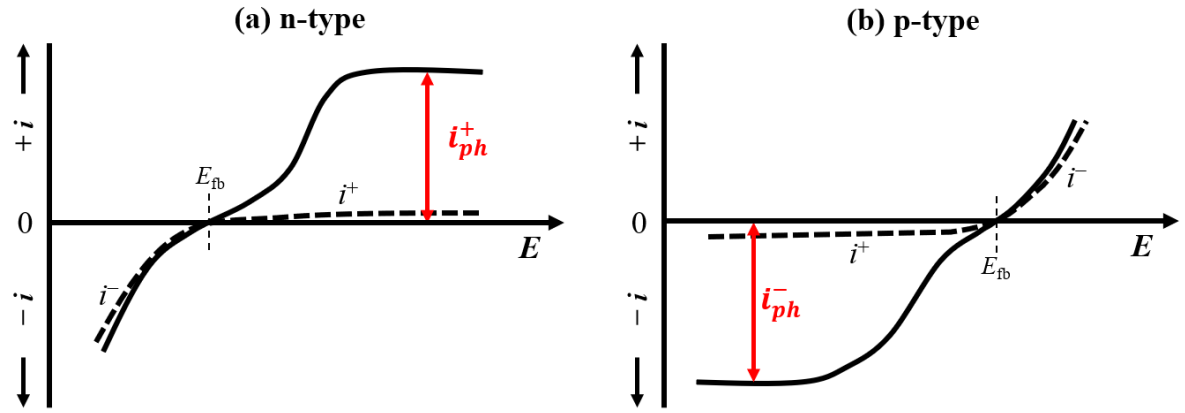

Figure 1.9 Polarization curves for electrode reactions at (a) n-type and (b) p-type semiconductor electrodes in the dark and in a photo-excited state: dashed curve = dark; solid curve = photo-excited; i^+ (i^-) = anodic (cathodic) current in the dark; i^+_{ph} (i^-_{ph}) = anodic (cathodic) current in a photo-excited state [66].

With regards to the photocurrents generated on compound semiconductors and passive films on metals and alloys, one of the most well-recognized characteristics is the photocurrent transient, which indicates the variations of photocurrent with time as illustrated in Fig. 1.10 [67]. The photocurrent transient was reported by Hardee in the 1970s for various metal oxides in polycrystals [57]. Later, in the 1980s, the photocurrent transient of passive films on Fe was examined by Peter, and the influence of surface recombination and band edge unpinning were discussed [68]. Azumi also explained the photocurrent transient by assuming an equivalent circuit for the passive film with an n-type semiconductive nature [69]. Numerous studies have been conducted to clarify the correlation between photocurrent transients and the electronic structure of passive films.

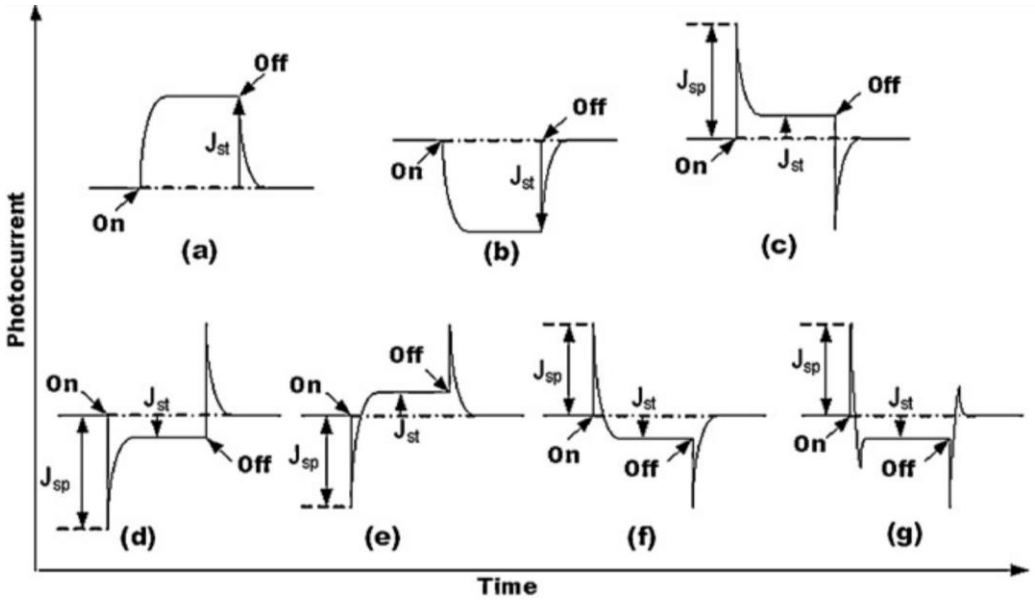

Figure 1.10 Various patterns of photocurrent transients for oxidation films formed on metal surfaces [67].

1.5 Semiconductor characteristics of passive films

Passive films formed on most metals such as Ti, Cr, Fe, and Ni, exhibit semiconductive behavior, because passive films are composed of oxides and hydroxides, both of which behave as semiconductors. The band gap energy of passive films on metals and alloys can be compared with the band gap energies for the oxides and hydroxides of the constituent elements which are included in the metallic materials. For instance, the band gap energies of NiO and $Ni(OH)_2$ are reported as 3.6 and 3.05 eV, respectively [70-72], whereas a passive film formed on Ni is reported to be a p-type semiconductor with a band gap energy of 2.9 – 3.1 eV [73, 74], implying that the passive film is mainly composed of $Ni(OH)_2$. In the case of Cr, although the band gap energies of Cr_2O_3 and $Cr(OH)_3$ are estimated as 3.5 – 3.6 eV and 2.5 – 2.7 eV, respectively, the band gap energy of passive films on Cr varies depending on where the films were formed [75-78], strongly indicating that the chemical composition of passive films on Cr varies. Furthermore, passive films on Cr were often reported to exhibit a typical p-type semiconductive behavior, but depending on the experimental environment, an n-type behavior is also found. By contrast, passive films formed on Ti, have often been reported to be an n-type semiconductor, with the band gap energy of 3.0 – 3.2 eV, which is in the range of anatase (E_g: 3.2 eV) [79-81], independent of the experimental environment.

Passive films are reported to have a multi-layered structure composed of oxides and hydroxides, which is supported by the results obtained from the photoelectrochemical response, as well as the electrochemical impedance spectroscopy. For instance, in the photoelectrochemical response, Tsuchiya *et al.* measured current changes induced by light-irradiation, so-called photocurrent, and found that positive and negative photocurrents appeared in a photocurrent spectrum. If the photocurrent was generated from a single semiconductive layer, the direction of the photocurrent should not have changed. Therefore, they concluded that the photocurrent spectrum, consisting of positive and negative photocurrents, reflected a multi-layered structure in the passive film [78]. Furthermore, they

proposed a duplex electronic band structure model for the passive film, which is an extension of the model proposed by Sato [82].

The electronic band structure model proposed by Tsuchiya *et al.* for passive films formed on Fe-Cr alloys in an acidic solution is presented in Fig. 1.11 (a). The corresponding model for a neutral solution is presented in Fig. 1.11 (b) [83]. In the models, the passive film in the acidic solution consists of inner p-type oxide and outer n-type hydroxide layers, whereas in the neutral solution, the model consists of inner n-type oxide and outer n-type hydroxide layers. The protectiveness and growth of passive films can be explained based on these models. It is well-known that passive films thicken more in neutral solutions but the protectiveness of the films is weaker, such that corrosion is more likely to occur in neutral solutions compared to acidic solutions. By contrast, passive films formed in acidic solutions are very thin, but highly protective against corrosion. In the proposed electronic band structure model for passive films formed in neutral solutions, metallic cations generated from the underlying metallic substrate and oxygen anions from the solution can travel outwards and inwards, respectively, along the potential gradient which is built within the passive films, resulting in its continuous growth. However, harmful anions such as chloride ions also penetrate the passive films, causing deterioration. By contrast, in the model for the passive films in acidic solutions, the outward movement of metallic cations and the inward movement of the anions are effectively suppressed. Therefore, the passive films in acidic solutions are very thin compared to the ones in neutral solutions, but highly protective due to the suppressed inward movement of harmful anions. Furthermore, one of the semiconductive properties of passive films, i.e., carrier density, is also reported to be related to the localized corrosion resistance [84, 85]. From this, one can conclude that understanding the electronic structure and semiconductive properties of passive films is of great importance.

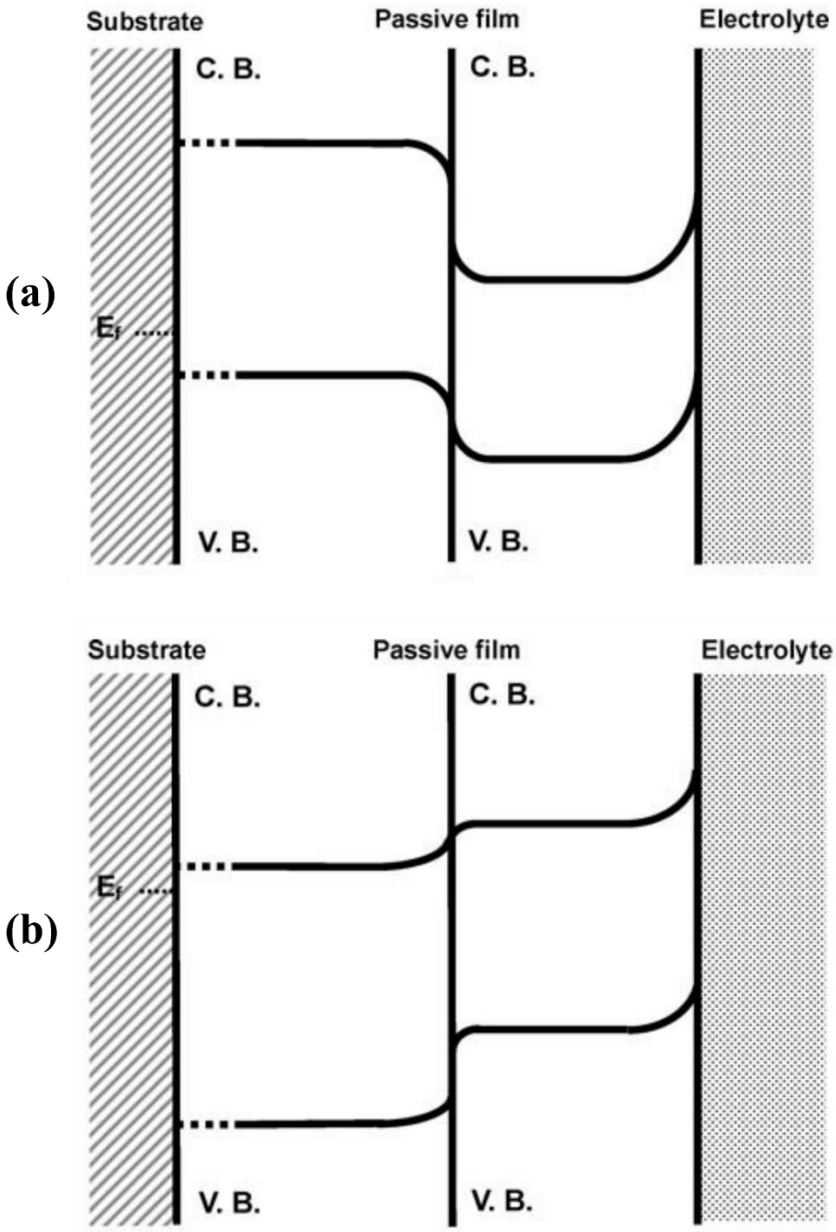

Figure 1.11 Schematic illustrations of the electronic band structure models of passive films on Fe-18Cr in (a) a sulfuric acid solution and (b) a borate buffer solution [83].

Cr-containing alloys are usually corrosion-resistant in various environments due to the protective nature of the passive films where Cr is highly enriched. As the electronic structure and semiconductive properties of passive films on Cr-containing alloys such as Fe–Cr, Ni–Cr, and Co–Cr alloys vary depending on the alloy composition and on the pH of the environment [83, 86, 87], largely different conclusions have been suggested, including from Tsuchiya *et al.* To develop a unified consensus on the passive films on Cr-containing alloys, the role of Cr oxide and hydroxide, which are constituents of the passive films, should be more precisely understood. Therefore, in the present thesis, the author has examined the electronic structures and semiconductive properties of passive films on Cr using photoelectrochemical response and electrochemical impedance spectroscopy. To further support the discussions regarding the data obtained by the electrochemical measurements, valence band spectrum of XPS was also introduced to reveal the valence band edge of the passive films on Cr. The electronic structures and semiconductive properties of passive films on Cr were compared with those of passive films on Ti. Furthermore, a numerical simulation model for the photocurrent transients, which are explained in Fig. 1.10, was also developed to realize a deeper understanding of the electronic structures and semiconductive properties of passive films.

1.6 The purpose and structure of this thesis

The purpose of this thesis is to reveal the electronic band structure of passive films formed on Cr and Ti by electrochemical measurements and surface analytical techniques. In addition, the development of a simulation model of the photocurrent transient, which has often been observed in the photocurrent measurements in literature and in this PhD work, is also presented. The present thesis consists of the following 5 chapters.

Chapter 1 introduces several concepts for the passivity of metals, passive films, and semiconductor electrochemistry. The purpose of this thesis is also described.

Chapter 2 deals with the electronic band structure of passive films formed on Ti in the simulated biological solutions. Furthermore, the superior biocompatibility of Ti is discussed in terms of the electronic band structure of its passive films.

Chapter 3 presents a comparative analysis of the electronic structure of passive films formed on Cr and Ti in a phosphate buffer solution of pH 7.

Chapter 4 provides a numerical simulation model for photocurrent transients, which is based on the generation and recombination of photo-excited charge carriers, and their transport by drift and diffusion. Through the screening of parameters, several properties of passive and anodic films, such as electron mobility, donor density, recombination coefficient, and interfacial reaction coefficient, were acquired.

Chapter 5 summarizes the findings of this thesis.

Reference

1. H. Kania, *Coatings*, **13**, 216 (2023).
2. G. Koch, J. Varney, N. Thompson, O. Moghissi, M. Gould, and J. Payer, *NACE International IMPACT report 2016*, (2016).
3. D. A. Jones, *Corros.*, **2**, 168 (1996).
4. M. Pourbaix, *A. Electrochemical Equi. Sol. 2nd ed*., (1974).
5. K. Ma, R. Zhang, J. Sun, and C. Liu, *Int. J. Corros*, **2020**, 9 (2020).
6. B. Thierry, M. Tabrizian, C. Trepanier, O. Savadogo, and L. H. Yahia, *J. Biomed. Mater. Res.*, **51**, 685 (2000).
7. M. Geetha, A. K. Singh, R. Asokamani, and A. K. Gogia, *Prog. Mater. Sci.*, **54**, 397 (2009).
8. M. T. Mohammed, Z. A. Khan, and A. N. Siddiquee, *Int. J. Chem. Mol. Nucl. Mater. Metall. Eng*, **8**, 726 (2014).
9. J. Pouilleau, D. Devilliers, F. Garrido, S. Durand-Vidal, and E. Mahé, *Mater. Sci. Eng. B*, **47**, 235 (1997).
10. Z. Jiang, X. Dai, T. Norby, and H. Middleton, *Corros. Sci.*, **53**, 815 (2011).
11. W. Xue, B. V. Krishna, A. Bandyopadhyay, and S. Bose, *Acta Biomater.*, **3**, 1007 (2007).
12. J. Pan, D. Thierry, and C. Leygraf, *Electrochim. Acta*, **41**, 1143 (1996).
13. V. Alves, R. Reis, I. Santos, D. Souza, T. d. F. Gonçalves, M. Pereira-da-Silva, A. Rossi, and L. Da Silva, *Corros. Sci.*, **51**, 2473 (2009).
14. J. Guertin, J. A. Jacobs, and C. P. Avakian, *CRC Press*, (2004).
15. M. Seo, R. Saito, and N. Sato, *J. Electrochem. Soc.*, **127**, 1909 (1980).
16. Y. Li, F. Zhou, Y. Ren, and G. Zhou, *Int. J. Electrochem. Sci.*, **17** 221056 (2022).
17. V. Maurice, W. Yang, and P. Marcus, *J. Electrochem. Soc.*, **143**, 1182 (1996).
18. P. Marcus and J. Grimal, *Corros. Sci.*, **33**, 805 (1992).
19. H. Hertz, *A Collection of Articles and Addresses*, 223, (2019).
20. A. Einstein, *Ann Phys*, **17**, 208 (1905).
21. P. Innes, *Proc. R. soc. Lond. Ser. A-Contain. Pap. Math. Phys*, **79**, 442 (1907).
22. K. Siegbahn, *ESCA*, (1967).
23. G. Okamoto, *Corros. Sci.*, **13**, 471 (1973).
24. K. Asami, K. Hashimoto, T. Masumoto, and S. Shimodaira, *Corros. Sci.*, **16**, 909 (1976).

25. K. Asami and K. Hashimoto, *Corros. Sci.*, **17**, 559 (1977).
26. K. Asami, K. Hashimoto, and S. Shimodaira, *Corros. Sci.*, **18**, 151 (1978).
27. J. Castle, L. Hazell, and R. Whitehead, *J Electron Spectros Relat Phenomena*, **9**, 247 (1976).
28. G. Bouyssoux, M. Romand, H. Polaschegg, and J. Calow, *J Electron Spectros Relat Phenomena*, **11**, 185 (1977).
29. P. Marcus, J. Oudar, and I. Olefjord, *J. Micr. Spectrosc. Electron*, **4**, 63 (1979).
30. J. Pan, D. Thierry, and C. Leygraf, *J. Biomed. Mater. Res.*, **28**, 113 (1994).
31. I. Milošev, M. Metikoš-Huković, and H.-H. Strehblow, *Biomater.*, **21**, 2103 (2000).
32. B. Stypula and J. Stoch, *Corros. Sci.*, **36**, 2159 (1994).
33. A. Lim and A. Atrens, *Appl. Phys. A.*, **54**, 343 (1992).
34. A. Yaniv, J. Lumsden, and R. Staehle, *J. Electrochem. Soc.*, **124**, 490 (1977).
35. R. J. Solar, S. R. Pollack, and E. Korostoff, *J. Biomed. Mater. Res.*, **13**, 217 (1979).
36. S. Boudin, J. L. Vignes, G. Lorang, M. Da Cunha Belo, G. Blondiaux, S. Mikhailov, J. Jacobs, and H. Brongersma, *Surf. Interface Anal.*, **22**, 462 (1994).
37. F. Koffyberg and F. Benko, *J. Appl. Phys.*, **53**, 1173 (1982).
38. F. Koffyberg and F. Benko, *J. Electrochem. Soc.*, **128**, 2476 (1981).
39. Y. Matsumoto, J. Kurimoto, Y. Amagasaki, and E. Sato, *J. Electrochem. Soc.*, **127**, 2148 (1980).
40. M. Sukkar, K. Johnson, and H. Tuller, *Mater. Sci. Eng. B*, **6**, 49 (1990).
41. K. Rajeshwar, *Encyclopedia of electrochemistry*, **6**, 1 (2007).
42. H. Gerischer, *Electrochim. Acta*, **35**, 1677 (1990).
43. O. Heaviside. *Electromagnetic theory*, **1**, (1894)
44. E. Warburg, *Ann. Phs.*, **303**, 493 (1899).
45. U. Stimming and J. Schultze, *Electrochim. Acta*, **24**, 859 (1979).
46. R. Thapar and K. Rajeshwar, *Electrochim. Acta*, **28**, 195 (1983).
47. M. Becquerel, *C. R. Acad. Sci. Paris ou CRAS*, **9**, 561 (1839).
48. J. Kruger, *J. Electrochem. Soc.*, **106**, 847 (1959).
49. D. C. Cronemeyer, *Phys. Rev.*, **87**, 876 (1952).
50. W. Brattain and C. Garrett, *Bell Syst. Tech. J.*, **34**, 129 (1955).
51. W. W. Gärtner, *Phys Rev.*, **116**, 84 (1959).
52. H. Harten, *Phys Chem Solids.*, **14**, 220 (1960).
53. H. Gerischer, *J. Electrochem. Soc.*, **113**, 1174 (1966).
54. H. Tributsch and H. Gerischer, *Bunsenges. Phys. Chem.*, **73**, 850 (1969).

55. E. Oshe and I. Rozenfeld, *Elektrokhimiya*, **4**, 1200 (1968).
56. S. Wilhelm, K. Yun, L. Ballenger, and N. Hackerman, *J. Electrochem. Soc.*, **126**, 419 (1979).
57. K. L. Hardee and A. J. Bard, *J. Electrochem. Soc.*, **124**, 215 (1977).
58. J. F. McAleer and L. M. Peter, *Faraday Discuss.*, **70**, 67 (1980).
59. K. Leitner, J. Schultze, and U. Stimming, *J. Electrochem. Soc.*, **133**, 1561 (1986).
60. T. Burleigh, *Corros.*, **45**, 464 (1989).
61. S. Virtanen, P. Schmuki, H. Böhni, P. Vuoristo, and T. Mäntylä, *J. Electrochem. Soc.*, **142**, 3067 (1995).
62. J. Birch and T. Burleigh, *Corros.*, **56**, 1233 (2000).
63. H. Gerischer, *Corros. Sci.*, **29**, 257 (1989).
64. H. Gerischer, *Corros. Sci.*, **29**, 191 (1989).
65. H. Gerischer, *Corros. Sci.*, **31**, 81 (1990).
66. N. Sato, *Electrochemistry at metal and semiconductor electrodes*, (1998).
67. S. Zhang, L. Jia, and T. Yu, *Electrochim. Acta*, **89**, 253 (2013).
68. L. Peter, J. Li, and R. Peat, *J. electroanal. Chem. Interfacial Electrochem.*, **165**, 29 (1984).
69. K. Azumi, T. Ohtsuka, and N. Sato, *Corros. Sci.*, **31**, 715 (1990).
70. J. L. McNatt, *Phys. Rev. Lett.*, **23**, 915 (1969).
71. M. Shi, T. Qiu, B. Tang, G. Zhang, R. Yao, W. Xu, J. Chen, X. Fu, H. Ning, and J. Peng, *Micromachines*, **12**, 80 (2021).
72. H. Jang, C. Park, and H. Kwon, *Electrochim. Acta*, **50**, 3503 (2005).
73. S. M. Wilhelm and N. Hackerman, *J. Electrochem. Soc.*, **128**, 1668 (1981).
74. Y. Mito, M. Ueda, and T. Ohtsuka, *Corros. Sci.*, **51**, 1540 (2009).
75. F. Di Quarto, S. Piazza, and C. Sunseri, *Corros. Sci.*, **31**, 721 (1990).
76. S. Fujimoto, O. Chihara, and T. Shibata, *Mater. Sci. Forum.*, **289-292**, 989 (1998).
77. J. Kim, E. Cho, and H. Kwon, *Electrochim. Acta.*, **47**, 415 (2001).
78. H. Tsuchiya, S. Fujimoto, O. Chihara, and T. Shibata, *Electrochim. Acta.*, **47**, 4357 (2002).
79. L. Forro, O. Chauvet, D. Emin, L. Zuppiroli, H. Berger, and F. Lévy, *J. Appl. Phys.*, **75**, 633 (1994).
80. L. Kavan, M. Grätzel, S. Gilbert, C. Klemenz, and H. Scheel, *J. Am. Chem. Soc.*, **118**, 6716 (1996).

81. A. Di Paola, M. Bellardita, R. Ceccato, L. Palmisano, and F. Parrino, *J. Phys. Chem. C*, **113**, 15166 (2009).
82. N. Sato, *Corros.*, **45**, 354 (1989).
83. H. Tsuchiya, S. Fujimoto, and T. Shibata, *J. Electroceramics*, **16**, 49 (2006).
84. W. Ye, Y. Li, and F. Wang, *Electrochim. Acta*, **54**, 1339 (2009).
85. B. Lu, Z. Chen, J. Luo, B. Patchett, and Z. Xu, *Electrochim. Acta*, **50**, 1391 (2005).
86. N. Hakiki, S. Boudin, B. Rondot, and M. D. C. Belo, *Corros. Sci.*, **37**, 1809 (1995).
87. N. Sato, *Corros. Sci.*, **31**, 1 (1990).

Chapter 2

Band structures of passive films on titanium in simulated bioliquids determined by photoelectrochemical response: Principle governing the biocompatibility

2.1 Introduction

Titanium (Ti) and its alloys are widely used as implant devices in medicine and dentistry due to their excellent corrosion resistance and high specific strength [1]. Their good tissue compatibility is well established through significant evidence from basic research and high clinical performance. For example, in orthopedics, bone screws and bone nails consisting of Ti alloys usually form calluses and assimilate into bone tissue after long-term implantation, inducing refracture of the bone during retrieval [2]. This is because of the good compatibility of Ti alloys with hard tissues. Many studies on the hard-tissue compatibility of Ti have been performed, and detailed information can be found in the literature [1, 3]. The initial reaction at the interface directly influences the biocompatibility of the material. Therefore, biocompatibility is governed by the surface properties of the material. However, the principle and mechanism of the good tissue compatibility of Ti among metals have not been completely elucidated, despite numerous studies conducted on biological reactions.

The surface of metallic Ti is covered by a passive film, which contributes to its excellent corrosion resistance. The passive film on Ti is mainly an extremely thin amorphous TiO_2 containing small amounts of Ti_2O_3 and TiO, along with water and hydroxyl groups [4-7]. In addition, as the composition is graded in the passive film, more Ti^{4+} and OH^- ions appear near the surface of the film [6]. The formation process of the passive film has been discussed elsewhere [8] and the chemical state of the passive film has also been precisely investigated [9]. It

has been established that the composition, structure, and chemical state of the passive film on Ti are different from those of the crystalline TiO_2 ceramics. For example, the adsorption kinetics of calcium and phosphate ions onto the passive films differ from those onto TiO_2 ceramics [10].

In this regard, the bandgap energy, E_g, which is equivalent to the energy difference between the valence and conduction bands of TiO_2 crystalline ceramics is usually evaluated by the optical absorption edge. It is well known that the reactivity of TiO_2 ceramics is governed by E_g, and continuous efforts to decrease E_g have been made to activate their photocatalyst performance [11]. The E_g of a photocatalyst decreases as its optical response shifts to longer excitation wavelengths. From this viewpoint, the passive film on Ti already contains oxygen defects because of its nonstoichiometric composition. Therefore, the difference in the surface properties between the passive films on Ti and TiO_2 ceramics is probably due to the difference in their E_gs. The E_g of passive films on Ti after anodic oxidation and thermal oxidation has been investigated by the photoelectrochemical response in borate buffer solution, artificial sea water, and sulfuric acid [12-14] because the conventional techniques employed for oxide ceramics, such as ultraviolet absorption, cannot be used for thin passive films on Ti.

In this study, the E_g values of passive films formed on Ti in simulated bioliquids, Hanks' solution and 0.9 % NaCl aqueous solution, were evaluated using the photoelectrochemical response at potentials as close as possible to the open circuit potential (OCP). In addition, X-ray photoelectron spectroscopy (XPS) was performed to understand the effect of the chemical composition and chemical state of the passive films on the photoelectrochemical properties. This research will lead to deeper understanding of the properties of passive films on Ti in the human body.

2.2 Experimental

2.2.1 Specimen

Commercially or industrially pure titanium (ISO grade 2; > 99.5% Ti; Test Materials, Tokyo, Japan) rods (8 mm in diameter) were cut into disks (1.5 mm in thickness). In the case of OCP measurement and XPS, the disks were polished with SiC paper, followed by mirror finishing with a 0.04 μm SiO_2 suspension. After polishing, the Ti disks were ultrasonically cleaned twice in acetone and once in isopropanol for 10 min each. The Ti disks were immersed in ultrapure water for 24 h to stabilize the passive films. The disks were then fixed in a polytetrafluoroethylene holder with an o-ring, exposing an area of 0.278 cm^2 to the electrolyte. For photoelectrochemical measurements, Ti was connected to a lead wire by welding. The disks and connected parts were embedded in epoxy resin, and the surface was polished with SiC paper, followed by mirror finishing with a 0.25 μm diamond suspension. After polishing, the specimens were ultrasonically cleaned sequentially in acetone, ethanol, and deionized water for 10 min each and immediately used for subsequent experiments.

2.2.2 Electrolytes

Hanks' solution without glucose (Hanks) was prepared using reagent-grade chemicals and ultrapure water. The composition of the Hanks was similar to that of extracellular fluid which contains the following ions in the stated concentrations: Na^+ = 142, K^+ = 5.81, Mg^{2+} = 0.811, Ca^{2+} = 1.26, Cl^- = 145, PO_4^{3-} = 0.778, SO_4^{2-} = 0.811, and CO_3^{2-} = 4.17 (mmol/L). The pH of Hanks was 7.4 after preparation and did not change during experiments at 37 ℃. A 0.9 mass% NaCl solution (saline) was also used for comparison. The pH of saline is 6.4 just after preparation at 37 ℃.

2.2.3 Electrochemical measurements

In the present study, two different types of electrochemical measurements were performed: the open circuit potential (OCP) measurement and the photoelectrochemical response. These measurements were conducted using a conventional three-electrode configuration cell equipped with a Ag/AgCl reference electrode and a Pt counter electrode. In the OCP measurement, the variations in the OCP of the specimens with time were monitored for 72 h in Hanks and saline solutions at 37 ℃. In the photoelectrochemical response, the specimens were immersed in Hanks and saline solutions for 10 min and then passivated by polarizing the specimens at the film formation potentials, E_fs, of −0.2, −0.1 and 0 $V_{Ag/AgCl}$ for 1 h to form a stable passive film. After the passive film was formed, monochromatic light from a 150 W xenon arc lamp and a grating monochromator was irradiated to the passivated specimen surfaces in the electrochemical cell through a quartz window. Current changes during light irradiation of 20 s were recorded as photocurrents and the photocurrent measurement was performed at the E_f by changing the wavelength of the incident light from 250 to 450 nm with the step of 10 nm. Then the applied potential was stepwisely changed with the interval of 0.1 V in the less noble direction and the measurements were repeated at each measuring potential, E_m. Both solutions used in this study were deaerated with N_2 gas for at least 2 h in the electrochemical cell prior to all the electrochemical measurements and the deaeration was continued during measurements.

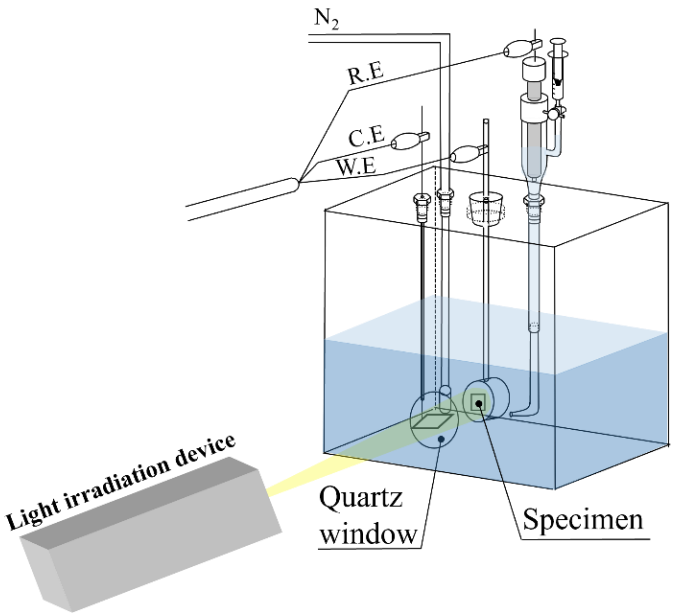

Figure 2.1 Schematic diagram of a three-electrode cell for the photoelectrochemical response.

2.2.4 X-ray photoelectron spectroscopy

After polarization at each E_f in both Hanks and saline for 1 h, the specimens were rinsed with ultrapure water to remove all chemical species that are incorporated out the specimen surfaces, and dried by a stream of N_2 gas. Immediately after the drying, the specimens were inserted in the pre-evacuation chamber of the XPS machine (JPS-9010MC, JEOL, Tokyo, Japan). Mg Kα line (1253.6 eV) was employed as the X-ray source. The binding energies were calibrated with electron energy of C1s peak (285.0 eV) originating from so-called contamination hydrocarbon. The background of peaks was subtracted with Shirley's method [19]. The composition and thickness of the passive films formed by the polarization were calculated according to literature [7, 20-23]. The results were statistically evaluated using one-way ANOVA with a significance of $p < 0.05$.

2.3 Results

2.3.1 Variations in open circuit potential

Figure 2.2 presents variations in the OCP of Ti in Hanks and saline over time. Noted that the pH of Hanks remained at 7.4, and no precipitation was observed during the OCP measurement, whereas the pH of saline gradually decreased to 5.7 after 6 h and 5.8 after 72 h. Immediately after the measurements commenced, the OCP drastically decreased in both solutions, followed by a gradual increase with time. After 72 h, the OCP was approximately −0.2 V in Hanks whereas −0.1 V in saline. The OCP in saline was always more noble than that in Hanks during the monitoring, because the pH of saline was lower than that of Hanks.

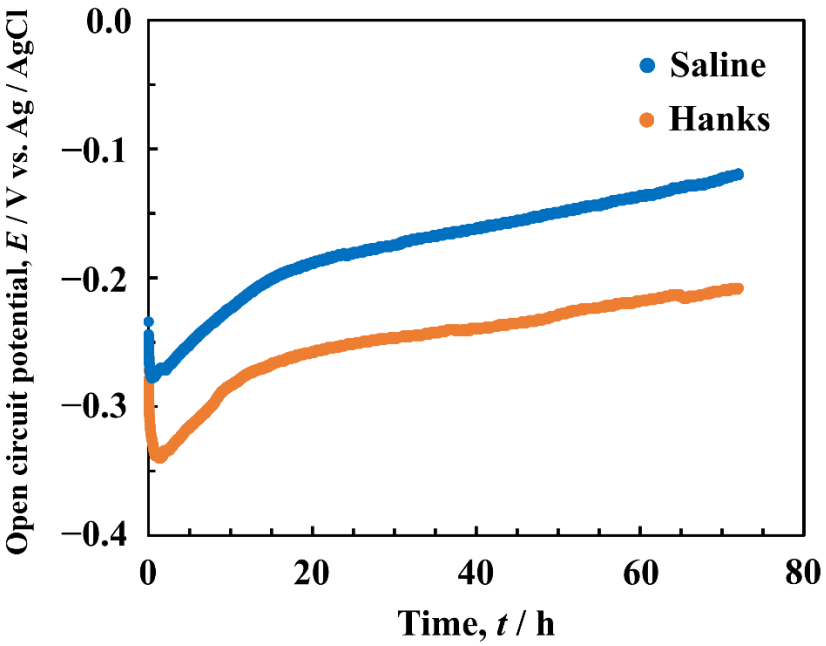

Figure 2.2 Variations in open circuit potential (OCP) of Ti in Hanks and saline for 72 h.

2.3.2 Photoelectrochemical response

A typical photocurrent transient observed for passive films formed on Ti in Hanks and saline is illustrated in Fig. 2.3. The shape of all the photocurrent transients observed in the present study was similar to the one in this figure, that is, the current rapidly increases immediately after light irradiation, reaches a peak, and then drastically decreases. After the drastic decrease, the current gradually converges to a steady-state value. When the irradiation is terminated, the current rapidly drops once and then recovers back to the original value. The steady-state current was defined as photocurrent, I_{ph}, and used for analysis in the present work.

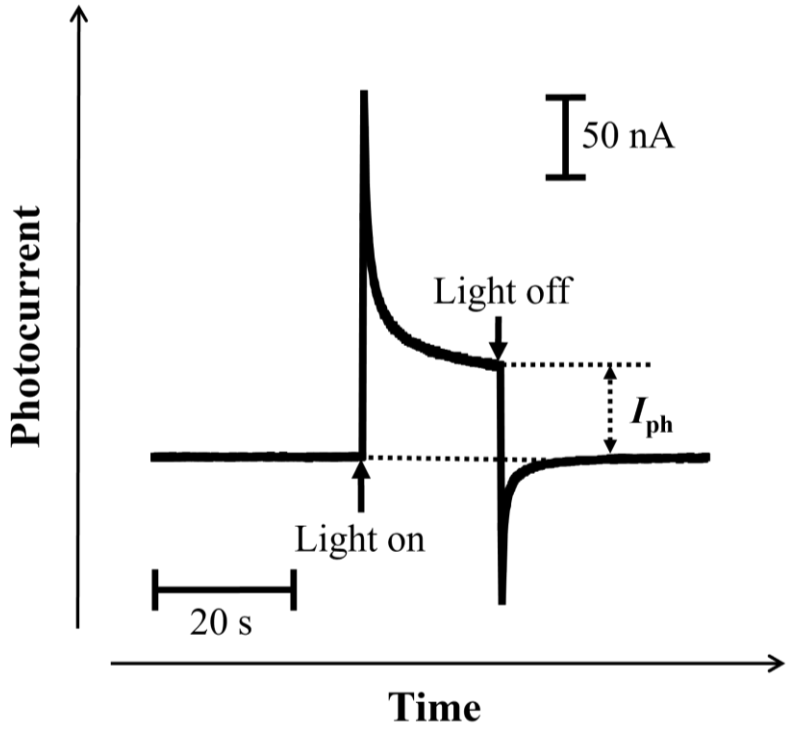

Figure 2.3 An example of photocurrent transient generated with the light on and off for a passive film on Ti.

Figure 2.4 shows the photocurrent spectra of the passive films formed on Ti in Hanks and saline solutions. The photocurrent varied depending on the E_m and the wavelength of the incident light, in both cases. The photocurrent spectra were normalized for further analysis because the intensity of the light is not constant for each wavelength. Assuming that the photoexcitation takes place as an indirect transition, the photocurrent spectra were normalized as photoelectrochemical action spectra using the following equation [15-18].

$$\left(I_{ph} \cdot hv/I_0\right)^{1/2} = S(hv - E_G), \tag{2.1}$$

where I_0 and hv are the intensity and photon energy of the incident light, respectively, S is constant which exhibits the slope of the photoelectrochemical action spectrum and reflects the amplitude and direction of photocurrent, and h is Planck's constant. Band gap energy (E_g) can be estimated as the photon energy value where the $(I_{ph} \cdot hv/I_0)^{1/2}$ equals zero. By replotting the photocurrent spectra in Fig. 2.4, photoelectrochemical action spectra, E_{ph}, were obtained, as shown in Figs. 2.5 and 2.6, corresponding to the spectra in Hanks and saline solutions, respectively. The bottom figures show enlarged views of the lower photon energy region. In the case of Hanks solution, the photoelectrochemical action spectra did not exhibit a straight line with a constant S_k, instead gradually changed. When the photocurrent is generated from a uniform composition layer, the direction of the photocurrent does not change at a fixed potential, even if the photon energy of the incident light is changed.

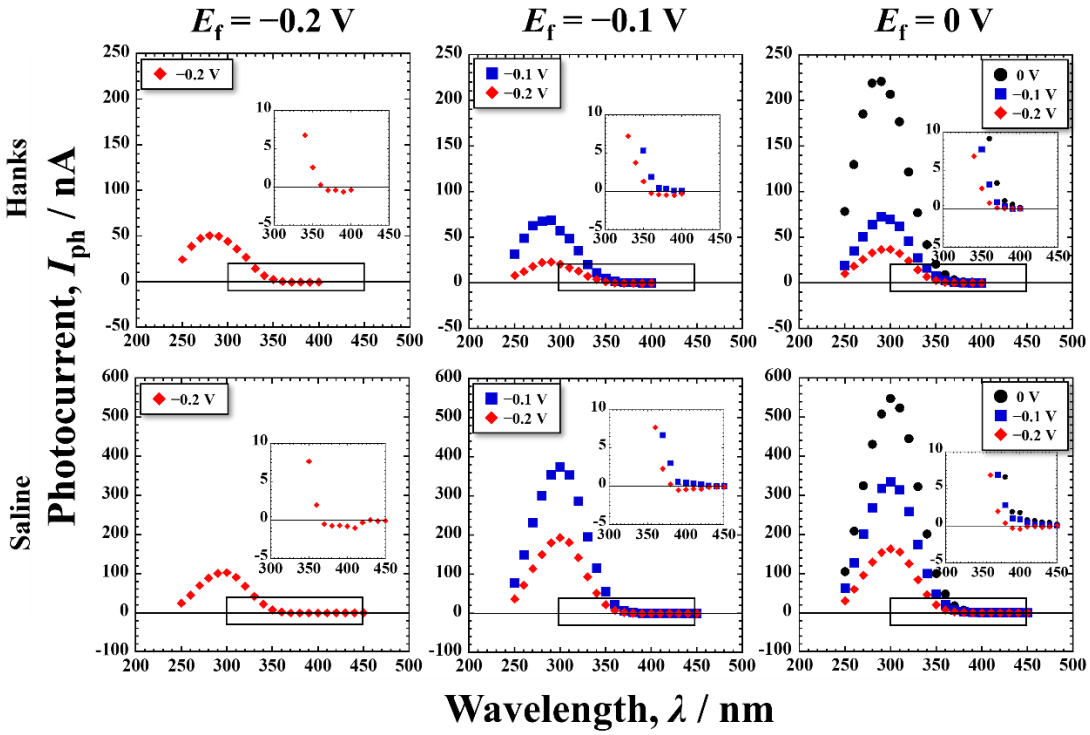

Figure 2.4 Photocurrent spectra of the passive films formed on Ti in Hanks and saline solutions.

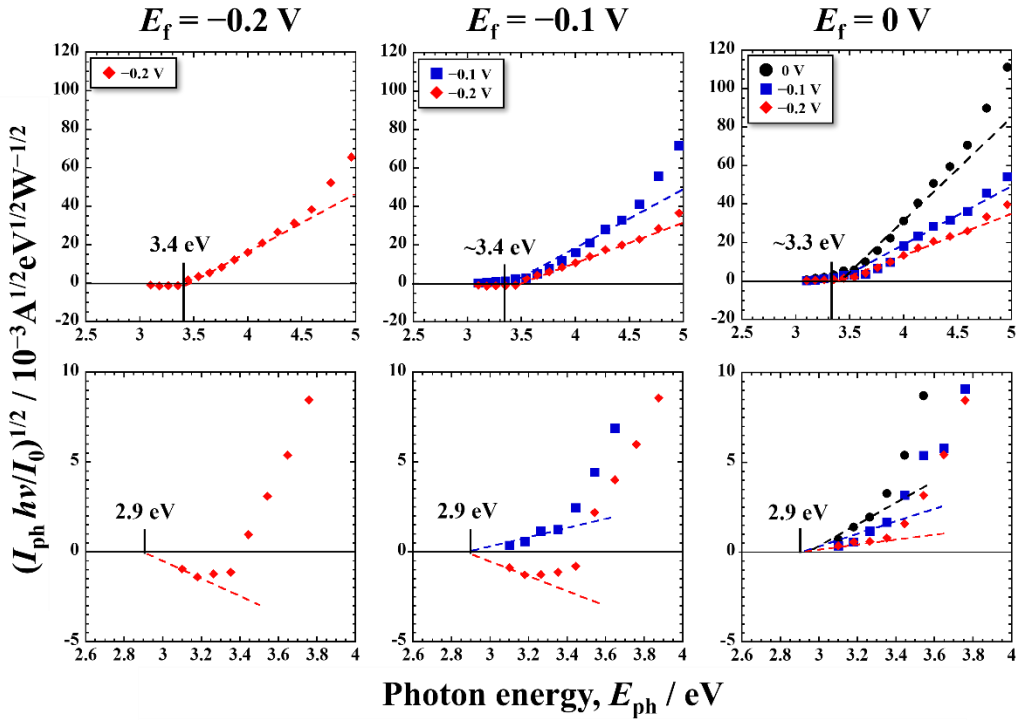

Figure 2.5 Photoelectrochemical action spectra calculated from the steady-state photocurrent in Hanks shown in Fig. 2.4.

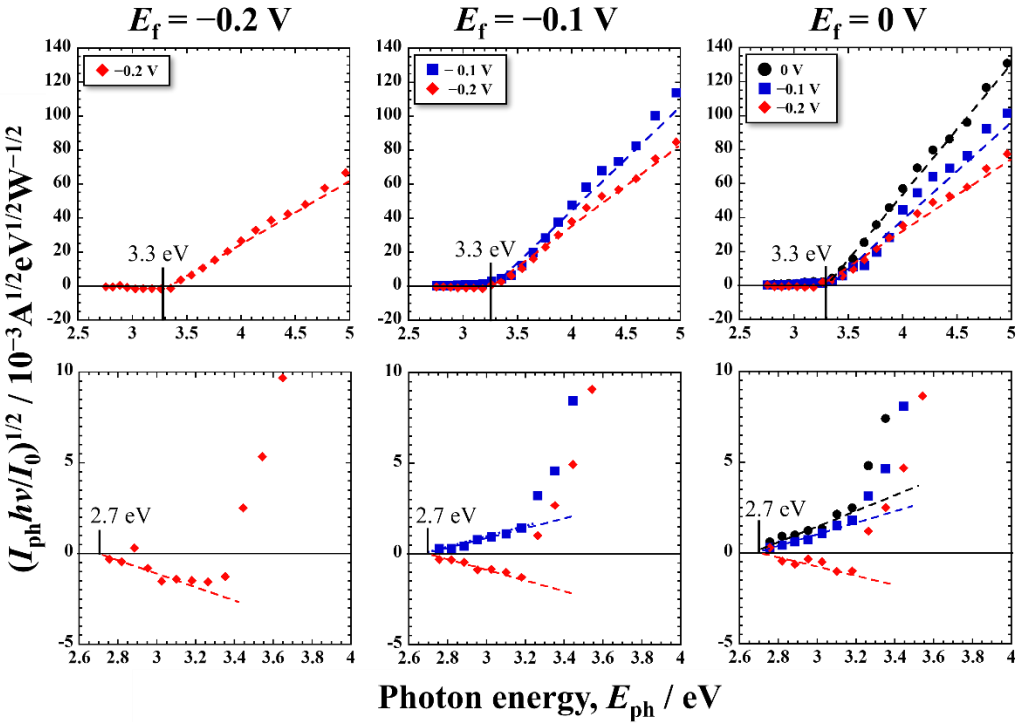

Figure 2.6 Photoelectrochemical action spectra calculated from the steady-state photocurrent in saline shown in Fig. 2.4.

On subtracting the photoelectrochemical response of a component with lower band gap energy from the original photoelectrochemical action spectra, the photoelectrochemical action spectra for the other component with higher band gap energy are obtained in the higher photon energy region. The extrapolation of the remaining spectra on the horizontal axis represents a larger E_g component. For Hanks solution, the larger component of E_g was in the range of 3.3 – 3.4 eV, whereas the smaller component of E_g was estimated from the bottom figures in Fig. 2.5. This value was identical for all the examined specimens in Hanks solution. In the case of saline, the E_gs were determined to be 3.3 eV and 2.7 eV. The band gap values in Hanks were slightly larger than those in the saline.

2.3.3 X-ray photoelectron spectroscopy

Titanium and oxygen were detected in all the specimens. Carbon and nitrogen were also detected in the contaminated layer. In addition to the above elements, calcium and phosphorus were detected in specimens polarized in Hanks. No peak originating from CO_3^{2-} was observed at approximately 289.6 eV [24]. The Ti 2p, O 1s, Ca 2p, and P 2p spectra obtained from passivated Ti at 0 V are organized in Fig. 2.7. In the following, the characteristics of each spectrum is briefly described and the effect of polarization on the chemical structure of surface film is also discussed by comparing bare Ti where a native oxide is present and the passivated specimens where a passive film is formed. Figure 2.7 (a) shows the deconvolution of the Ti 2p spectrum. As indicated, the Ti 2p spectrum consists of four doublets corresponding to the metallic state of Ti^0 and the oxidized states of Ti^{2+}, Ti^{3+}, and Ti^{4+}. The binding energy of each valence state of titanium was determined from the data previously reported [5]. The binding energy of the peak originating from Ti^{4+} before polarization was 458.8 eV, and after polarization it was 458.8 – 459.0 eV in both Hanks and saline. In addition, the $[Ti^{4+}]/([Ti^{2+}] + [Ti^{3+}] + [Ti^{4+}])$ ratio obtained from the titanium surfaces before and after polarization, which was calculated from the integrated peak intensity of each component, was almost constant in the range from 0.78 to 0.82 in Hanks and saline solutions. As presented in Fig. 2.7 (b), the O 1s spectrum is composed of three peaks originating from oxide (O^{2-}), hydroxyl groups or hydroxide (OH^-), and adsorbed water or hydrate (H_2O) [25]. Noted that a peak from the phosphate oxygen overlaps with the OH^- peak, but the proportion of the former was small. Figure 2.8 summarizes the $[OH^-]/[O^{2-}]$ ratios on titanium surfaces after polarization at different E_fs in Hanks and saline solutions. The ratio before the polarization is also included as comparison. The ratios increased after polarization in both solutions. Although the ratios obtained at −0.2 V were same for both solutions, the ratio for Hanks solution significantly decreased with increasing the E_f, whereas that for saline solution was almost constant independent of the E_f, indicating that the ratio for saline solution was significantly larger than

that for Hanks at 0 V. The peak at the binding energy of 347.6 – 347.7 eV was found in the Ca $2p_{3/2}$ spectrum (Fig. 2.7 (c)), indicating that calcium existed as Ca^{2+} in the passive film formed in Hanks [26]. Whereas the peak at 133.9 – 134.2 eV in the P 2p spectrum revealed that phosphorus was also present as phosphate (Fig. 2.7 (d)) in the passive film formed in Hanks [22, 27]. The adsorption process of Ca and P on the passive film formed in Hanks' solution was reported by Hanawa [28]. Ca ions in Hanks' solution modify the Ti surface and cause the adsorption of phosphate ions. Ca and P ions adsorbed on the surface can be incorporated into the passive film. At the same time, Ca ions can react with P ions in the near-surface solution to precipitate calcium phosphate on the surface. Therefore, it can be concluded that the calcium and phosphorus are in the passive film as Ca and P ions and sometimes form calcium phosphate on the passive film. The effects of Ca and P on the Ti passive film are discussed later.

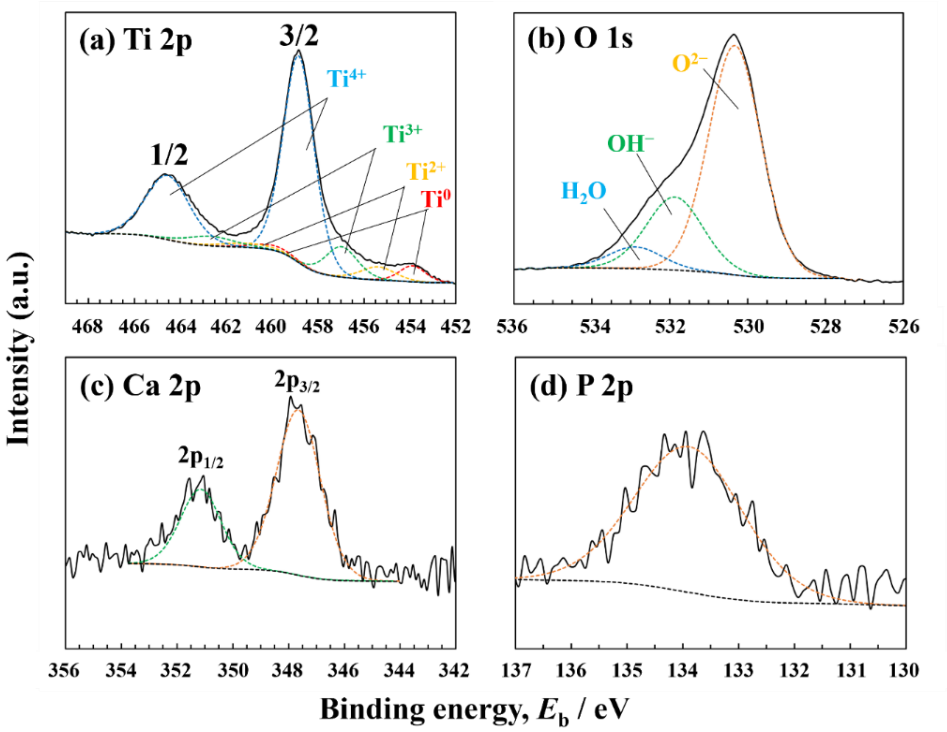

Figure 2.7 (a) Ti 2p, (b) O 1s, (c) Ca 2p, and (d) P 2p spectra obtained from Ti after polarization at 0 V in Hanks solution for 1 h.

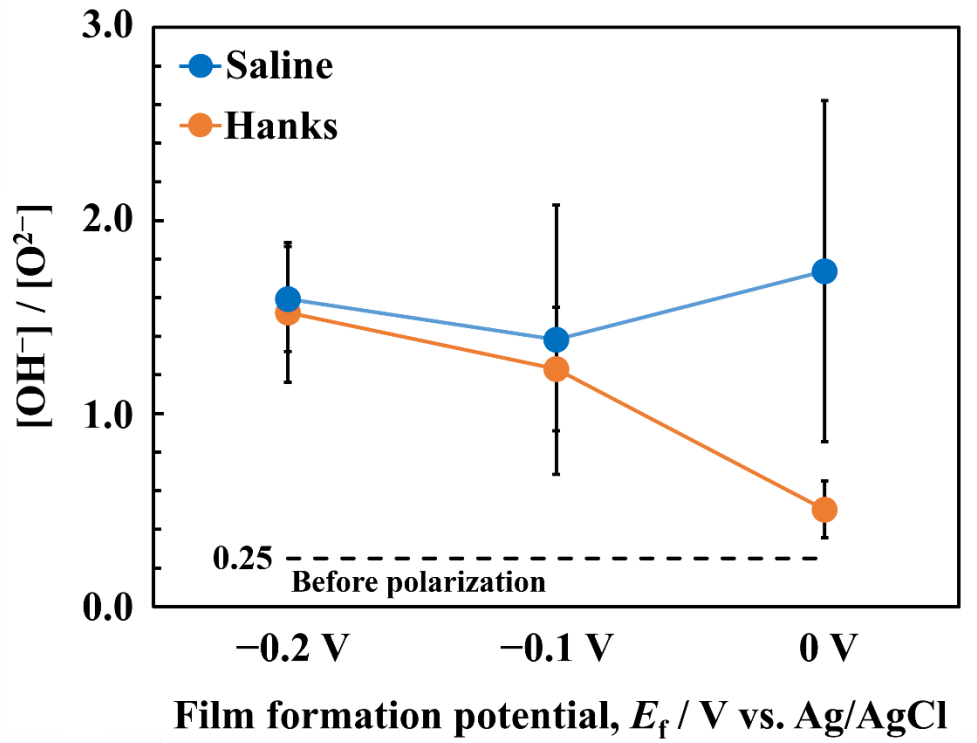

Figure 2.8 $[OH^-]/[O^{2-}]$ ratios calculated form O 1s spectra of Ti before and after polarization at each film formation potential, E_f (Mean±SD, n = 3).

The relative concentrations of Ti, O, Ca, and P in the passive film formed at the E_gs were calculated by assuming that the total amount of these elements was 100 at.%, as presented in Table 2.1. It is evident that after polarization in Hanks solution, as described above, calcium and phosphate ions were incorporated into the passive film, but their amounts did not significantly change with increasing the E_f. The ratios of calcium concentration to phosphorus concentration, [Ca]/[P] slightly increased with the E_f, although there is no significant difference. The thickness of the passive films increased slightly after polarization, and the thickness in Hanks solution was comparable to or smaller than that in saline solution, despite the incorporation of calcium and phosphate ions or the formation of calcium phosphate.

Table 2.1 Relative concentrations of elements, [Ca]/[P] ratios, and thickness of the passive films formed on Ti (Mean±SD, n = 3).

Electrolyte	Film formation potential, E_f / V	Relative concentration (at.%)				[Ca]/[P]	Thickness, d / nm
		Ti	O	Ca	P		
Before polarization	-	28.8±1.2	71.2±1.0	-	-	-	5.9±0.2
Hanks	−0.2	13.2±1.6	85.4±2.1	0.5±0.3	1.0±0.4	0.5±0.2	6.5±0.2
	−0.1	14.4±2.2	84.1±2.2	0.6±0.2	1.0±0.1	0.6±0.3	6.4±0.4
	0	22.8±1.5	76.1±1.9	0.5±0.1	0.7±0.2	0.7±0.2	6.3±0.1
Saline	−0.2	14.1±2.4	85.9±2.4	-	-	-	6.4±0.4
	−0.1	11.0±2.5	89.0±2.5	-	-	-	6.9±0.4
	0	13.5±6.5	86.5±6.5	-	-	-	6.9±0.6

The valence-band energy-region spectrum obtained from the passivated Ti at 0 V (the valence-band XPS spectrum) is presented in Fig. 2.9. The spectrum appears due to the superimposition of those derived from the passive film and the Ti substrate. It is reported that in anatase, the valence-band spectrum consists of two peaks at ~ 6 and ~ 8 eV, which correspond mainly to π (non-bonding) and σ (bonding) of O 2p orbitals, respectively [29]. In addition, the 3σ orbital of OH^- appears at a binding energy of ~ 10.8 eV [30]. The water molecule and 3σ orbital of the dissociated water lie at approximately 13 and 11 eV, respectively [31]. The highest energy of the valence-band, E_v, for the passive film against Fermi energy, E_F, was determined by linearly extrapolating the fermi-level-side slope of the valence-band spectrum to the baseline [32]. The E_vs were estimated as 2.8 – 2.9 eV in Hanks and 2.8 – 3.0 eV in saline, whereas that for the polished Ti without polarization was 2.8 eV.

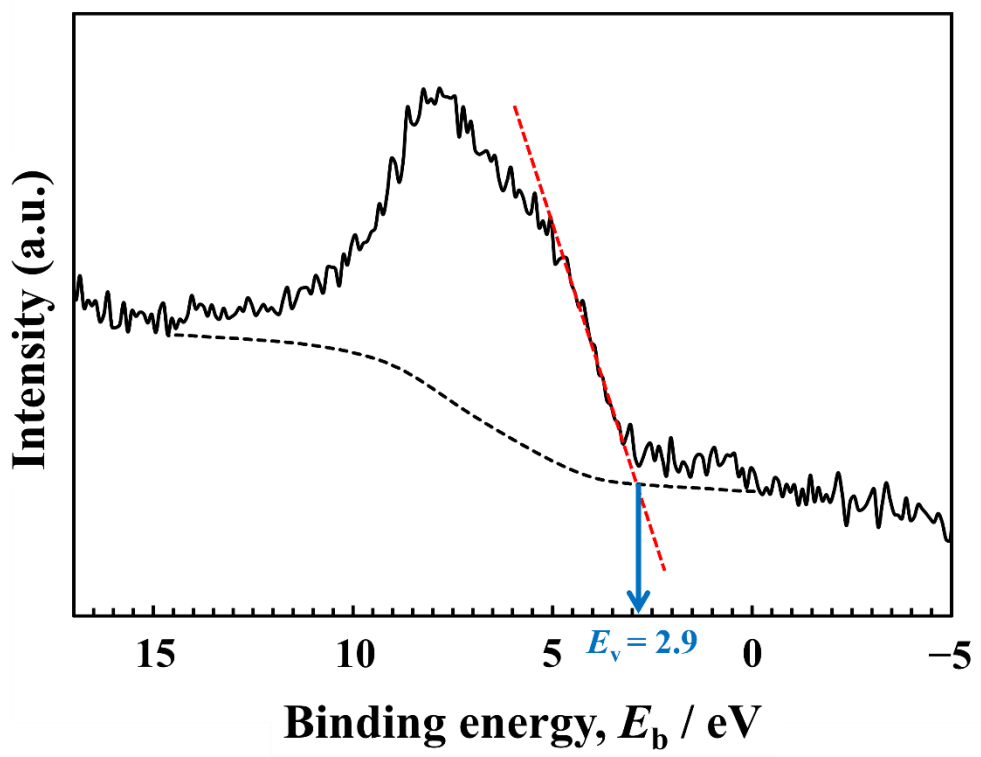

Figure 2.9 Valence-band region spectra of Ti after polarization at 0 V in Hanks for 1 h and the determination of the maximum energy of valence-band, E_v.

2.4 Discussion

XPS results revealed that the passive films on Ti consisted mainly of very thin TiO_2 containing small amounts of Ti_2O_3 and TiO, along with hydroxyl groups and water (Fig. 2.7). These results are in accordance with those of previous studies [4-7]. The passive films on Ti is considered to be non-stoichiometric TiO_2 containing Ti_2O_3 and TiO that are electro-conductive materials. However, the effect of Ti_2O_3 and TiO on the resultant E_gs is unclear in this study. On the other hand, the composition is probably graded; more Ti^{4+} and OH^- exist near the surface of the film [6], and a large number of hydroxyl groups were detected using XPS. Therefore, similar to the passive film formed on Fe-Cr alloys, the passive films on Ti are assumed to consist of two layers [33]: inner oxide and outer hydroxide. After polarization, the $[OH^-]/[O^{2-}]$ ratios increased in the passive films formed in both Hanks and saline solutions (Figure 2.8). The ratio in Hanks solution significantly decreased with E_f, probably caused by the formation of calcium phosphate. As a result, the relative concentration of O at 0 V in Hanks solution was significantly smaller than those under other conditions (Table 2.1) because of the decrease of OH^-. The $[OH^-]/[O^{2-}]$ ratios of the passive films on Co-28Cr-6Mo alloy (ASTM F799-95), Co-Ni-Cr-Mo alloy (ASTM F562), and 316 L stainless steel were 2.9, 2.7, and 1.93, respectively, even before polarization [34-36]. Therefore, the $[OH^-]/[O^{2-}]$ ratio in the passive films on Ti was much smaller than those on the Co-Cr alloys and 316L stainless steel. Although the thickness of the passive films on Ti is much larger than those on Co-Cr alloys and 316L stainless steel, the relative thickness of the hydroxide layer to the entire thickness of the passive films and the relative amount of hydroxyl groups are found to be smaller. The thickness of the passive film was increased by 0.4 – 1.0 nm by polarization (Table 2.1). As the concentrations of Na^+ and Cl^- were almost the same in Hanks and saline, and other elements contained in Hanks were not contained in saline, the difference between the passive films formed in Hanks and those formed in saline can be the incorporation of calcium and phosphate ions or the formation of calcium phosphate in Hanks.

The E_gs of the inner layer in the passive films formed in Hanks were comparable or slightly larger than that in saline, independent of the E_f and E_m (Figs. 2.5 and 2.6). Interestingly, the E_gs of the outer layer were identical in each solution: for all the E_f and E_m, 2.9 eV in Hanks and 2.7 eV in saline, that is, the E_g of the hydroxide layers formed in Hanks was also larger than that in saline. It has been reported that the E_g of hydroxyapatite was determined experimentally as > 6 eV and theoretically as 4.95 eV [36], whereas other studies reported 5.4 eV [38] and 4.51 eV [39]. In addition to hydroxyapatite, the E_gs of α-tricalcium phosphate (TCP) and that of β-TCP are reported as 4.89 and 5.25 eV, respectively [39]. These values are much larger than those of TiO_2. Therefore, it is found that the formation of calcium phosphate in Hanks probably increases E_g of the inner and outer layers.

As mentioned above, the E_g of the outer layer is much smaller than that of the inner layer in the passive films. The passive films on Ti behaved as an n-type semiconductor. However, the photocurrents in the lower photon energy region obtained for the passive films formed in both solutions showed negative values when the photocurrent spectrum measured at the E_m of −0.2 V (Figs. 2.5 and 2.6). The author assumes that the outer layer, the E_g of which is smaller compared to that of the inner layer, is an n-type semiconductor, and that the outer layer generates space charge layers at both the film / electrolyte interface and the outer layer / inner layer interface. The change in the direction of the photocurrents from positive to negative shown in Figs. 2.5 and 2.6 can be attributed to opposite slopes of the two space charge layers. This has been reported in the passive films on Fe-Cr alloy with a p-type inner layer and an n-type outer layer [18]. The same phenomenon was observed in this study, even though both the inner and outer layers were n-type. Further discussion is required for comprehension of this observation.

The E_g of the passive film on Ti formed in H_2SO_4 is reported as 3.25 ± 0.05 eV [12], whereas that of the film formed in artificial seawater is 3.4 – 3.7 eV and that in borate buffer solution is 3.1 eV. Meanwhile, the E_g values of the passive films formed in Hanks and saline in

this study, 3.2 – 3.4 eV, were almost the same as those in previous studies. The E_g of TiO_2 ceramics, rutile and anatase, are 3.0 eV and 3.2 eV, respectively. Therefore, E_g of the passive film formed by polarization is comparable to or larger than that of TiO_2 ceramics, while in the outermost surface of the passive film, it is smaller than that of TiO_2 ceramics.

From the above results and discussion, the electronic band structures of the passive films formed on Ti in Hanks and saline solutions are proposed in Fig. 2.10. The band structure of the outer hydroxide layer was based on the previous studies of Fujimoto *et al.* [16-18]. Considering the results that the E_gs of the inner oxide layer formed in Hanks and saline solutions were 3.3 – 3.4 eV and 3.3 eV, respectively, and that the energy differences between the Fermi level of the Ti substrate and the highest energy of the valence-band of the inner oxide layers, E_v, were 2.8 – 2.9 eV in Hanks and 2.8 – 3.0 eV in saline. Therefore, the lowest energy of the conduction band, E_c, against E_F in Hanks was higher than that in saline.

Zirconium (Zr) forms a highly stable and protective passive film, and the reactivity of Zr is much lower than that of Ti [40]. The passive film on Zr consists mainly of ZrO_2 with hydroxyl groups. In the case of the passive film on Zr, the E_g is 3.01 – 3.47 eV in the outer hydroxide layer and 4.44 – 4.91 eV in the inner oxide layer [41]. The E_gs of Zr oxide are estimated as 4.27 – 4.93 eV by theory and 5.78 – 6.1 eV by experiment that vary according to the crystal systems [42]. These values are much larger than those for TiO_2 and the passive film on Ti. Therefore, the reactivity of a material can be determined based on E_g. The E_g values in the outermost layer are much smaller than those of TiO_2 crystalline ceramics (rutile and anatase) whereas the values in the inner layer are slightly larger than or almost the same as those of TiO_2 ceramics. A very thin and non-stoichiometric composition probably reduces the E_g. Therefore, differences in the composition, structure, and chemical state of passive films influence E_g, and their thinness and non-stoichiometric composition decrease E_g. The decrease in the E_g of a material activates its reactivity. The excellent biocompatibility of Ti among the metals may be induced by the low E_g of the outermost surface layer in the passive film. Calcium phosphate is regularly formed on Ti,

but not on TiO_2. Calcium phosphate formation kinetics on Ti are distinct from those on TiO_2 crystalline ceramics [10]. The E_g values of the outermost surface of the passive film formed on Ti are smaller than those of the TiO_2 ceramics, rutile (E_g = 3.0), and anatase (E_g = 3.2). Therefore, the Ti surface is more reactive with the surrounding environment than the TiO_2 ceramic surface. This reactivity is probably one factor contributing to the excellent biocompatibility of Ti.

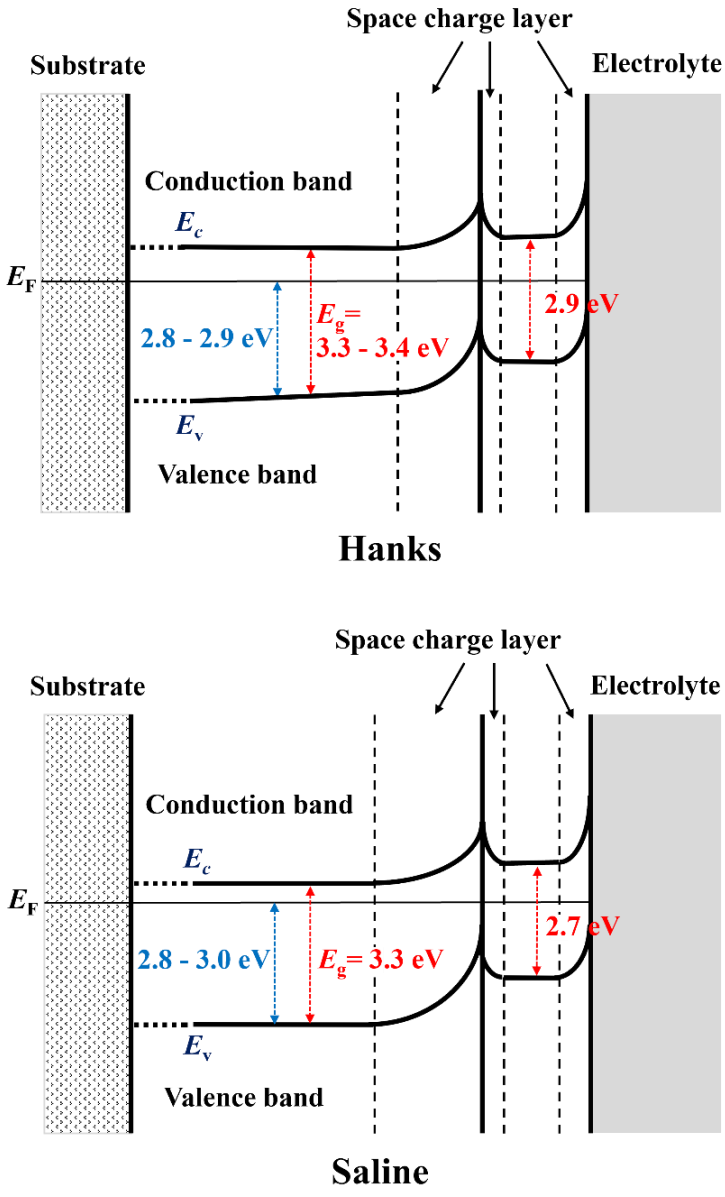

Figure 2.10 Electronic band structures of passive films formed on Ti in Hanks and saline.

2.5 Conclusion

Passive films formed on mainly consisted of a very thin TiO_2 layer containing small amounts of Ti_2O_3 and TiO, hydroxyl groups, and water. During polarization in Hanks, calcium and phosphate ions were incorporated or formed calcium phosphate but not in saline. Calcium phosphate and hydroxyl groups influenced the band structure. The passive films on Ti behaved as an n-type semiconductor consisting of two layers: an inner oxide layer with a large E_g, and an outer hydroxide layer with a small E_g. In Hanks, the value of E_g in the inner layer was 3.3 – 3.4 eV, whereas it was much lower in the outermost surface layer (2.9 eV). In saline, E_gs were 3.3 eV in the inner layer and 2.7 eV in the outermost layer. The E_g values of the outermost surfaces of the passive films formed on Ti were smaller than those of TiO_2 ceramics. Therefore, the Ti surface is more reactive with the surrounding environment than the TiO_2 ceramic surface. This is probably one of the reasons for the excellent biocompatibility of Ti among metals.

References

1. D. M. Brunette, P. Tengvall, M. Textor, and P. Thomsen, *Titanium in medicine. Berlin: Springer*, (2001).
2. P. Sanderson, W. Ryan, and P. Turner, *Injury*, **23**, 29 (1992).
3. T. Hanawa, *Front. Bioeng*, **7**, 170 (2019).
4. E. J. Kelly, *Mod. Aspect. Electrochem.*, **14**, 319 (1982).
5. K. Asami, S.-C. Chen, H. Habazaki, and K. Hashimoto, *Corros. Sci.*, **35**, 43 (1993).
6. T. Hanawa, K. Asami, and K. Asaoka, *J. Biomed. Mater. Res.*, **40**, 530 (1998).
7. A. Hiji, T. Hanawa, M. Shimabukuro, P. Chen, M. Ashida, and K. Ishikawa, *Surf. Interface Anal.*, **53**, 185 (2021).
8. J. W. Olver and J. W. Ross, *J. Am. Chem. Soc.*, **85**, 2565 (1963).
9. L.Wang, H. Yu, K. Wang, H. Xu, S. Wang, and D. Sun, *ACS Appl. Mater. Interfaces.*, **8**, 18608 (2016).
10. A. Hiji, T. Hanawa, T. Yokoi, P. Chen, M. Ashida, and M. Kawashita, *Langmuir.*, **37**, 3597 (2021).
11. U. Diebold, *Surf. Sci. Rep.*, **48**, 53 (2003).
12. F. Di Quarto, S. Piazza, and C. Sunseri, *Electrochim. Acta.*, **38**, 29 (1993).
13. J. Marsh and D. Gorse, *Electrochim. Acta.*, **43**, 659 (1998).
14. D. Kim and H. Kwon, *Corros. Sci. Technol.*, **2**, 212 (2003).
15. H. Tsuchiya and S. Fujimoto, *Sci. Technol. Adv. Mater.*, **5**, 195 (2004).
16. H. Tsuchiya, S. Fujimoto, and T. Shibata, *J. Electrochem. Soc.*, **151**, B39 (2004).
17. H. Tsuchiya, S. Fujimoto, and T. Shibata, *J. Electroceram.*, **16**, 49 (2006).
18. S. Fujimoto and H. Tsuchiya, *Corros. Sci.*, **49**, 195 (2007).
19. D. A. Shirley, *Phys. Rev. B.*, **5**, 4709 (1972).
20. K. Asami, K. Hashimoto, and S. Shimodaira, *Corros. Sci.*, **17**, 713 (1977).
21. K. Asami and K. Hashimoto, *Corros. Sci.*, **24**, 83 (1984).
22. T. Hanawa and M. Ota, *Biomaterials*, **12**, 767 (1991).
23. Y. Tanaka, M. Nakai, T. Akahori, M. Niinomi, Y. Tsutsumi, H. Doi, and T. Hanawa, *Corros. Sci.*, **50**, 2111 (2008).

24. J. Hammond, J. Holubka, J. Devries, and R. Dickie, *Corros. Sci.*, **21**, 239 (1981).
25. K. Asami and K. Hashimoto, *Corros. Sci.*, **17**, 559 (1977).
26. C. Wagner, *Practical Surface Analysis*, (1990).
27. T. Hanawa and M. Ota, *Appl. Surf. Sci.*, **55**, 269 (1992).
28. T. Hanawa, M. Kon, H. Ukai, K. Murakami, Y. Miyamoto, and K. Asaoka, *J. Biomed. Mater. Res.*, **34**, 273 (1997).
29. A. Orendorz, J. Wüsten, C. Ziegler, and H. Gnaser, *Appl. Surf. Sci.*, **252**, 85 (2005).
30. M. Fusi, E. Maccallini, T. Caruso, C. S. Casari, A. L. Bassi, C. E. Bottani, P. Rudolf, K. Prince, and R. G. Agostino, *Surf. Sci.*, **605**, 333 (2011).
31. R.L. Kurtz, R. Stock-Bauer, T. E. Msdey, E. Román, and J. De Segovia, *Surf. Sci.*, **218**, 178 (1989).
32. A. P. Singh, N. Kodan, and B. R. Mehta, *Appl. Surf. Sci.*, **372**, 63 (2016).
33. B. Lynch, F. Wiame, V. Maurice, and P. Marcus, *Appl. Surf. Sci.*, **575**, 151681 (2022).
34. T. Hanawa, S. Hiromoto, and K. Asami, *Appl. Surf. Sci.*, **183**, 68 (2001).
35. A. Nagai, Y. Tsutsumi, Y. Suzuki, K. Katayama, T. Hanawa, and K. Yamashita, *Appl. Surf. Sci.*, **258**, 5490 (2012).
36. T. Hanawa, S. Hiromoto, A. Yamamoto, D. Kuroda, and K. Asami, *Mater. Trans.*, **43**, 3088 (2002).
37. M. Tsukada, M. Wakamura, N. Yoshida, and T. Watanabe, *J. Mol. Catal. A.*, **338**, 18 (2011).
38. L. Calderin, M. Stott, and A. Rubio, *Phys. Rev. B.*, **67**, 134106 (2003).
39. L. Liang, P. Rulis, and W. Ching, *Acta Biomater.*, **6**, 3763 (2010).
40. Y. Tsutsumi, D. Nishimura, H. Doi, N. Nomura, and T. Hanawa, *Mater. Sci. Eng. C.*, **29**, 1702 (2009).
41. B.-Y. Kim, C.-J. Park, and H.-S. Kwon, *J. Electroanal. Chem.*, **576**, 269 (2005).
42. R. French, S. Glass, F. Ohuchi, Y.-N. Xu, and W. Ching, *Phys. Rev. B.*, **49**, 5133 (1994).

Chapter 3

Electronic structures of passive film formed on Ti and Cr in a phosphate buffer solution of pH 7

3.1 Introduction

Ti-based and Cr-containing alloys are widely used in various fields that require high corrosion resistance [1-8]. These materials commonly form passive films on their surfaces, providing excellent corrosion resistance. The surfaces of Ti-based alloys, such as Ti-6Al-4V and Ti-Ni, are mainly covered with a Ti dioxide [3-5]. Meanwhile, passive films on Cr-containing alloys such as, Fe-Cr, Ni-Cr, and Co-Cr-Mo alloys consist of oxides and hydroxides, including large amounts of Cr [6-11].

Passive films on Ti [12] and Cr [13] are known to exhibit semiconductive behavior. Ti oxides are widely used as functional materials in light-energy conversion devices, such as solar cells, and their semiconductive behavior has been investigated in various studies, including the pioneering work of Bard [14, 15]. Passive films on Ti have been reported to generate a positive photocurrent, which is a characteristic of n-type semiconductors, regardless of the film-formation environment [16, 17]. Mott-Schottky plots measured for the passive films showed a clear positive slope, also indicating n-type semiconductive behavior [18, 19]. Kwon *et al.* compared the photoelectrochemical behavior of the passive film formed on Ti in a pH8.5 buffer solution with that of the thermally grown oxide layer on Ti at 673 K. They reported that the optical band gap energy of 3.36 eV was obtained for the passive film, which was relatively larger than that for the thermal oxide layer (3.1 eV). The larger band gap energy was attributed to the less crystallinity or more disordered structure of the passive film compared to that of the thermal oxide layer [20]. Semiconductive behavior of passive and anodic films has been studied not only for Ti but also for Ti alloys. Santamaria *et al.*

measured and analyzed photocurrent spectra for anodic films formed on Ti-Zr alloys with different Zr content ranging from 10 at. % to 100 at. % (pure Zr) and found that the optical band gap energy increased with increasing Zr content. They discussed that the correlation between the band gap of the oxides and the electronegativity difference of their constituents [21]. Piazza also examined anodic films formed on cast Ti-Mo alloys with different Mo contents (6 – 20 wt.%). They reported for thick anodic films grown at higher potentials on Ti-Mo alloys with higher Mo contents that the direction of photocurrent changed depending on the applied potential where the photocurrent measurements were carried out, that is, positive photocurrents were generated at the higher applied potential whereas negative ones were found at the lower potential [22].

The semiconductor properties of passive films on Cr-containing alloys have also been extensively studied. Tsuchiya *et al*. revealed using the photoelectrochemical response that the passive films on stainless steel consisted of a p-n junction or an n-n junction depending on the pH of the solution [13, 23]. Kim *et al*. reported that the photocurrent generated on passive films of Ni-Cr alloys depended on the Cr content inside the films [11]. In electrochemical impedance spectroscopy, which is commonly used to determine the type of semiconductor, the Mott–Schottky plots did not necessarily show a straight line due to the duplex structure of passive films on the Cr-containing alloy [23, 24]. Santamaria *et al.* considered passive films formed on type 304L, 316L and duplex stainless steels in various solutions with different pHs. They described that passive films grown on 316L and duplex stainless steels in a neutral aqueous solution were doped with Mo during the growth of passive films, resulting in the changes in their electronic properties such as band gap energy and flat band potential from those of passive films on 304L stainless steel [25]. Furthermore, they examined passive films on the stainless steels and pure Cr in acidic and alkaline solutions and described that the passive films on the stainless steels behaved as n-type semiconductors while passive films on pure Cr behaved as p-type semiconductors. In addition, band gap energies of passive films on the 304L

and 316L stainless steels and pure Cr were reported to vary depending on the pH of the solutions whereas band gap energy of those on the duplex stainless steel was independent of the pH [26]. As described above, the semiconductive properties of passive films on Fe-Cr and Ni-Cr alloys vary depending not only on the alloy composition, but also on environmental factors such as pH. Therefore, largely different conclusions have been drawn depending on the measurements used for the analysis. Therefore, the semiconductive properties of passive films are not consistently understood yet. It is well known that Cr is enriched in passive films on highly corrosion-resistant Cr-containing alloys, such as Fe-Cr and Ni-Cr alloys (i.e., these alloys exhibit the excellent corrosion resistance when their surfaces are covered with a thin layer mainly consisting of Cr oxide). The properties of the passive films on Cr should be revealed to understand the role of Cr oxide with respect to the high corrosion resistance of Cr-containing alloys.

In this work, the author examined the semiconductive behavior of passive films on Cr formed in a phosphate buffer solution (PBS) using photoelectrochemical response and electrochemical impedance spectroscopy. In addition, valence-band X-ray photoelectron spectroscopy (XPS) was also used to obtain further details on the electronic structures of the passive films on Cr. The electronic structures of the passive films on Cr were compared with those of the passive films on Ti, the structures of which are relatively clear.

3.2 Experimental

Materials examined were CP Ti (purity: 99.9 %) and commercially available pure Cr (purity: 99.95 %) sheets with a thickness of 2 mm were examined. Several coupons of both metals were cut from each sheet to the dimensions of 10×10 mm^2. For electrical conduction, a wire was welded to the coupons and then, each coupon was embedded in epoxy resin to prepare the specimens. The surfaces of the specimens were mechanically polished with SiC abrasive paper up to #2000, followed by mirror-finishing with a submicron diamond paste.

After polishing, the specimens were sequentially cleaned with acetone, ethanol, and distilled water. The surface was covered with polytetrafluoroethylene (PTFE) adhesive tape, leaving an exposed area of 28.3 mm^2 to the solution. A conventional three-electrode configuration cell equipped with a Ag/AgCl reference electrode and a platinum counter was used for all electrochemical measurements. A PBS of pH 7 was deaerated with N_2 gas for at least 2 h in an electrochemical cell prior to the electrochemical measurements.

For the photoelectrochemical response, the Ti and Cr specimens were passivated for 2 and 24 h at the desired film formation potentials (E_f), respectively, before commencing the measurements. Monochromatic light obtained using a 150-W xenon arc lamp and a grating monochromator was irradiated onto the passivated specimen surfaces in the electrochemical cell through a quartz window. The current change during light irradiation of 20 s was recorded as the photocurrent, and the measurement was performed at E_f by changing the wavelength of the incident light from 250 nm to 500 nm. The applied potential was then changed stepwise at an interval of 0.1 V in the less noble (less positive) direction and the measurement of the photocurrent spectrum was repeated at each measuring potential (E_m). The author carefully shielded the electrochemical cell to avoid noise and also used a low-pass filter with a cut-off frequency of 4 Hz to measure extremely small photocurrents generated from passive films.

In the electrochemical impedance measurement, the capacitance of the passive film formed on Cr and Ti was obtained from the impedance measured at 1 Hz, where the Bode plot represents the capacitive region. The measurement was performed at each E_m, which was the same as for the photoelectrochemical response.

XPS was used to characterize the chemical structures of the passive films on Ti and Cr. The surfaces of the Ti and Cr specimens were passivated under the same conditions as those used for the photoelectrochemical response, rinsed with ultrapure water, and dried in air. After drying, the specimens were placed in the chamber of an XPS apparatus (JPS-9010MC;

JEOL, Japan). All XPS spectra were obtained using the Mg Kα line (1253.6 eV). After the measurements the electron energy of the C 1s peak (285.0 eV) derived from the surface contamination hydrocarbon was used to calibrate the binding energy. The background of the obtained XPS spectra was subtracted, as required, using the Shirley's method [27]. The structure of the passive film was qualitatively evaluated based on the deconvoluted photoelectron spectra of Ti 2p 3/2, Cr 2p 3/2, O 1s and C 1s.

3.3 Results

Figure 3.1 shows polarization curves of Cr and Ti in the PBS of pH 7. Cr shows a passive region from −0.6 $V_{Ag/AgCl}$ to 0.6 $V_{Ag/AgCl}$ in the solution whereas Ti exhibits a passive region in the wide potential range from −0.5 $V_{Ag/AgCl}$. In the present work, the author determined several potentials for the film formation potential to examine the semiconductive behavior of passive films on Cr and Ti at the potentials. Figure 3.2 (a) presents the photocurrent spectra of the passive films formed on Cr at 0.4 $V_{Ag/AgCl}$ in the PBS of pH 7. Photocurrent measurements were performed at various measuring potentials (E_m). The spectra in the red solid square of Fig. 3.2 (a) are enlarged and re-plotted in Fig. 3.2 (b). From Figs. 3.2 (a) and (b), it is obvious that the photocurrent depends not only on the wavelength of the incident light but also on E_m. In addition, positive and negative photocurrents are found depending on the wavelength in one single photocurrent spectrum, which is obtained at the E_m of 0.3 $V_{Ag/AgCl}$ as apparent from Fig. 3.2 (b). Note that the photocurrent spectra must be normalized for further analysis because the light intensity is not constant for each wavelength. Assuming that photoexcitation occurs as an indirect transition, the photocurrent spectra are expressed as photoelectrochemical action spectra using Eq. (2.1), as in Chapter 2.

Figure 3.2 (c) shows the photoelectrochemical action spectra obtained from the passive films on Cr. All spectra deviate from a single linear trend, and instead exhibit two regions with different slopes. This indicates that the photocurrents reflect a duplex structure of

passive films (i.e., an uppermost hydroxide layer and an underlying oxide layer), as reported previously by Fujimoto *et al.* [13, 28], that is, the photocurrents generated individually from the hydroxide layer as well as the oxide layer. Therefore, the two bandgap energies, E_gs, can be estimated from Figs. 3.2 (c) and (d). This approach is similar to the duplex-structure analysis in previous studies on passive films of Fe-Cr alloys, Ni-Cr alloys and pure Cr [11, 13, 23, 28, 29]. The E_gs of the passive film on Cr were estimated at approximately 2.5 and 3.6 eV. Referring to E_g reported for Cr oxide and hydroxide,[13, 25] it is found that E_gs of 2.5 and 3.6 eV obtained from the photoelectrochemical response were attributed to the outer $Cr(OH)_3$ and inner Cr_2O_3 layers, respectively.

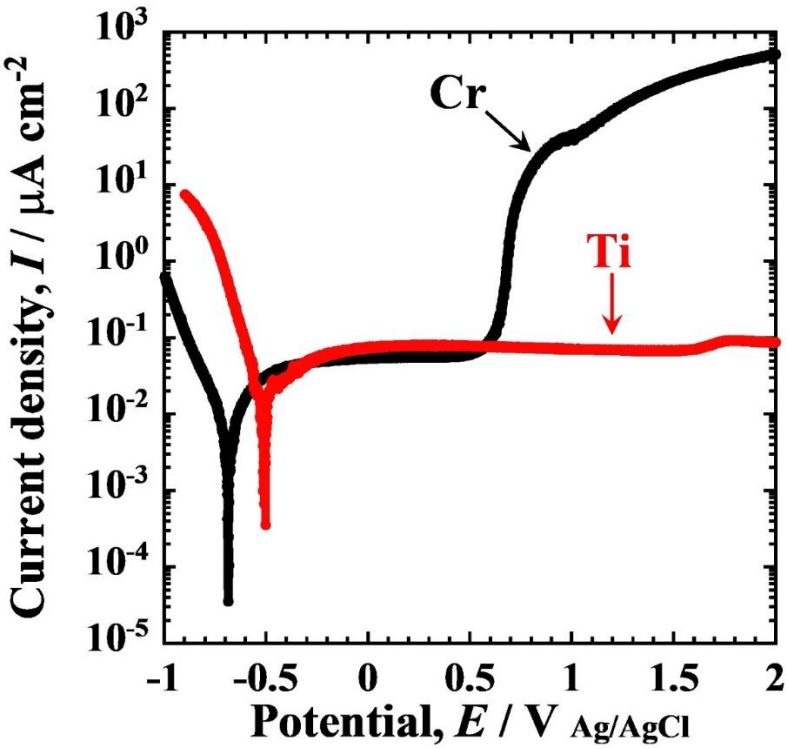

Figure 3.1 Potentiodynamic polarization curves of Cr and Ti in a phosphate buffer solution with a sweep rate of 1 mV/s.

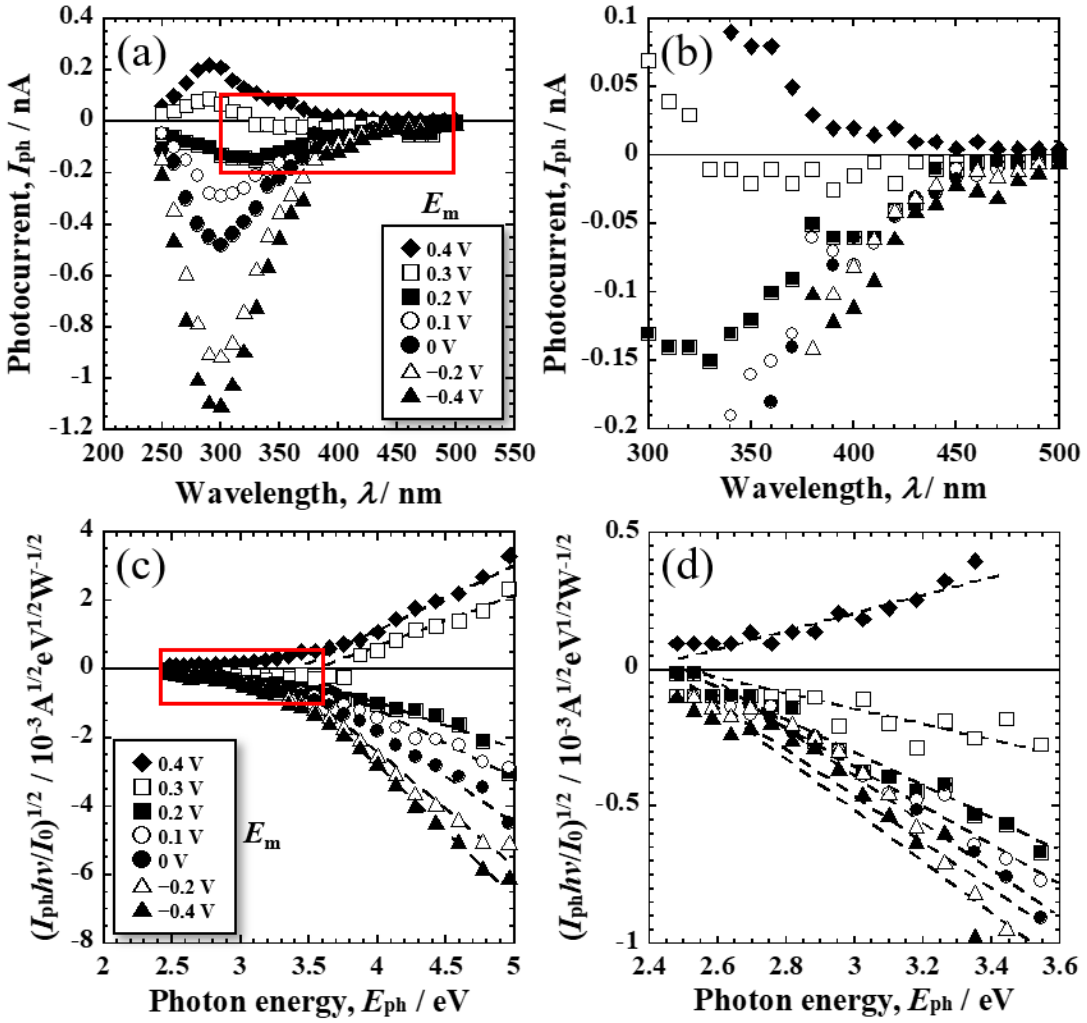

Figure 3.2 (a) Example of photocurrent spectrum for the passive film of Cr formed at 0.4 V and (c) the photoelectrochemical action spectra obtained from the photocurrent spectra shown in (a). Figures (b) and (d) are enlarged figures of the red solid square regions in (a) and (c), respectively.

The results obtained for the passive film formed on Ti at 0 $V_{Ag/AgCl}$ in the PBS of pH 7 are displayed in Fig. 3.3 in the same manner as Cr. Similar to Cr, the photoelectrochemical action spectra of the passive film also exhibited two distinct regions with different slopes. As shown in Figs. 3.3 (c) and (d), the E_gs of the passive film on Ti were estimated to be approximately 2.4 – 2.5 eV and 3.2 eV. The E_g of 3.2 eV coincides with the value reported for anatase [21]. The other E_g of 2.4 – 2.5 eV, which is narrower than that of Ti dioxide, may be attributed to Ti hydroxide. Nogueira *et al*. reported that the E_g of $Ti(OH)_4$ is 0.7 eV narrower than that of TiO_2 [32]. Therefore, the smaller E_g obtained for the passive film is considered to be related to the adsorption of hydroxyl groups or the formation of Ti hydroxides such as $Ti(OH)_4$. This indicates that the passive film on Ti also consists of inner oxide and outer hydroxide layers.

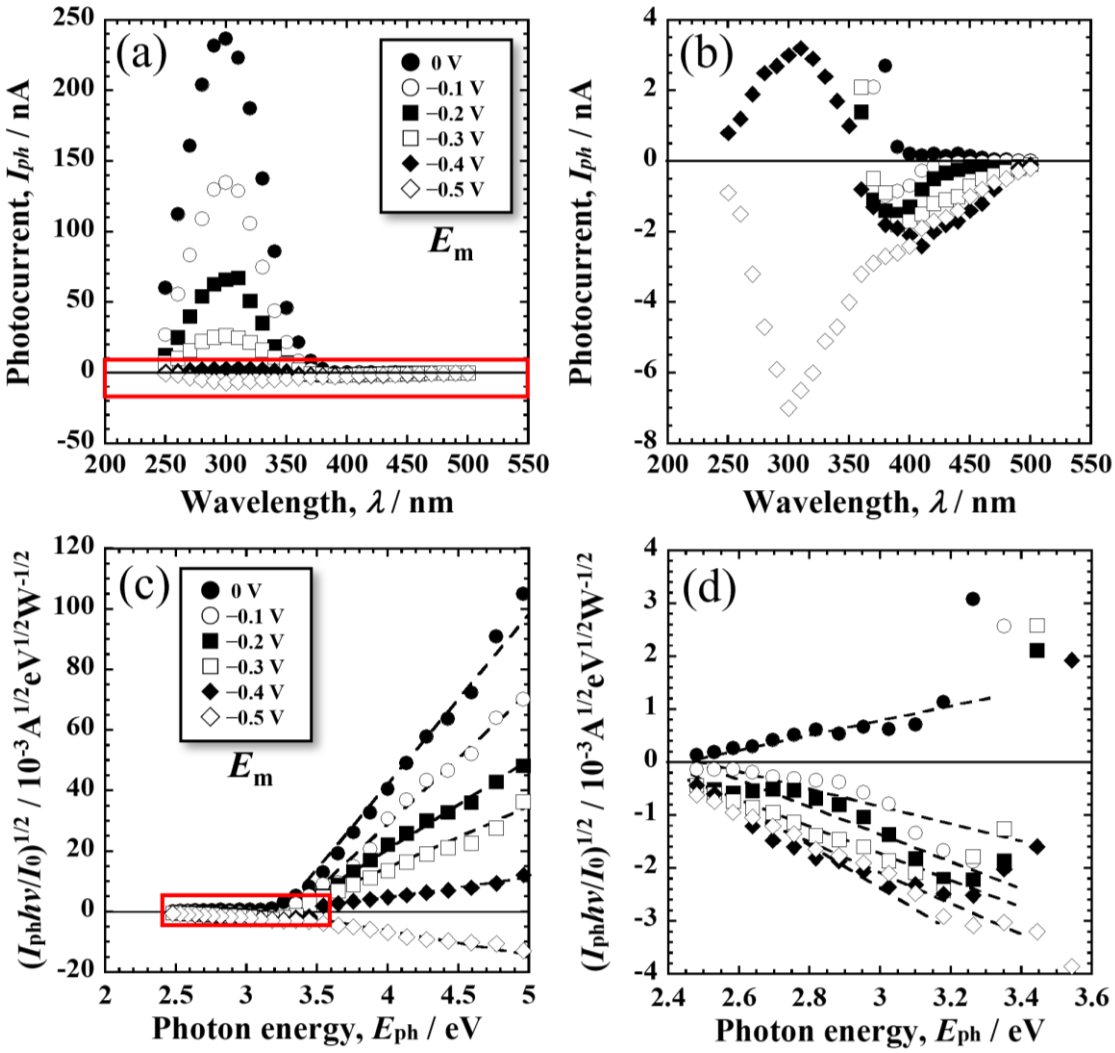

Figure 3.3 (a) Example of photocurrent spectrum for the passive film of Ti formed at 0 V and (c) the photoelectrochemical action spectra obtained from the photocurrent spectra shown in (a). Figures (b) and (d) are enlarged figures of the red solid square regions in (a) and (c), respectively.

Figure 3.4 shows the variation in the slope of the photoelectrochemical action spectra, *S*, of the passive films on Cr and Ti formed at various E_fs in the PBS. From the results obtained for Cr shown in Fig. 3.4 (a), it is found that the *S* values obtained for the inner Cr_2O_3 layers are negative, and the absolute values of *S* increase with decreasing E_m. This is typical p-type semiconductive behavior, indicating that the inner oxide layer behaves as a p-type semiconductor with an E_g of 3.6 eV. On the other hand, the *S* values for the outer $Cr(OH)_3$ layers are relatively small compared to those of the oxide layer. However, it is clear that most of the *S* values for the hydroxide layers (E_g = 2.5 eV) are negative and the absolute values increase as E_m decreases. This indicates p-type semiconductive behavior, which will be discussed later.

For the passive film formed on Ti, the photocurrent response of the component with the E_g of 3.2 eV, which is attributed to the inner oxide layer, exhibits a positive *S* value at most potentials, which increases with increasing E_m, as shown in Fig. 3.4 (b). This is a typical n-type semiconductive behavior. In contrast, the photocurrents generated on the hydroxide layer (E_g = 2.5 eV) are significantly smaller than those derived from the oxide layer. The *S* value for the hydroxide layer is negative at lower E_ms, but increases with increasing E_m and then changes to positive at –0.05 $V_{Ag/AgCl}$. It is difficult to determine the type of semiconductor for the hydroxide layer based only on the potential dependence of *S* value.

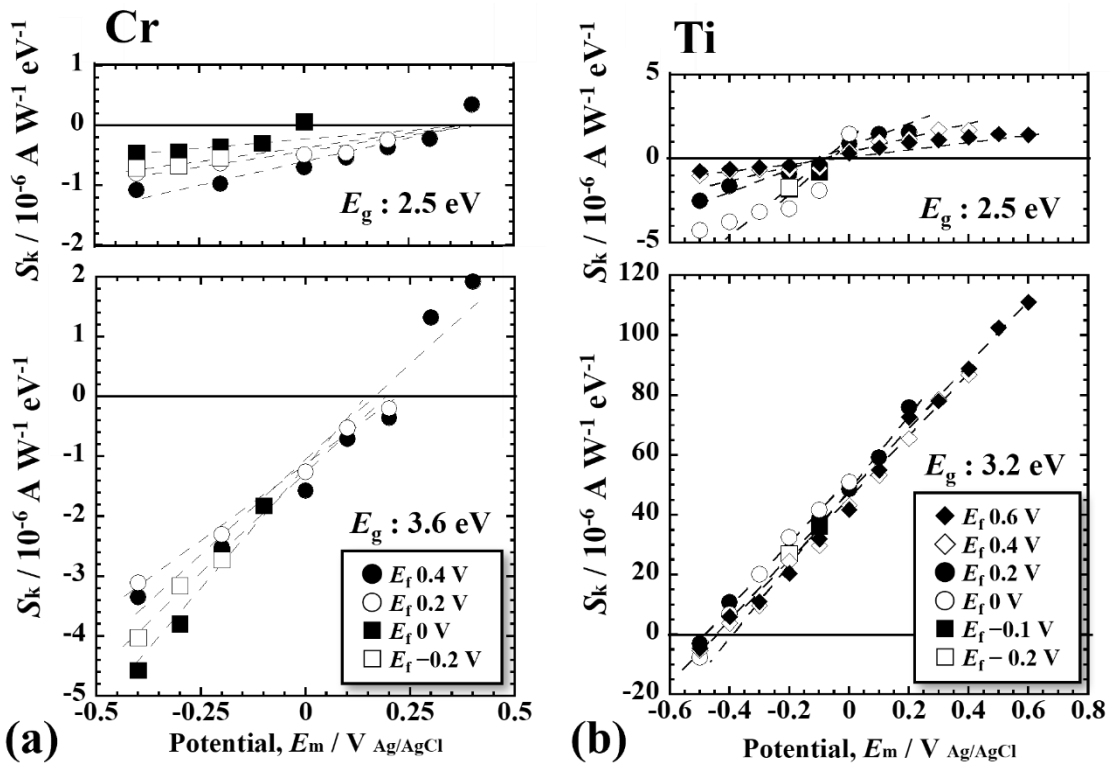

Figure 3.4 Variations in the slope of the action spectrum, S_k, of the passive film for (a) Cr and (b) Ti formed at different potentials in phosphate buffer solutions.

Figure 3.5 (a) shows the Mott-Schottky plots obtained for the passivated Cr surfaces at various E_fs. As shown in Fig. 3.5 (a), two straight lines with negative and positive slopes were obtained at potentials higher than about 0 $V_{Ag/AgCl}$ and at potentials lower than 0 $V_{Ag/AgCl}$, respectively. This implies that two or more space-charge layers are present in the passive films on Cr, assuming that the capacitance of the Helmholtz layer is greater than those of space-charge layers in the passive films. For Cr, Mott–Schottky plots exhibit behaviors different from those in the photoelectrochemical response, which is discussed later. As shown in Fig. 3.5 (b), by contrast, the straight lines with positive slopes in the Mott-Schottky plots of the passivated Ti indicate that the passive films on Ti formed in the PBS behave as n-type semiconductors.

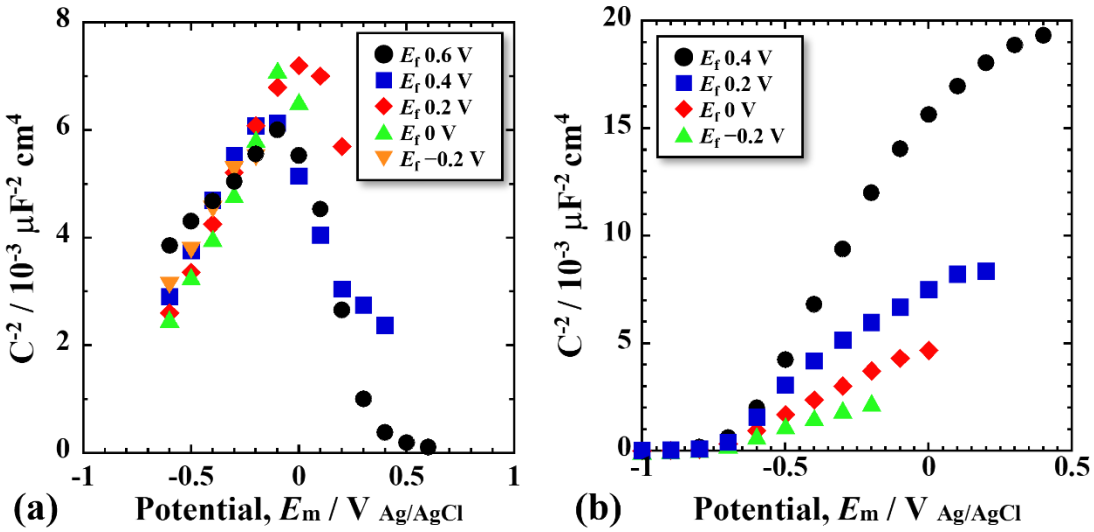

Figure 3.5 Mott-Schottky plots for passive films formed on (a) Cr and (b) Ti at various potentials in phosphate buffer solution.

Figure 3.6 shows the XPS spectra obtained for the passive film formed on Cr at 0.4 $V_{Ag/AgCl}$ in the PBS. The XPS spectra were deconvoluted into some chemical states, according to the procedure reported in previous studies [33, 34]. In the Cr 2p spectrum, the peaks from hydroxide and oxide of Cr^{3+} are identified in addition to the peak derived from metallic Cr, while the O 1s spectrum consists of peaks from OH^-, O^{2-}, and H_2O. Therefore, the passive film formed on Cr is concluded to be composed of $Cr(OH)_3$, Cr_2O_3, and bonding water. The XPS spectra obtained for the passive film formed on Ti at 0 $V_{Ag/AgCl}$ in the PBS are presented in Fig. 3.7. The Ti 2p spectrum consists of four doublets corresponding to the metallic state of Ti^0 and the oxidized states of Ti^{2+}, Ti^{3+} and Ti^{4+} whereas the O 1s spectrum consists of three peaks derived from OH^-, O^{2-} and H_2O, similar to Cr. The passive film formed on Ti is composed mainly of TiO_2 and a covering layer containing some hydroxyl groups and water, because the area ratio of the Ti^{4+} peak is relatively large compared to those of the other oxidized states. The structures of the passive films on Cr and Ti agree well with those discussed for the photoelectrochemical response.

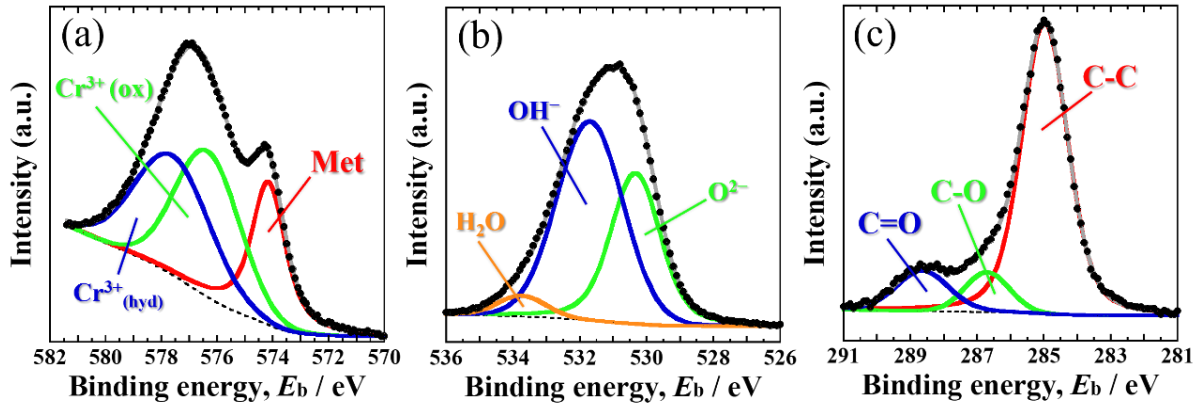

Figure 3.6 (a) Cr 2p, (b) O 1s, and (c) C 1s electron energy region spectra obtained from Cr after polarization at 0.4 $V_{Ag/AgCl}$ in phosphate buffer solution for 24 h.

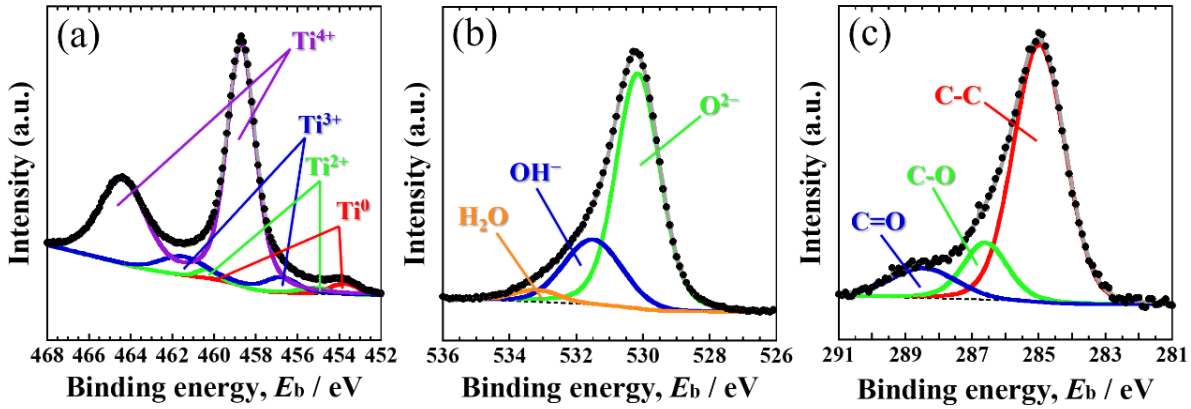

Figure 3.7 (a) Ti 2p, (b) O 1s, and (c) C 1s electron energy region spectra obtained from Ti after polarization at 0 $V_{Ag/AgCl}$ in phosphate buffer solution for 2 h.

Understanding the valence-band position in a passive film provides valuable insights into its electronic band structure. Therefore, the XPS spectra near the valence-band region, that is, the valence-band XPS spectra for Cr and Ti, were also acquired, as shown in Figs. 3.8 (a) and (b), respectively. In the figures, 0 eV of the binding energy was calibrated using the Fermi energy, $E_{F,}$ of gold (Au). These valence-band XPS spectra might be composed of the spectra attributed to the passive film and that of substrate metal. The author recently evaluated the valence-band positions of passive films on Ti in Hanks' and saline solutions [35]. As in the present study, a similar valence-band spectrum was obtained for passivated Ti in the PBS of pH 7, thus the author similarly analyzed the spectrum displayed in Fig. 3.8 (b). A large peak is observed in the binding energy range from 3 eV to 10 eV, whereas the other broad but low-intensity peak arises from 0 eV and then overlaps with the large peak in the binding energy region larger than 3 eV. This large peak may have originated from the passive film on Ti. As shown in Fig. 3.8 (b), the energy difference between the Fermi level of substrate metal and the highest energy of the valence-band in the passive film, E_v, was determined by linearly extrapolating the Fermi-level-side slope of the spectrum to the baseline [36], which was calculated to be 2.7 eV. As the peak of metallic Ti corresponding to the Ti 3d orbital is reported to be at 0 – 2 eV [37], the broad but small peak at 0 eV can be attributed to the Fermi energy of the Ti substrate.

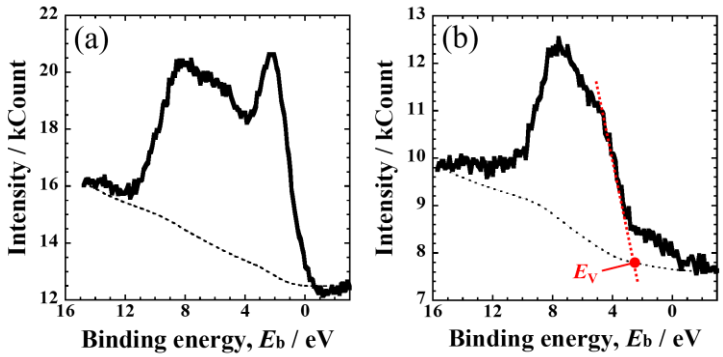

Figure 3.8 XPS spectra of the valence-band region: (a) Cr after polarization at 0.4 $V_{Ag/AgCl}$ in PBS for 24 h and (b) Ti after polarization at 0 $V_{Ag/AgCl}$ in PBS for 2 h.

As shown in Fig. 3.8 (a), on the other hand, two large peaks are observed around 0 – 12 eV in the valence-band XPS spectrum of the passivated Cr at 0.4 $V_{Ag/AgCl}$ in the PBS. According to literature, the photo-electron peaks of metallic Cr corresponding to Cr 3d orbital and the peak of Cr oxide corresponding to the O 2p orbital are located at 0 – 3 eV and 4 – 8 eV, respectively [38]. Therefore, the peaks in the 0 – 12 eV region can be interpreted to be derived from the passive film and Cr substrate. Because the peak of metallic Cr is considerably high, the spectra of the Cr metal and the passive film on Cr cannot be separated by simple linear extrapolation. Therefore, in the present study, the passive film was successively removed by Ar ion sputtering, and the valence-band XPS spectra were then acquired. Core-level photoelectron spectra were also acquired to confirm how the passive film was sputtered. Figure 3.9 (a) and (b) show the Cr 2p and O 1s spectra of the passive film formed on Cr in the PBS of pH 7 at 0.4 $V_{Ag/AgCl}$ before Ar ion sputtering. After sputtering for 200 s, the Cr 2p spectrum in Fig. 3.9 (c) still consists of three peaks derived from Cr^{3+} oxide, Cr^{3+} hydroxide, and metallic Cr, although the intensities of oxide and hydroxide drastically decrease. After sputtering for 7200 s, the peak of Cr^{3+} hydroxide completely disappears, but the peak of Cr^{3+} oxide remains. In the O1s spectrum in Fig. 3.9 (d), the peak derived from H_2O completely disappears, and the peak from hydroxide remains to a slight extent after sputtering for 200 s. Even after sputtering for 7200 s, the oxygen-related peaks, that is, Cr^{3+}(ox) and O^{2-}, are still evident, as shown in Figs. 3.9 (e) and (f). This is due to the re-oxidation of Cr surface after the sputtering because the sputtering was conducted in the pre-chamber of the XPS apparatus where the vacuum level is a bit lower compared to the main chamber where XPS measurements are performed. Figure 3.10 shows the sputtering-induced changes in the valence-band spectrum of the passivated Cr in the PBS of pH 7. Note that deconvoluted spectra are also displayed in the figures. Through Ar-ion sputtering, distinct changes are observed in the binding energy range of 3 – 12 eV. Considering the changes in the core-level spectra induced by sputtering, shown in Fig. 3.9, a

decrease in the peak intensity between 6 and 10 eV in the spectrum after 200 s of sputtering can be attributed to the removal of the hydroxide species. Further sputtering for 7200 s reduces the peak intensity in the binding energy range of approximately 5 eV, owing to the partial removal of the oxide species. These results suggest that the peaks observed within the binding energy range of 3 – 12 eV in the spectrum originate from the hydroxide and oxide of Cr. On the other hand, the peak observed around the binding energy of 2 eV can be derived from the Cr substrate, and the binding energy where the peak appears remains unchanged throughout the sputtering process. The E_vs for the oxide and hydroxide on Cr can be obtained by extrapolating line of the deconvolved peaks in the same manner as for Ti, as shown in Fig. 3.8 (b). The Fermi level of the Cr substrate was assumed to be locate at the energy at which the intensity of the metallic Cr peak increased. As discussed above, the area ratio of the peaks related to the oxide and hydroxide of Cr decreases after sputtering for 200 s. Further sputtering for 7200 s completely removed the hydroxide, and thereby, E_v for the oxide was easily estimated as 0.3 eV. This is in accordance with those estimated from the original spectrum and the spectrum sputtered for 200 s based on the deconvoluted spectra. The E_v for the hydroxide was also estimated as 0.4 eV from the spectra.

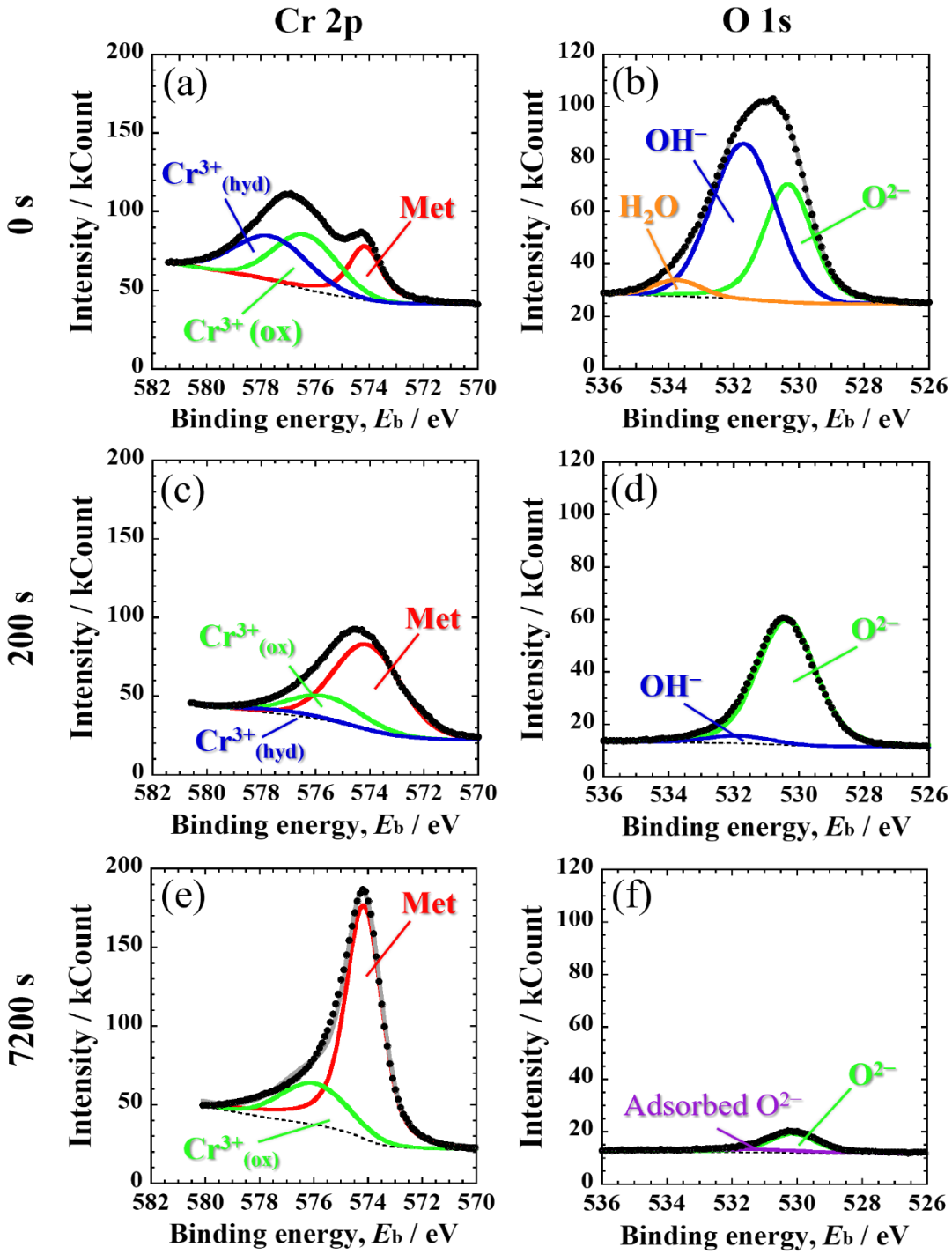

Figure 3.9 (a) and (b) represent the spectrum of Cr 2p and O 1s without sputtering. (c) Cr 2p and (d) O 1s electron energy region spectra obtained after 200 s of Ar sputtering, and (e) Cr 2p and (f) O 1s electron energy region spectra were obtained after 7200 s of Ar sputtering.

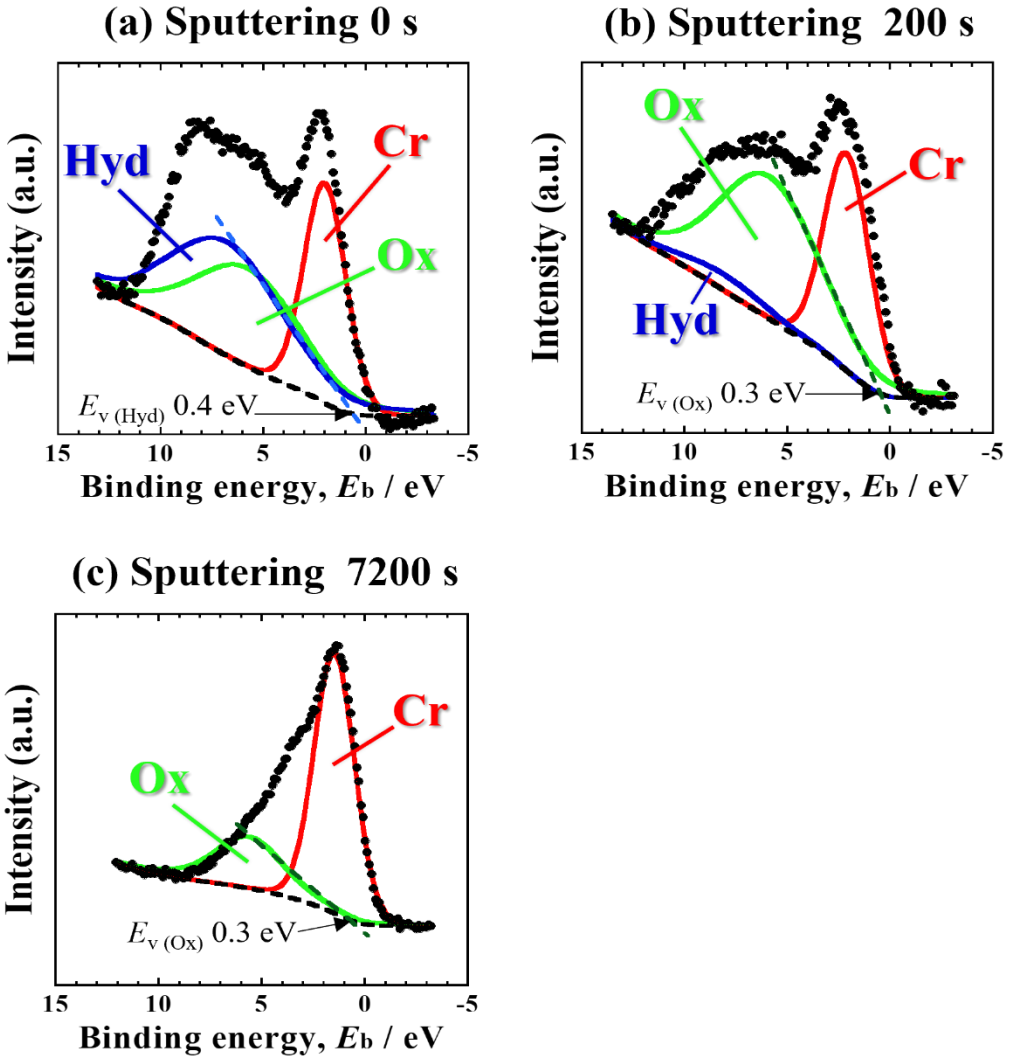

Figure 3.10 Deconvoluted valence-band spectra of passivated Cr at 0.4 $V_{Ag/AgCl}$ for 24 h.

3.4 Discussion

3.4.1 Electronic structure of passive films on Ti in the PBS of pH 7

In the case of Ti, typical n-type semiconductive behavior is observed in the Mott–Schottky plot, as well as in the potential dependence of the *S* value obtained from the photoelectrochemical action spectra for the oxide layer with a large E_g of 3.2 eV. In addition, the resutls obtained from valence-band XPS of the passivated Ti indicate that the passive film can be an n-type semiconductor as the highest energy of the valence-band of the passive film is estimated to be located 2.5 eV lower than the Fermi energy of the metallic substrate.

In the present work, the photoelectrochemical response was carried out for the passive films formed at various, E_fs, ranging from −0.2 $V_{Ag/AgCl}$ to 0.6 $V_{Ag/AgCl}$. As presented in Fig. 3.4 (b), the photoelectrochemical response for the component with larger E_g of 3.2 eV, that is, the oxide layer in the passive films, is independent of E_fs. This implies that except for the thickness of the passive films, which is well known to linearly increase with the E_f [39], the other properties of the passive films as well as the width of the space charge layer in the passive films are similar independent of the E_fs. The author of the present work deduces that in the potential range in which the photoelectrochemical response of the passive films on Ti is measured, the thickness of the passive films increases with increasing the E_fs; however, the width of the space-charge layer, which is one of the dominant factors for the generation of photocurrent, is independent of E_fs. Therefore, the *S* value for the inner oxide layer with the E_g of 3.2 eV is independent of the film-formation potential as well.

In contrast, for the hydroxide layer with the E_g of 2.5 eV, positive and negative photocurrents were generated in the photocurrent spectrum; therefore, it is difficult to determine whether the hydroxide layer is an n-type or a p-type semiconductor. Furthermore, the amplitude of the photocurrent depends on the film-formation potential. The author previously examined passive films formed on Fe-Cr alloys in an acidic solution and found that the photocurrents generated in the outer hydroxide layer of the passive films changed direction

from negative to positive with increasing the E_m [13], similar to those observed for the hydroxide layers in the passive films on Ti. In the duplex structure of the passive films, the outer hydroxide layer could build space-charge layers at both interfaces: the outer hydroxide layer/inner oxide layer and the outer hydroxide layer/aqueous solution. The author suggested that the outer hydroxide layer in the passive films on Ti is an n-type semiconductor, and at lower E_ms, the space-charge layer at the interface between the outer hydroxide layer and inner oxide layer is dominant, whereas at higher E_ms, the space-charge layer at the interface between the outer hydroxide layer and solution is dominant (see Fig. 3.11 (b)), resulting in negative photocurrent and positive photocurrents, respectively. As discussed above, the present results for the photoelectrochemical response can be explained, even if the outer hydroxide layer is an n-type semiconductor. Furthermore the Mott–Shockky plots of the passivated Ti reflect the n-type semiconductive behavior of the passive films. The valence-band XPS results also indicate that the outer hydroxide layer can be considered as an n-type semiconductor. Therefore, the author determined that the outer hydroxide layer in the passive films formed on Ti in the PBS of pH 7 behaves as an n-type semiconductor, similar to the passive films formed on Fe-Cr alloys in an acidic solution [13]. Based on the above discussion, it can be concluded that the electronic structure of the passive films formed on Ti in the PBS of pH 7 consists of an n-type inner oxide layer with an E_g of 3.2 eV and an n-type outer hydroxide layer with an E_g of 2.5 eV.

3.4.2 Electronic structure of passive films on Cr in the PBS of pH 7

In the case of Cr, the inner oxide layer exhibits typical p-type semiconductive behavior, whereas the outer hydroxide layer is assumed to be a p-type semiconductor because negative photocurrents are observed for most E_ms. As explained above, the valence-band XPS indicates that the highest energy of the valence-band of the inner oxide layer and outer hydroxide layer are located 0.3 and 0.4 eV lower than the Fermi level of the substrate Cr, respectively, whereas

the E_gs of the layers are estimated as 3.6 and 2.5 eV, respectively, in the photoelectrochemical response, demonstrating that both the layers are p-type semiconductors. In contrast, the Mott–Schottky plots of the passivated Cr exhibit negative slopes at noble potentials and positive slopes at less noble potentials than 0 $V_{Ag/AgCl}$. The differential capacitance of the hydroxide layer is found to be smaller than that of the oxide layer because the outer hydroxide layer is not as dense as the inner oxide layer. Therefore, the outer hydroxide layer is assumed to be responsible for the series capacitance of the passive film, where space-charge layers are formed at several interfaces in the film. Figure 3.11 (a) illustrates an electronic band structure model of the passive films formed on Cr based on the results obtained in the present study and the aforementioned assumptions. In the electronic band structure, negative photocurrents are generated in the inner oxide layer at most E_ms, whereas the direction of the photocurrent in the outer hydroxide layer varies depending on the correlation of the space-charge layers built at the interface with the inner oxide layer, as well as at the interface with the solution, as discussed in the previous section. This can explain why a positive photocurrent is generated at a higher potential of 0.4 $V_{Ag/AgCl}$. With decreasing the measuring potential, the width of the space-charge layer at the interface between the outer hydroxide layer and solution increases, resulting in negative slopes in the Mott–Schottky plots, as presented in Fig. 3.5 (a). However, the Fermi level at the interface between the outer hydroxide layer and solution approaches the conduction band of the layer with a further decrease in the potential. In such a situation, the depletion layer turns into an inversion layer, where minority charge carriers (i.e., electrons in this case) accumulate. The differential capacitance of the inversion layer in the p-type hydroxide layer is considered to increase with decreasing potential, resulting in a positive slope in the Mott–Schottky plots. Thus, it can concluded that the electronic structure of the passive films formed on Cr in the PBS of pH7 consists of a p-type inner oxide layer with an E_g of 3.6 eV and a p-type outer hydroxide layer with an E_g of 2.5 eV.

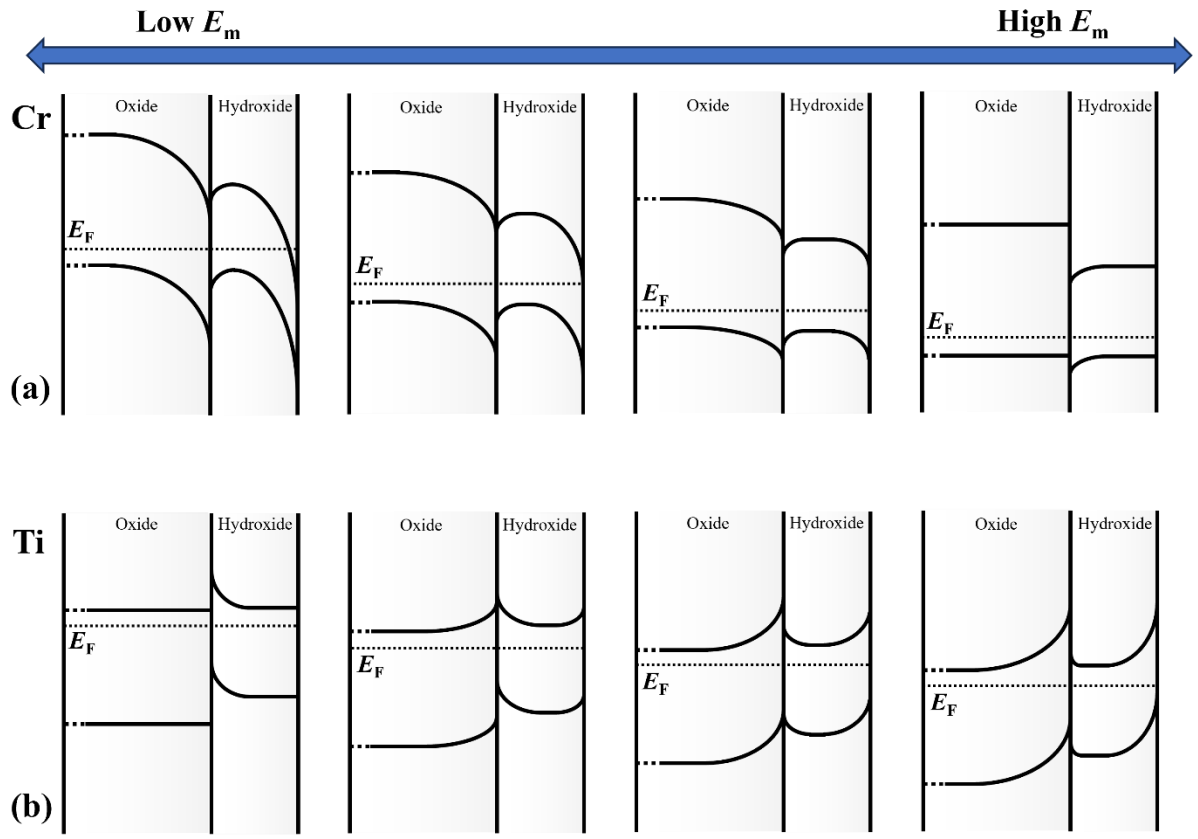

Figure 3.11 The schematic diagrams of electronic band structure according to the potential for passive film on (a) Cr and (b) Ti.

3.4.3 Electronic structure of passivated Ti and Cr

Through the present work, the author evaluated several properties that characterize the semiconductive nature of passive films formed on Cr and Ti using photoelectrochemical response and valence-band XPS. Based on these results, the electronic structures of the passivated Cr and the passivated Ti are schematically illustrated in Figs. 3.12 (a) and (b), respectively. In the right part of each figure, the (partial) density of states for the passive films is presented, whereas in the left part, the counterpart for the underlying metal substrate is displayed. Note that although passive films possess a layered structure consisting of an inner oxide layer and an outer hydroxide layer as mentioned above, the oxide and hydroxide layers cannot be distinguished in the figures for simplicity. As mentioned above, the band structure of the passive film can be discussed in more detail by using the valence-band XPS with the photoelectrochemical response, which helps in further understanding of the passive film.

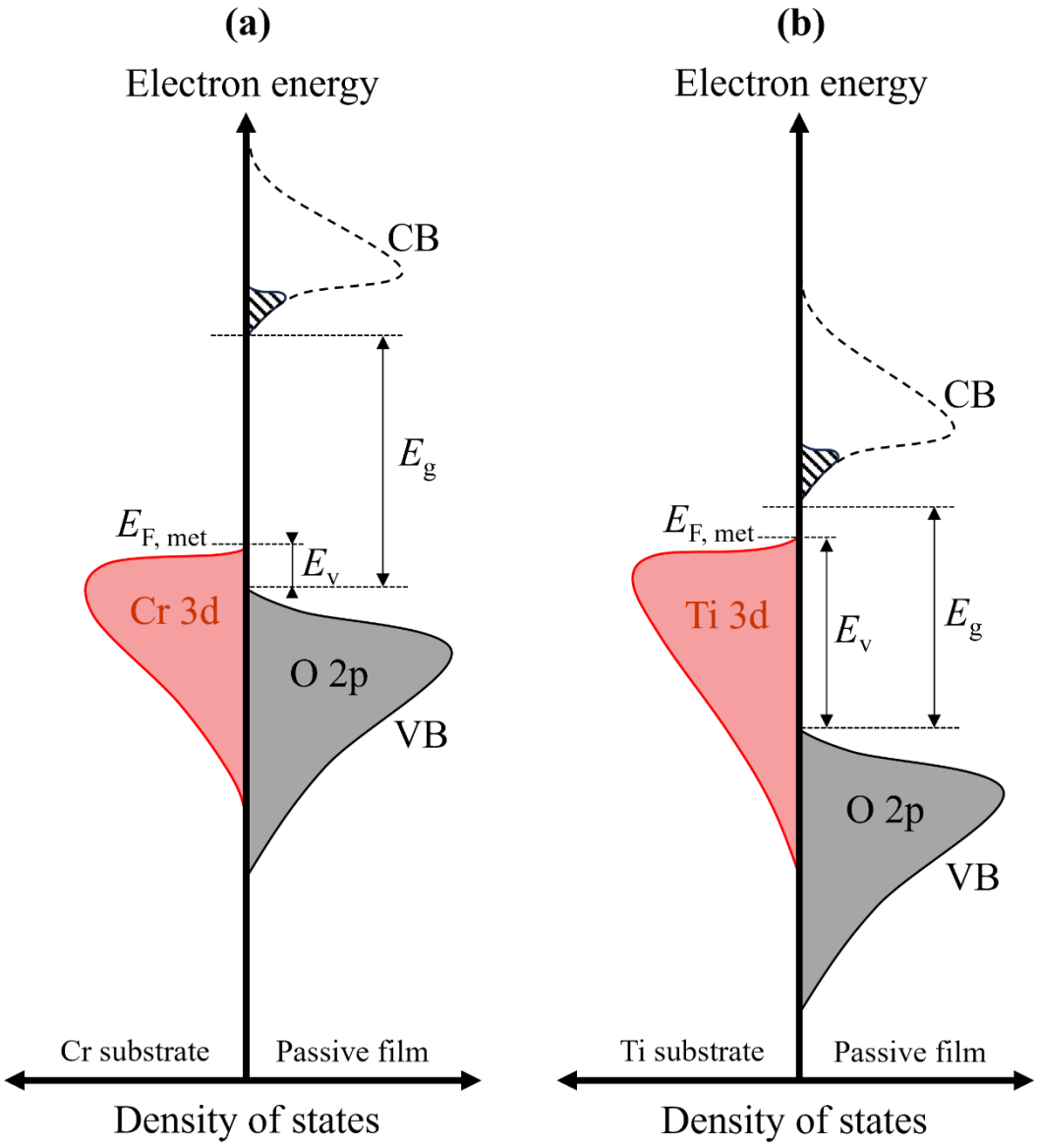

Figure 3.12 Occupation density of the valence and conduction bands for (a) Cr passive film and (b) Ti passive film.

3.5 Conclusions

In the present work, passive films formed on Cr and Ti in a PBS of pH 7 were examined using photoelectrochemical response, electrochemical impedance spectroscopy and XPS. The photoelectrochemical action spectra of the passive films on both metals consist of two straight regions with different slopes, reflecting the duplex structure of the passive films. Considering the potential dependence of the slopes of the photoelectrochemical action spectra and the valence-band edges of the passive films, it is concluded that the passive film on Cr consists of a p-type outer hydroxide layer with an E_g of 2.5 eV and a p-type inner oxide layer with an E_g of 3.6 eV, whereas the passive film on Ti is composed of an n-type outer hydroxide layer with an E_g of 2.5 eV and an n-type inner oxide layer with an E_g of 3.2 eV. In the Mott–Schottky plots of the passivated Ti, only a positive slope is observed, which is attributed to the outer hydroxide layer. In contrast, positive and negative slopes are found for the passivated Cr at less noble potentials than 0 $V_{Ag/AgCl}$ and at higher potentials than 0 $V_{Ag/AgCl}$, respectively. At higher potentials, the space-charge layer built at the interface between the outer hydroxide layer and solution can be in the depleted state, wherein negative slopes are obtained for the p-type semiconductor, whereas at lower potentials, the space-charge layer can be in the inversed state because the Fermi level at the interface approaches the conduction band of the hydroxide layer, in which positive slopes are observed. Based on these results, a partial density of states for passivated metal surfaces was proposed and discussed.

References

1. N. Tomashov, R. Altovsky, and G. Chernova, *J. Electrochem. Soc.*, **108**, 113 (1961).
2. J. Sundgren, P. Bodö, and I. Lundström, *J. Colloid Interface Sci.*, **110**, 9-20 (1986).
3. M. Geetha, A. K. Singh, R. Asokamani, and A. K. Gogia, *Prog. Mater. Sci*, **54**, 397-425 (2009).
4. M. T. Mohammed, Z. A. Khan, and A. N. Siddiquee, *Int. J. Chem. Mol. Nucl. Mater. Metall., Eng* **8**, 726 (2014).
5. B. Thierry, M. Tabrizian, C. Trepanier, O. Savadogo, and L. H. Yahia, *J. Biomed. Mater. Res.*, **51**, 685 (2000).
6. R. Adams, *J. Vac. Sci. Technol. A*, **1**, 12-18 (1983).
7. X. Yue, L. Zhang, Y. Hua, J. Wang, N. Dong, X. Li, S. Xu, and A. Neville, *Appl. Surf. Sci.*, **529**, 147170 (2020).
8. I. Milošev and H.-H. Strehblow, *Electrochim. Acta*, **48**, 2767 (2003).
9. W. Yang, D. Costa, and P. Marcus, *J. Electrochem. Soc.*, **141**, 111 (1994).
10. V. Maurice, W. Yang, and P. Marcus, *J. Electrochem. Soc.*, **145**, 909 (1998).
11. W. S. Kim, H. Tsuchiya, and S. Fujimoto, *Mater. Trans.*, **56**, 593 (2015).
12. K. Azumi and M. Seo, *Corros. Sci.*, **43** 533 (2001).
13. H. Tsuchiya, S. Fujimoto, O. Chihara, and T. Shibata, *Electrochim. Acta*, **47**, 4357 (2002).
14. B. Kraeutler and A. J. Bard, *J.Am. Chem. Soc.*, **100**, 5985 (1978).
15. I. Izumi, W. W. Dunn, K. O. Wilbourn, F.-R. F. Fan, and A. J. Bard, *J. Phys. Chem.*, **84**, 3207 (1980).
16. P. Salvador, *J. Phys. Chem.*, **89**, 3863 (1985).
17. R. AnthonyáSpackman, *J. Chem. Soc. Faraday Trans.*, **92**, 4049 (1996).
18. A. Gad Allah and A. Mazhar, *Corrosion*, **46**, 306 (1990).
19. W. Badawy, A. Felske, and W. Plieth, *Electrochim. Acta*, **34**, 1711 (1989).
20. D.Y. Kim, S. Ahn, H.S. Kwon, *Thin Solid Films*, **513**, 212 (2006).
21. M. Santamaria, F. Di Quarto, and H. Habazaki, *Corros. Sci.*, **50**, 2012 (2008).

22. N.T.C. Oliveira, A.C. Guastaldi, S. Piazza, and C. Sunseri, *Electrochim. Acta*, **54**, 1395 (2009).
23. H. Tsuchiya, S. Fujimoto, and T. Shibata, *J. Electrochem. Soc.*, **151**, B39 (2004).
24. H. Jang and H. Kwon, *ECS Tran.*, **3**, 1 (2007).
25. G. Tranchida, F. Di, Franco, and M. Santamaria, *J. Electrochem. Soc.*, **167**, 061506 (2020).
26. G. Tranchida, M. Clesi, F. Di Franco, F. Di Quarto, and M. Santamaria, *Electrochim. Acta*, 273, 412 (2018).
27. D. A. Shirley, *Phys. Rev.B*, **5**, 4709 (1972).
28. S. Fujimoto, O. Chihara, and T. Shibata, *Mater. Sci. Forum*, **289-292**, 989 (1998).
29. H. Tsucihya and S. Fujimoto, *Sci. Tech. Adv. Mater.* **5**, 195 (2004).
30. F. Di Quarto, S. Piazza, and C. Sunseri, *Corros. Sci.*, **31**, 721 (1990).
31. M. Rao, K. Rajeshwar, and V.R. Pai Verneker, *J. Phys. Chem.*, **84**, 1987 (1980).
32. A. E. Nogueira, L.S. Ribeiro, L.F. Gorup, G.T.S.T. Silva, F.F.B. Silva, C. Ribeiro, and E.R. Camargo, *Int. J. Photoenergy*, **2018**, 6098302 (2018).
33. S. Fujimoto, S. Kawachi, and T. Shibata, *J. Japan Inst. Metals*, **63**, 375 (1999).
34. S. Fujimoto, T. Yamada, and T. Shibata, *J. Electrochem. Soc.*, **145**, L79 (1998).
35. S.-C. Kim, T. Hanawa, T. Manaka, H. Tsuchiya, and S. Fujimoto, *Sci. Tech. Adv. Mater.*, **23**, 322 (2022).
36. A. P. Singh, N. Kodan, and B. R. Mehta, *Appl. Surf. Sci.*, **372**, 63 (2016).
37. Y. Fukuda, F. Honda, and J.W. Rabalais, *Surf. Sci.*, **91**, 165 (1980).
38. K. Asami and K. Hashimoto, *Corros. Sci.*, **17**, 559 (1977).
39. M. Kozlowski and W. H. Smyrl, *Electrochim. Acta*, **34**, 1763 (1989).

Chapter 4

Numerical simulation of photocurrent transients generated from passive films and anodic films on Ti

4.1 Introduction

Passive films formed on many metals and alloys have been reported to exhibit semiconductive behavior that is considered to be closely related to the corrosion resistance of the metallic substrates [1, 2]. The photoelectrochemical response, in some case called as photocurrent measurements/photocurrent spectroscopy, is one of the most widely used techniques to investigate the semiconductive properties of passive films, based on the generation, annihilation and transport of photo-excited carriers within passive films. However, the analysis frequently performed on photocurrent spectra only reveals the band gap energy and flat-band potential of passive films and the type of semiconductor (n-type or p-type) on one hand [3-5], but further information on physical properties of passive films is required to discuss the protectiveness of passive films in corrosive environments on the other hand. Therefore, supplementary experiments such as electrochemical impedance spectroscopy have been utilized to reach more accurate understanding on the electronic structure of passive films.

Photocurrents generated from passive films and anodic films exhibit some transients during photoirradiation, that is, current changes with time. In particular, passive and anodic films on Fe-based alloys including pure Fe [6-9] and Ti alloys including pure Ti [10-12] have been extensively studied, revealing that the shape of the transients varies depending on the composition of passive and anodic films and electrode potential. Furthermore, photocurrent transients are reported to vary depending on the morphology of TiO_2 for examples, flat, nanotubular, nanoporous or nanoflake layers [13-16].

Azumi *et al*. attributed the photocurrent transients generated from anodic oxide film on TiN coating layer to the accumulation of photo-excited carriers at the interface between the oxide film and the electrolyte [17]. Peter suggested that the unpinning of the band edge should be considered to interpret the photocurrent transient and that the concentration of accumulated holes at the surface causes the unpinning of the band edge [18]. Furthermore, surface states where charge carriers are recombined and/or are trapped, followed by reacting redox species, have also been reported to affect photocurrent transients [19, 20]. Zhang *et al.* applied numerical simulations to discuss photocurrent transients generated from oxide films on 304L stainless steel [21]. As properties of passive films are associated with photocurrent transient, the numerical analysis of photocurrent transients can provide various properties of passive films. To the best of our knowledge, there have been no studies in which various properties of passive and anodic films on Ti have been estimated based on numerical simulation of photocurrent transient.

In the present work, the author reports a numerical simulation of photocurrent transients generated from passive films and anodic films formed on pure Ti to obtain various semiconductive properties by considering the generation, recombination and transports of photo-excited carriers. The fitting of simulated photocurrent transients with experimentally obtained ones provided semiconductive properties such as electron mobility, donor density, recombination coefficient and interfacial reaction rate coefficient.

4.2 Experimental

4.2.1 Preparation of samples

Specimens used in the present work were prepared from a sheet of CP Ti. A coupon of Ti was connected with a wire for electrical conduction and then embedded in an epoxy resin to prepare a specimen. The specimen surface was successively polished with SiC papers up to 2000 grit and finally mirror finished with 0.25 μm diamond paste. Afterwards, ultrasonic

cleaning was performed in the order of acetone, ethanol, and distilled water. The area of the specimen surface exposed to a solution was 28.3 mm^2 and the rest was covered with a polytetrafluoroethylene (PTFE) adhesive tape. The solution used in this work was a phosphate buffer solution (pH = 7) deaerated with high-purity N_2 gas for at least 2 h prior to electrochemical measurements. For all electrochemical measurements, a conventional electrochemical cell equipped with an Ag/AgCl reference electrode, and a platinum counter electrode was used. The specimen was anodically polarized for 2 h at various film formation potentials (E_f): low potentials of −0.2, 0, and 0.2 $V_{Ag/AgCl}$ and high potentials of 3, 5, and 7 $V_{Ag/AgCl}$.

4.2.2 Photoelectrochemical response

Photocurrent transients were recorded for the passive films prepared according to the above-mentioned procedure. Monochromated light with a wavelength of 300 nm (4.13 eV) generated by a 150 W xenon arc lamp was irradiated to a passive film at the E_f, causing the change in current during the photoirradiation for 20 s, that is photocurrent transient. Note that the photocurrent measurements were performed after the dark current became very low down to a negligible level. Then the measuring potential (E_m) was shifted stepwisely in the less noble direction with the internal of 0.1 V and a photocurrent transient was recorded again. This process was repeated as long as a photocurrent transient can be obtained. The measurements were performed using a low-pass filter with a cut off frequency of 4 Hz and a differential amplifier.

4.3 Numerical simulation model

Passive films on Ti are known to consist of an inner oxide layer and an outer hydroxide layer; however, the author recently revealed that the photoelectrochemical responses from the outer hydroxide layer were relatively small compared with those from the inner oxide layer [5].

Therefore, in the present work, the contribution from the outer hydroxide layer was not considered, that is, photocurrent transients were assumed to be generated in the inner oxide layer and were analyzed based on the schematic diagram shown in Fig. 4.1. In this model, the space charge layer in contact with the electrolyte exhibits upward bending. The outermost surface of the oxide layer (TiO_2) was taken as the origin, and the *x*-axis was set in the direction toward the metal substrate. In addition, photo-excitation which contributes to generate charge carriers in the valence band as well as the conduction band was assumed to occur only in the space charge layer. Electrons that reach the outside of the space charge layer ($x = W$) are transported to the metal substrate whereas the transport of holes to the substrate is assumed to be ignored following two reasons: i) carrier transport by concentration gradient is less than transport by electric field, ii) the amount of holes transported to the metal substrate is significantly less than electrons, which are the majority carriers in an n-type semiconductor. In contrast, holes that reach the other edge ($x = 0$) react with some redox species in the electrolyte, but electrons at the surface are assumed not to react with any redox species due to the Schottky barrier. This interfacial reaction will be explained later. Based on these assumptions, equations for the generation of charge carriers by light absorption, carriers transport in the conduction band and valence band, and the annihilation of carriers by recombination were established. The one-dimensional drift-diffusion model provides a theoretical analysis of the transport of the carriers in semiconductor [22]. Based on the model, the generation of photocurrent due to the transport of charge carriers in passive film on Ti with an n-type semiconductive nature was considered according to the following procedure.

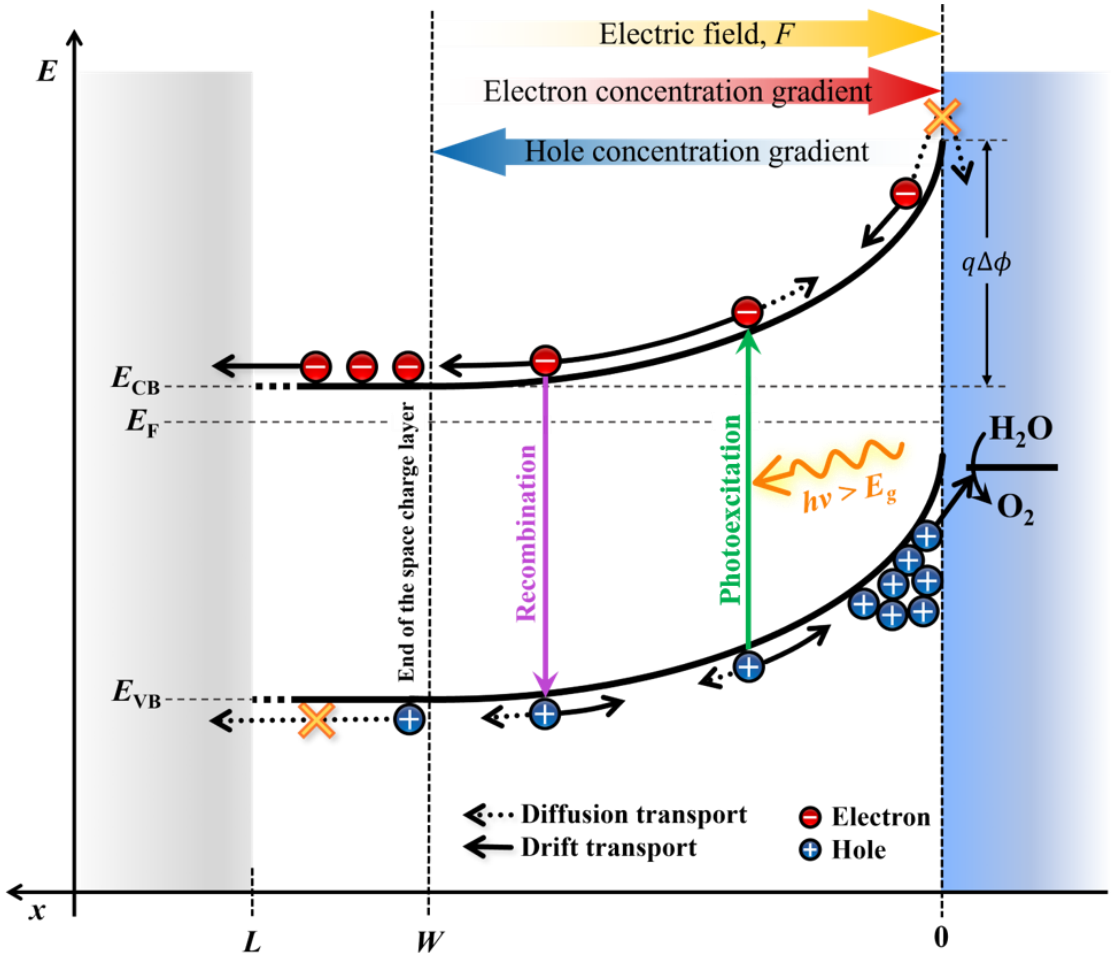

Figure 4.1 Schematic illustration on the energy diagram of an n-type semiconductor and some phenomena occurred by photoexcitation. L and W indicate the thickness of the n-type semiconductor and the width of a space charge layer, respectively. E_{VB} and E_{CB} represent the valence and conduction bands of the semiconductor and E_F is the Fermi level.

4.3.1 Changes in the concentration of charge carriers

As the light intensity along the *x*-axis attenuates depending on the position *x*, the intensity of the incident light at *x* is described as follows.

$$I_{in}(x) = I_0 exp\ (-\alpha x) \tag{4.1}$$

In addition, light is reflected at the interface between the metal substrate and the oxide layer, and the intensity of the reflected light at *x* is also expressed as follows.

$$I_{ref}(x) = I_0 exp\{-\alpha(2L - x)\} \tag{4.2}$$

where I_0 is the light intensity at $x = 0$, α is the absorption coefficient of the film, and L is the film thickness. As the light absorption rate is converted into the number of photons using the Eqs. (4.1) and (4.2), and the number of absorbed photons can be assumed to be equal to the number of photo-generated carriers, the number of photo-generated carriers at the position *x*, n_G (x) and $p_G(x)$, can be expressed, according to the following equation.

$$n_G(x) = p_G(x) = \frac{\lambda}{hc} I_0 \alpha [exp\ (-\alpha x) + exp\{-\alpha(2L - x)\}] \tag{4.3}$$

where λ, h and c express the wavelength of light, the Planck's constant, and the light speed within the film, respectively.

Not only photo-induced generation of charge carriers but also the annihilation of photo-excited charge carriers by recombination should be considered. As the recombination rate is proportional to the photo-excited electron concentration and the hole concentration, the recombination rate of electrons and holes, at the position *x*, $n_R(x)$ and $p_R(x)$, can be expressed as follows.

$$n_R(x) = p_R(x) = kn_x p_x \tag{4.4}$$

where n_x and p_x represent the electron concentration in the conduction band and the hole concentration in the valence band at the position *x*, respectively, and *k* is the recombination coefficient.

The transport of charge carriers at the position *x* due to the electric field built in the film can be described as the product of carrier concentration, mobility, and electric field.

$$n_{drift}(x) = \mu_n n_x F_x \tag{4.5 a}$$

$$p_{drift}(x) = \mu_p p_x F_x \tag{4.5 b}$$

In the equations described above, μ_n and μ_p are the mobility of electron and hole, respectively, and F_x is the internal electric field at the position *x* in the film. On the other hand, the transport of charge carriers at the position *x* due to the concentration gradient within the film can be presented as the product of diffusion coefficient of charge carriers (electron or hole) and the concentration gradient of the carriers.

$$n_{diff}(x) = D_n \frac{dn_x}{dx} \tag{4.6 a}$$

$$p_{diff}(x) = D_p \frac{dp_x}{dx} \tag{4.6 b}$$

where D_n and D_p are the diffusion coefficients of electron and hole, respectively. Therefore, based on the Eqs. (4.5) and (4.6), the flux of electrons and holes at position *x* can be expressed by considering the drift in the electric field F_x and the diffusion under the carrier concentration gradient.

$$\frac{dn_x}{dx} = -\mu_n n_x F_x - D_n \frac{dn_x}{dx} \quad (4.7\text{ a})$$

$$\frac{dp_x}{dx} = -\mu_p p_x F_x + D_p \frac{dp_x}{dx} \quad (4.7\text{ b})$$

where μ_n and μ_p are the mobility of electron and hole whereas D_n and D_p are the diffusion coefficient of electron and hole, respectively. The continuity equations for the electron and hole concentrations with position x and time t under light irradiation can be defined as follows [23].

$$\frac{\partial n_{x,t}}{\partial t} = \mu_n \frac{\partial n_{x,t} F_{x,t}}{\partial x} + D_n \frac{\partial^2 n_{x,t}}{\partial x^2} + \frac{\lambda}{hc} I_0 \alpha [exp\,(-\alpha x) + exp\{-\alpha(2L - x)\}] - k n_{x,t} p_{x,t} \quad (4.8\text{ a})$$

$$\frac{\partial p_{x,t}}{\partial t} = -\mu_p \frac{\partial p_{x,t} F_{x,t}}{\partial x} + D_p \frac{\partial^2 p_{x,t}}{\partial x^2} + \frac{\lambda}{hc} I_0 \alpha [ex\,p(-\alpha x) + exp\{-\alpha(2L - x)\}] - k n_{x,t} p_{x,t} \quad (4.8\text{ b})$$

where $F_{x,t}$ is the electric field as a function of the position, x, and the time, t. The calculation method for these equations is described below.

4.3.2 Potential distribution in the film

Photo-excited carriers in the space charge layer in n-type semiconductor are transported either toward the metal substrate or to the interface with the electrolyte along the electron gradient and the concentration gradient, resulting in a significant change in the distribution of carriers. As a result, the potential distribution changes every moment, which in turn affects the transport of carriers. The following Poisson's equation is used to derive the relationship between charge concentration ρ the electron potential ϕ.

$$-\frac{d^2\phi}{dx^2} = \frac{dF}{dx} = \frac{\rho_x}{\varepsilon_0 \varepsilon_r} \quad (4.9)$$

where ε_0 and ε_r express the vacuum permittivity and the relative permittivity of TiO_2, respectively. The charge concentration in the semiconductor ρ can be described as follows:

$$\rho_x = q(N_{D,x} - N_{A,x} + p_x - n_x) \tag{4.10}$$

where N_D and N_A denote the donor and the acceptor densities, respectively. In the case of n-type semiconductor, N_A is considered zero. Therefore, from the Eqs. (4.9) and (4.10), the following equation was obtained.

$$\frac{dF}{dx} = \frac{q}{\varepsilon_0 \varepsilon_r}(N_{D,x} + p_x - n_x) \tag{4.11 a}$$

The electric field F_x at position x was obtained by integrating Eq. (4.11 a).

$$F_x = F_0 + \frac{q}{\varepsilon_0 \varepsilon_r}\int_0^x (N_{D,x} + p_x - n_x)dx \tag{4.11 b}$$

where F_0 is the electric field at the interface between the semiconductor layer and the electrolyte ($x = 0$).

4.3.3 Interfacial reaction at the TiO_2 / electrolyte interface

Photocurrents generated in n-type semiconductor are affected not only by the transport of electrons to the metal substrate but also by the consumption of holes at the semiconductor film/electrolyte interface, mostly the water oxidation to generate oxygen. As a plenty amount of water is present in this system, the consumption of holes can be assumed to be proportional to the concentration of accumulated holes at the TiO_2 / electrolyte interface. Therefore, the interface reaction rate can be calculated, according to the following equation.

$$\rho_{inter} = p_0 l \tag{4.12}$$

where p_0 is the concentration of holes at $x = 0$, and l is the interface reaction rate coefficient.

4.3.4 Calculation method of the proposed numerical model

To perform numerical analysis on photocurrent transients, the partial differential equations (the Eqs. (4.8 a) and (4.8 b)) were discretized using a finite difference method (the explicit scheme). The algebraic equations obtained are described below.

$$\frac{n_{x,t+1}-n_{x,t}}{\Delta t} = \mu_n \frac{n_{x,t}F_{x,t}-n_{x-1,t}F_{x-1,t}}{\Delta x} + D_n \frac{n_{x+1,t}F_{x+1,t}-2n_{x,t}F_{x,t}+n_{x-1,t}F_{x-1,t}}{\Delta x^2} + \frac{\lambda}{hc} I_0 \alpha [exp\,(-\alpha x) + exp\{-\alpha(2L-x)\}] - k n_{x,t} p_{x,t} \tag{4.13 a}$$

$$\frac{p_{x,t+1}-p_{x,t}}{\Delta t} = -\mu_p \frac{p_{x+1,t}F_{x+1,t}-p_{x,t}F_{x,t}}{\Delta x} + D_p \frac{p_{x+1,t}F_{x+1,t}-2p_{x,t}F_{x,t}+p_{x-1,t}F_{x-1,t}}{\Delta x^2} + \frac{\lambda}{hc} I_0 \alpha [exp\,(-\alpha x) + exp\{-\alpha(2L-x)\}] - k n_{x,t} p_{x,t} \tag{4.13 b}$$

The forward difference method was similarly applied to Eq. (4.11 b) a to calculate the electric field in the semiconductor and thus Eq. (4.14) was obtained.

$$F_x = F_0 + \frac{q\Delta x}{\varepsilon_0 \varepsilon_r} \sum_{x=0}^{n-1} \left(N_{D,x} + p_x - n_x\right) \tag{4.14}$$

The initial value of F_0 was estimated, based on the assumption that the electric field at the position $x = W$ equals 0. This assumption led to the following equation.

$$F_w = 0 = F_0 + \frac{q\Delta x}{\varepsilon_0 \varepsilon_r} \sum_{x=0}^{W} \left(N_{D,x} + p_x - n_x\right) \tag{4.15 a}$$

As the concentrations of electrons and holes, i.e., n_x and p_x, respectively, were quite small compared to that of the donor density N_D, they were ignored in the initial state before photoirradiation. Therefore, the initial F_0 was estimated using the donor density N_D and the width of the space charge layer W in the n-type film, both of which were calculated using the Mott-Schottky plot for the film.

$$F_0 = -\frac{q\Delta x}{\varepsilon_0 \varepsilon_r} \sum_{x=0}^{W} N_{D,x} \quad (4.15\ b)$$

All electrons that passed through the end of the space charge layer by drift and diffusion were assumed to have reached the semiconductor-metal interface, after which they were then transported to the metal substrate. Therefore, the photocurrent caused by the electron transport can be obtained as follows.

$$I_{ph} = A\left(-q\mu_n n_W F_{W-1} - qD_n \frac{n_W - n_{W-1}}{\Delta x}\right) \quad (4.16)$$

where I_{ph} is the photocurrent and A is the area of the electrode.

In this work, the position x inside the space charge layer was finely divided into 0.05 nm (Δx), and the concentrations of n and p were calculated every 1 ms (Δt).

4.4 Results and discussion

4.4.1 Photocurrent transients on passive films and anodic films

In this work, although both were formed by anodic polarization, the films formed on pure Ti at potentials lower than 1 $V_{Ag/AgCl}$ are called passive films, whereas those formed at potentials higher than 1 $V_{Ag/AgCl}$ are called anodic films. Figure 4.2 shows the photocurrent transients of passive films and anodic films formed on Ti. As apparent from the figures,

positive photocurrents were observed at all the E_ms and the photocurrents increased with increasing the E_m, indicating that the passive and anodic films formed on Ti exhibited typical n-type semiconductive behavior. As shown in the figure, the photocurrent transients can be classified into two types. The photocurrent exhibited an initial increase in the anodic current, followed by a drastic decrease and a subsequent gradual decrease to a steady state value during irradiation. Immediately after the irradiation was terminated, the photocurrent rapidly dropped to a negative value and then increased again to its original value. This type of transient (defined as spike-type) was observed for passive films regardless of the E_m and for anodic films at lower E_ms. In contrast, the others exhibited an almost constant value just after an initial rapid increase during irradiation. After the termination of irradiation, it rapidly attenuated to its original value. This flat-type transient appeared in the anodic films at higher E_ms. The variation in the shape of photocurrent transient has been also found in nanostructured TiO_2 layers [13-16]. In addition, interestingly, the amplitude of steady-state photocurrent in the flat-type transient is comparable to the one reported for as-formed amorphous nanotubular TiO_2 layer consisting of individual tubes with a length of approximately 2.5 μm and a diameter of approximately 100 nm [13].

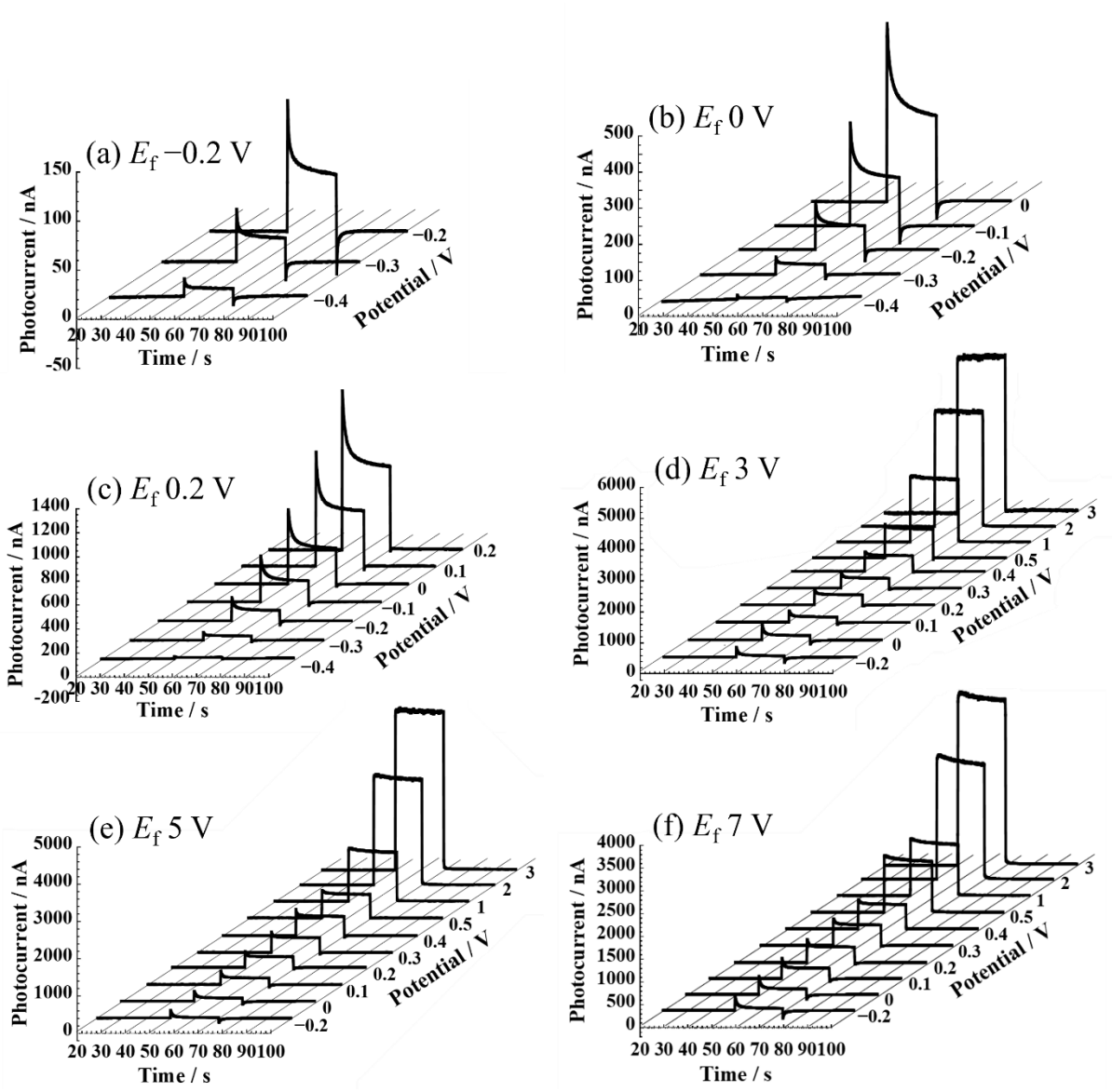

Figure 4.2 Photocurrent transients observed for passive films and anodic films formed at various film formation potentials, E_fs, on pure Ti.

4.4.2 Numerical simulation of photocurrent transient

In the present work, numerical simulation on photocurrent transient was performed for 3 s from the beginning of irradiation. The specific values and variables used in the numerical simulation of photocurrent transient are listed in Table 4.1. Screening the variables was repeated until the best fit of simulated transient to experimentally obtained one was achieved. The variables used in optimization of fitting are later organized and their characteristics will be explained. Figure 4.3 compares the measured transients with the simulated ones obtained after screening for spike-type and flat-type transients. In Figs. 4.3 (a − f), the photocurrent transients obtained at the E_m of −0.2 $V_{Ag/AgCl}$ not only for the passive films but also the anodic films roughly matched the simulated ones. However, the deviation of the simulated transient from the experimentally obtained one could be recognized for the films formed at the potentials higher than 0 $V_{Ag/AgCl}$. The deviation between the simulated transients and the experimentally obtained ones became larger with increasing the E_f. In contrast, as shown in Fig. 4.3 (g − i), the simulated transients were in good accordance with the experimentally obtained ones measured at 1 $V_{Ag/AgCl}$ for the anodic films.

Table 4.1 Specific values and variables used in the simulation. The marks, *, indicate variables in the study.

Parameter	Symbol	Numerical value or equation
Planck's constant (J s)	h	6.63×10^{-34}
Boltzmann's constant (J K^{-1})	k_B	1.38×10^{-23}
Electric charge (C)	q	1.6×10^{-19}
Vacuum permittivity (F m^{-1})	ε_0	8.85×10^{-12}
Relative permittivity of TiO_2	ε_r	83
Thermodynamic temperature (K)	T	300
Light speed in oxide (m s^{-1})	c	8.82×10^{7}
Irradiated light intensity (W)	I_0	2.80×10^{-3}
Irradiated light wavelength (m)	λ	300×10^{-9}
Absorption coefficient (m^{-1})	α	3.13×10^{7}
Electron diffusion coefficient (m^2 s^{-1})	D_n	$\mu_n k_B T/q$
Hole diffusion coefficient (m^2 s^{-1})	D_p	$\mu_p k_B T/q$
Electric field (V m^{-1})	F	$\frac{qN_D}{\varepsilon_0 \varepsilon_r}(x - W)$
Space charge layer width (m)	W	$\sqrt{\frac{2\varepsilon_0 \varepsilon_r \Delta\phi}{qN_D}}$
Schottky Barrier Height (V)	$\Delta\phi$	$\phi_m - \phi_{fb}$
Measuring potential (V vs. Ag/AgCl)	ϕ_m	–
Flat band potential (V vs. Ag/AgCl)	ϕ_{fb}	-0.5
Charge density (C m^{-3})	ρ	qN_D (Before light irradiation)
Hole mobility (m^2 V^{-1} s^{-1})	μ_p	$0.957\mu_n$
Electron mobility (m^2 V^{-1} s^{-1})	μ_n	*
Donor density (m^{-3})	N_D	*
Recombination coefficient	k	*
Interfacial reaction rate coefficient	l	*
Electron concentration (m^{-3})	n	–
Hole concentration (m^{-3})	p	–

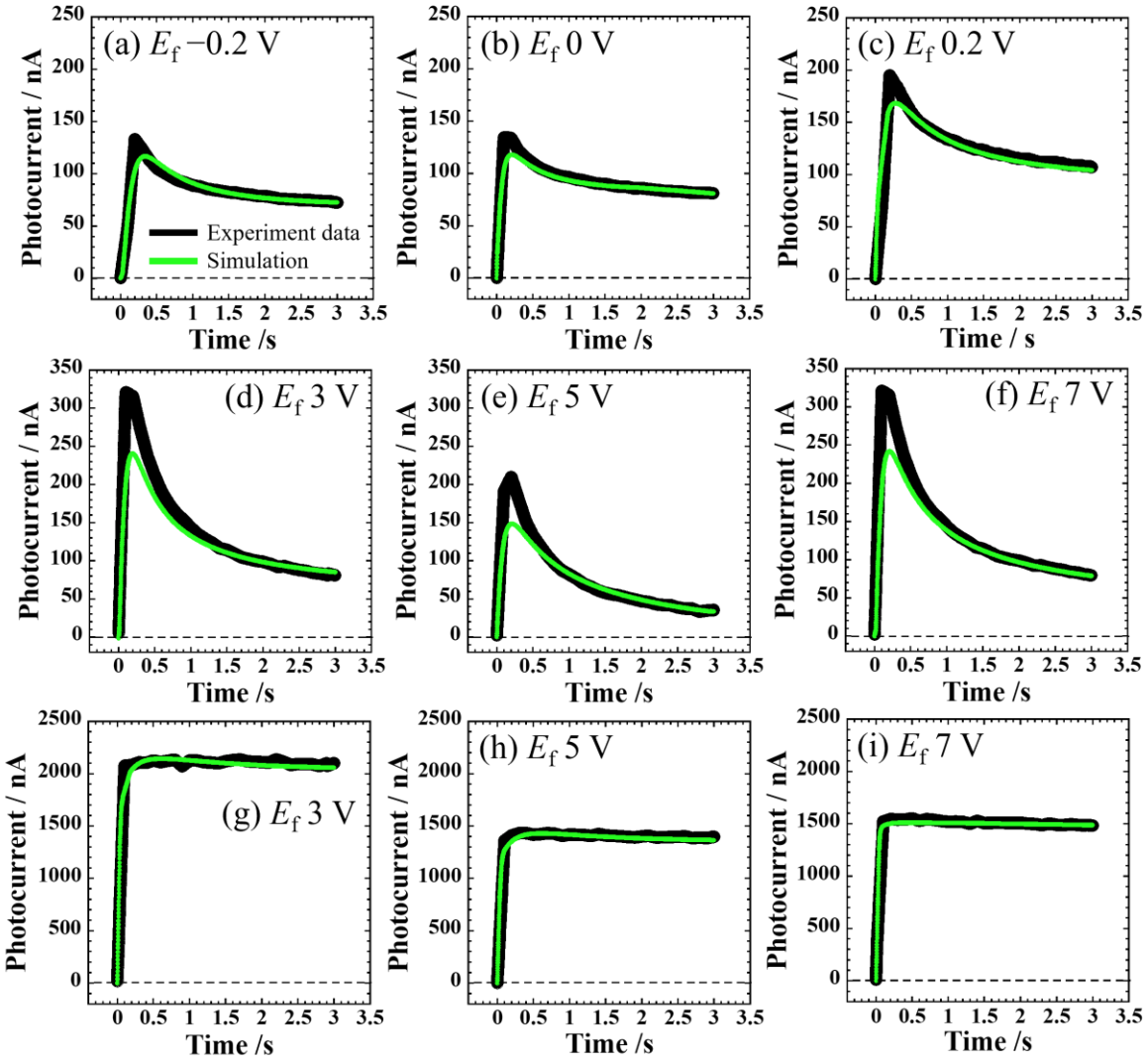

Figure 4.3 Comparison of photocurrent transients with simulated ones. The spike-type transients were observed at −0.2 $V_{Ag/AgCl}$ for passive and anodic films (a – f) whereas the flat-type transients were observed at 1 $V_{Ag/AgCl}$ for anodic films (g – i).

Figure 4.4 summarizes several properties of the passive and anodic films by the fitting of in the numerical simulation, several properties of the passive and anodic films were obtained, and the results are summarized in Fig. 4.4. These properties are classified into two categories: the ones which are almost constant independent of the E_m, and the others which present drastic decrease at lower potentials. The electron mobility and the interfacial reaction rate coefficient belong to the former, that is, both slightly increase with increasing the E_m as shown in Figs. 4.4 (a) and (b). These properties are considered inherent to the films. In addition, the electron mobility and the interfacial reaction rate coefficient are largely dependent on the E_f, that is, those of the anodic films formed at potentials higher than 3 $V_{Ag/AgCl}$ are larger than those of the passive films formed at lower potentials than 0.2 $V_{Ag/AgCl}$. This is also reasonable as the E_f causes some changes in other properties that may affect the electron mobility and the interfacial reaction rate coefficient, such as donor density. On the other hand, as shown in Figs 4.4 (c) and (d), the donor density and recombination coefficient belong to the latter, that is, they drastically decrease with increasing the E_m in the lower potential region and then gradually decrease. These results may imply that donor and recombination sites are not uniformly distributed in the films, that is, they are relatively higher near the outermost surface compared to those in the bulk, and they decrease with increasing distance from the surface. In the present work, the simulation was carried out based on the changes of concentration in charge carriers which are generated within the space charge layer by light-irradiation, that is, the calculation targets a limited region of the electronic band structure within the films. Therefore, in the lower E_m region, the estimated donor density and recombination coefficient at a E_m are determined by the higher number of donor and recombination site distributed within the space charge layer that is built near the surface. As the width of the space charge layer increases with increasing the E_m, the estimated donor density and recombination coefficient are likely to be determined not only by the higher number of donor and recombination sites near the surface but also by the lower

number of them which are distributed in the inner region of the space charge layer built at a higher E_m. Therefore, the estimated donor density and recombination coefficient were considered to decrease, as shown in Figs. 4(c) and (d). The proposed numerical model was useful for quantitative analysis by deriving the semiconductive physical properties inside the film through photocurrent transient fitting. The potential dependence of physical properties could be confirmed, and the recombination rate and interfacial reaction rate could be derived as coefficient values. In addition, the derived electron mobility and donor density are within the range of values obtained experimentally and computationally in previous studies [24, 25].

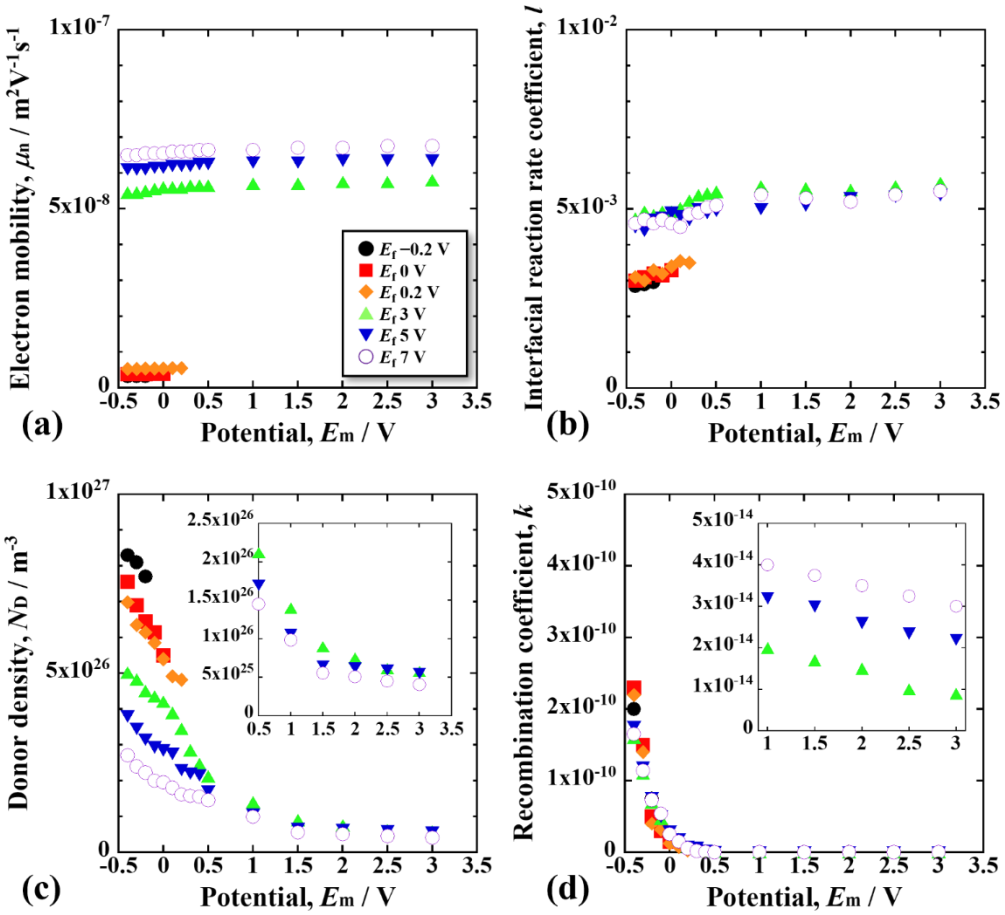

Figure 4.4 Estimated properties of passive and anodic films by the fitting of simulated photocurrent transients with measured ones.

4.5 Conclusion

In this study, a numerical simulation model on photocurrent transients generated on passive films and anodic films on Ti was proposed. The photoelectrochemical experiments were carried out to obtain the references of photocurrent transient for the fitting. In the experiment, positive photocurrents were observed for all the films examined, and increased with increasing the E_m, indicating that the films behaved as n-type semiconductor. The shape of the photocurrent transients was classified into two types: the spike-type transient and the flat-type transient. The spike-type transients were obtained for the passive films as well as the anodic films at the lower E_ms whereas the flat-type ones were observed only for the anodic films at the higher E_ms. The partial differential equations that express the change in the concentrations of carries with the time and the position in the films were introduced to simulate the photocurrent transients, based on the generation and annihilation of carriers and their transports by the drift and diffusion and the equations were discretized using a finite difference method (the explicit scheme) to conduct the numerical simulation. The fitting of the photocurrent transients obtained by the simulation to the experimentally obtained ones led to the estimation of several properties of the films such as the electron mobility, the donor density, the recombination coefficient, and the interfacial reaction rate coefficient. The electron mobility and interfacial reaction are considered intrinsic characteristics of the film. These two factors were not significantly related to the photocurrent transient. On the other hand, the donor density and recombination rate had a clear dependence on the E_m.

References

1. J. Pan, C. Leygraf, D. Thierry, and A. Ektessabi, *J. Biomed. Mater. Res.*, **35**, 309 (1997).
2. S. Radhakrishnan, C. Siju, D. Mahanta, S. Patil, and G. Madras, *Electrochim. Acta*, **54**, 1249 (2009).
3. S. Fujimoto, O. Chihara, and T. Shibata, Mater. *Sci. Forum*, **989**, 289 (1998).
4. H. Tsuchiya, S. Fujimoto, O. Chihara, and T. Shibata, *Electrochim. Acta*, **47**, 4357 (2002).
5. S.-C. Kim, T. Hanawa, T. Manaka, H. Tsuchiya, and S. Fujimoto, *Sci. Tech. Adv. Mater.*, **23**, 322 (2022).
6. L.M. Abrantes and L.M. Peter, *J. Electroanal. Chem.*, **150**, 593 (1983).
7. K. Azumi, T. Ohtsuka, and N. Sato, *Corros. Sci.*, **31**, 715 (1990).
8. G. Tranchida, F. Di Franco, and M. Santamaria, *J. Electrochem. Soc.*, **167**, 061506 (2020).
9. G. Tranchida, M. Clesi, F. Di Franc. F. Di Quarto, and M. Santamaria, *Electrochim. Acta*, **273**, 412 (2018).
10. J.F. McAleer and L.M. Peter, *Faraday Discuss. Chem. Soc.*, **70**, 67 (1980).
11. M.R. Kozlowski, P.S. Tyler, W.H. Smyrl, and R.T. Atanasoski, *J. Electrochem. Soc.*, **136**, 442 (1989).
12. N. Oliveira, A. C. Guastaldi, S. Piazza, and C. Sunseri, *Electrochim. Acta*, **54**, 1395 (2009).
13. H. Tsuchiya, J.M. Macak, A. Ghicov, A.S. Räder, L. Taveira, and P. Schmuki, *Corros. Sci.*, **49**, 203 (2007).
14. T. Oekermann, T. Yoshida, J. Nakazawa, S. Yasuno, T. Sugiura, and H. Minoura, *Electrochim. Acta*, **52**, 4325 (2007).
15. H. Sopha, M. Krbal, S. Ng, J. Prikryl, R. Zazpe, F.K. Yam, and J.M. Macak, *Appl. Mater. Today*, **9**, 104 (2017).
16. X. Zhou, N. Denisov, G. Cha, I. Hwang, and P. Schmuki, *Electrochem. Commun.*, **124**, 106937 (2021).
17. K. Azumi, S. Watanabe, M. Seo, I. Saeki, Y. Inokuchi, P. James, and W.H. Smyrl, *Corros. Sci.*, **40**, 1363 (1998).
18. L. M. Peter, A. B. Walker, T. Bein, A. G. Hufnagel, and I. Kondofersky, *J. Electroanal. Chem.*, **872**, 114234 (2020).
19. L. Peter, J. Li, and R. Peat, *J. Electroanal. Chem. Interfacial Electrochem.*, **165**, 29 (1984).
20. P. M. Hoffmann, G. Oskam, and P. C. Searson, *J. Appl. Phys.*, **83**, 4309 (1998).

21. S. Zhang, L. Jia, and T. Yu, *Electrochim. Acta*, **89**, 253 (2013).
22. W. Van Roosbroeck, *Bell Syst. Tech. J.*, **29**, 560 (1950).
23. J. F. Burgler, R. E. Bank, W. Fichtner, and R. K. Smith, *IEEE TCAD*, **8**, 479 (1989).
24. T. Ohtsuka and T. Otsuki, *Corros. Sci.*, **40**, 951 (1998).
25. Y. Tu, J. Lin, W. Lin,C. Liu, J. Shyue, and W. Su, *Cryst. Eng. Comm.*, **14**, 4772 (2012).

Chapter 5
General conclusions

In the present study, the author investigated semiconductive properties of passive films on Cr and Ti using photoelectrochemical response, electrochemical impedance spectroscopy and X-ray photoelectron spectroscopy. In addition, a simulation model on photocurrent transients was developed. As a result, the following conclusions have been drawn.

Chapter 1 introduced several bases on the passivity of metallic materials and the semiconductor electrochemistry to help the readership understand the contents of the present thesis. In particular, Cr and Ti are focused. In this chapter, the principles of electrochemical measurements and surface analytical techniques used in the present work are briefly described, and findings in literature are summarized. Finally, the purpose of the present work is mentioned.

Chapter 2 has shown the electric band structures and band gap energies (E_g) of passive films formed on Ti passivated for 1 h in simulated bioliquids, such as Hanks and saline solutions. The surface of the passive films was characterized using X-ray photoelectron spectroscopy (XPS), and their semiconductor properties were evaluated by photoelectrochemical response. It was found from XPS that passive films consisted of a very thin TiO_2 layer containing small amounts of Ti_2O_3 and TiO, hydroxyl groups, and water. During polarization in Hanks, calcium and phosphate ions were incorporated or formed calcium phosphate, but not in saline. The photoelectrochemical response revealed that the passive films on Ti consist of two n-type semiconductors: an inner oxide layer with a large E_g and an outer hydroxide layer with a small E_g. In Hanks, the E_gs were 3.3 – 3.4 eV for the inner oxide layer and 2.9 eV for the outer hydroxide layer whereas in saline, the E_gs were 3.3 eV for the inner layer and 2.7 eV for the outer layer. The E_g of the outermost surface was smaller than that of TiO_2 ceramics, which is probably one of the principles of the excellent biocompatibility of Ti among metals.

Chapter 3 reports that the electronic band structures, including semiconductive properties, of passive films formed on Cr and Ti in a phosphate buffer solution of pH 7 were evaluated using photoelectrochemical response, electrochemical impedance spectroscopy and X-ray photoelectron spectroscopy. Based on the results obtained in the photoelectrochemical response and the electrochemical impedance spectroscopy, the electronic structure models of the passive films were proposed: the passive films on Cr consisted of the inner p-type oxide layer with the band gap energy, E_g, of 3.6 eV and the outer p-type hydroxide layer with the E_g of 2.5 eV whereas those on Ti consisted of the inner n-type oxide layer with the E_g of 3.2 eV and the outer n-type hydroxide layer with the E_g of 2.5 eV. The type as semiconductor evaluated for the oxide and hydroxide layers was strongly supported by the valence-band XPS which provides the energy difference between the Fermi energy of underlying metal and the highest energy of the valence bands of the oxide and hydroxide layers in the passive films.

In Chapter 4, a numerical simulation model on photocurrent transients for n-type passive films and anodic films on Ti was developed. The partial differential equations were built by considering the change in the concentration of carriers with the time and the position in the films, based on the generation and annihilation of charge carriers as well as their transports by the drift and diffusion. Simulations were performed by screening several parameters after the discretization of the equations. By fitting the simulated photocurrent transient to the experimentally obtained transient, the electron mobility, the donor density, the recombination coefficient and the interfacial reaction coefficient were estimated. Among the properties, the recombination rate and the donor density clearly exhibited the potential dependence, similar to the experimentally obtained photocurrent transients, and were found to contribute more to the photocurrent transient. Meanwhile, the electron mobility and the interfacial reaction retained almost constant even as the potential changed; these values are considered as intrinsic properties of the film.

Above-mentioned findings are expected to be useful guidelines for improving the corrosion resistance of the passive film.

List of publications

Publications related to this thesis

1. Seong-Cheol Kim, Takao Hanawa, Tomoyo Manaka, Hiroaki Tsuchiya, and Shinji Fujimoto.
   Band structures of passive films on titanium in simulated bioliquids determined by photoelectrochemical response: Principle governing the biocompatibility, *Sci. Technol. Adv. Mater., 23:1, 322–331 (2022)*

2. Seong-Cheol Kim, Hiroaki Tsuchiya, Tomoyo Manaka, Takao Hanawa, and Shinji Fujimoto.
   Electronic structures of passive film formed on Ti and Cr in a phosphate buffer solution of pH 7, *J. Electrochem. Soc., (Accepted March 11, 2024)*

3. Seong-Cheol Kim, Hiroaki Tsuchiya, and Shinji Fujimoto.
   Numerical simulation of photocurrent transients generated from passive films and anodic films on Ti, *Electrochem. Commun., 160, 107666 (2024)*

Other Publications

1. Seong-Cheol Kim, Sang-Hyup Park, Nam-Seok Kim, and Tae-Hyun Nam.
   Microstructures and Martensitic Transformation Behavior of a (Ti+Hf)-Rich Ti-49Ni-12Hf Alloy, *Sci. Adv. Mater., 10, 1236–1240 (2018)*

Acknowledgments

First of all, I would like to express my sincere gratitude to my research guide, ***Prof. Shinji Fujimoto*** of The Division of Material and Manufacturing Science, Osaka University, for his valuable comments, remarks and suggestions throughout the duration of this study. I consider myself privileged to have been able to conduct research under the guidance of a world-class metal electrochemistry expert. Through discussions with him, I was able to expand my insight into the field of metal corrosion. Additionally, he has played an important role not only in my research but also in my professional and personal development.

I am greatly indebted to the readers of this dissertation, ***Prof. Hiromi Yamashita*** and ***Prof. Hiroyuki Yasuda*** of The Division of Material and Manufacturing Science, Osaka University, for their careful and thorough review of the entire manuscript.

I am also deeply grateful to ***Associate Prof. Hiroaki Tsuchiya*** of The Division of Material and Manufacturing Science, Osaka University, for providing insightful discussions and suggestions. His discussions and encouragement were greatly helpful during my doctoral course.

I would like to express the appreciation to ***Assistant Prof. Sayaka Miyabe*** and ***Mr. Junji Nakata*** for their generous support that allowed me to focus on my research. I would also like to thank all members of Fujimoto's Group for their helpful suggestions and collaborations during my study in Japan.

I would like to express the appreciation to ***Prof. Takao Hanawa*** and ***Assistant Prof. Peng Chen*** of Tokyo Medical and Dental University, for their technical assistance, kind help, and constructive comments. I would also like to thank ***Dr. Tomoyo Manaka*** of Tokyo Medical and Dental University, for pertinent advice on the research.

I would like to take this opportunity to express my sincere gratitude to ***Prof. Tae-Hyeon Nam*** of Gyeongsang National University, Republic of Korea, for his sincere encouragement and advice.

I would like to thank ***Jae-Jun Park*** for his generous financial support during my study in Japan. I would also like to thank the Korean international students at Osaka University for their encouragement and kind support.

Finally, I would like to express my deepest gratitude to my family, especially my father ***Sung-Ho Kim***, my mother ***Joo-Young Lee***, and my brother ***Eun-Oh Kim***, for their patience, advice and encouragement. And beloved ***Dr. Ju-Yeon Kim***, who has been very patient and always believed in me, whatever I might say here cannot do full justice to the extent and value of her contribution.

I was able to successfully complete this dissertation with the dedication and help of many people. Although I could not list all of their names, I have dedicated this dissertation to them.

Seong-Cheol Kim

December 2023